



BRNO UNIVERSITY OF TECHNOLOGY
VYSOKÉ UČENÍ TECHNICKÉ V BRNĚ

FACULTY OF CIVIL ENGINEERING
FAKULTA STAVEBNÍ

INSTITUTE OF STRUCTURAL MECHANICS
ÚSTAV STAVEBNÍ MECHANIKY

**STATIC AND DYNAMIC ANALYSIS OF PLAIN
AND FIBER-REINFORCED CONCRETE USING
DISCRETE MESO-SCALE MODEL**

STATICKÁ A DYNAMICKÁ ANALÝZA PROSTÉHO A VLÁKNY VYZTUŽENÉHO
BETONU S VYUŽITÍM DISKRÉTNÍHO MODELU

DOCTORAL THESIS
DISERTAČNÍ PRÁCE

AUTHOR
AUTOR PRÁCE

Ing. Josef Květoň

SUPERVISOR
VEDOUCÍ PRÁCE

doc. Ing. Jan Eliáš, Ph.D.

BRNO 2019

Abstract

The presented thesis is devoted to mathematical modeling of concrete fracture. A special type of model called discrete particle model is used. The concrete meso-structure is simplified as a system of interconnected polyhedral particles. The particles represent larger concrete aggregates with surrounding cement paste. The particle interaction is prescribed at their contacts. Solution of discrete displacement field is obtained under the assumption of small deformations and rigid body movement of particles. Two modifications of the static version of the discrete meso-scale model are presented: (i) representation of short fiber reinforcement and (ii) implicit dynamic solver.

The first main part of the thesis is devoted to modelling of short fiber reinforcement, which is used to improve poor tensile performance of concrete. This material modification leads to more efficient material use and crack width reduction. Short fibers are represented in the discrete model indirectly, taking into account the frictional forces between fiber and cement matrix. The fiber forces are applied at particle contacts working against the crack opening. This modification is able to capture the strain hardening behavior and the multiple cracking of the fiber reinforced composites.

The second main part of the thesis addresses dynamic material behavior. Concrete resistance varies under different strain-rates. For slow, quasi-static loading rates, the initial micro-cracks localize into a macro-crack. For fast loading rates, the energy is not consumed by one crack only, but multiple cracking and crack branching occurs. The inertia typically dominates in fast processes. Even though the meso-scale model accounts for the inertia and the crack branching, the cracking at lower scale is not addressed. Therefore additional phenomenological rate-dependency of the constitutive law is adopted. Numerical simulations on various geometries under various loading rates are performed and compared to experimental evidence from literature. Dynamic material behavior is computed using Newmark's implicit time-integration scheme.

Key words

Concrete Fracture; Discrete modelling; Meso-scale; Fiber Reinforcement; Dynamics; Inertia; Strain-rate

Abstrakt

Předkládaná práce se zabývá matematickým modelováním chování betonu. K numerické analýze je použit diskrétní částicový model. Tento model zjednodušuje meso-strukturu materiálu na systém propojených diskrétních částic – konvexních mnohostěnů. Částice reprezentují větší zrna kameniva společně s okolní cementovou maticí. Tyto částice jsou uvažovány ideálně tuhé a jejich vzájemná interakce je předepsána na kontaktech sousedních částic. Při hledání nespojitého pole posunů a rotací jsou zjednodušeně předpokládány malé deformace. Práce popisuje dvě rozšíření implementovaná do stávající verze modelu, konkrétně (i) přidání reprezentace krátké rozptýlené výztuže a (ii) implicitní dynamický řešič.

První z hlavních částí práce se zabývá modelováním kompozitů s krátkou rozptýlenou výztuží. Krátká vlákna rozptýlená v materiálu přispívají k zlepšení jinak nepříznivé tahové pevnosti betonu. Vlákna přemostňují vznikající trhliny a přenášejí značnou část zatížení, dochází tak ke snížení šířky trhlin, jejich četnost je naopak zvýšena a materiál je pak lépe využit. Vlákna jsou v částicovém modelu reprezentována nepřímo, zohledněním tření mezi vláknem a cementovou maticí silami, které působí proti otevírání trhlin. S pomocí tohoto rozšíření model dokáže předpovídat chování vláknobetonu zahrnující tahové zpevnění i navýšení počtu trhlin.

Druhá z hlavních částí se zabývá odezvou materiálu na dynamické zatížení. Beton vykazuje rozdílné chování pro různé rychlosti zatěžování. V případě pomalého, kvazi-statického, zatěžování se počáteční mikro-trhliny lokalizují v makro-trhlinu. Dochází-li k rychlému zatěžování, energie nahromaděná v tělese není spotřebována pouze jednou trhlinou, ale dochází k jejímu větvení. V případě rychlých procesů je hlavním faktorem setrvačnost hmoty, která je zatížením urychlována. Struktura materiálu a setrvačnost částic je v mezo-úrovňovém diskrétním modelu zahrnuta. Přesto ale další jevy probíhající pod rozlišovací úrovní modelu ovlivňují výsledné chování materiálu. Proto je do modelu přidána fenomenologická závislost konstitutivního zákona na rychlosti přetváření. Numerické simulace těles rozličných tvarů zatěžovaných různou rychlostí deformace jsou porovnány s experimenty z literatury.

Klíčová slova

Beton; Trhliny; Diskrétní model; Mezo úrovňový model; Krátká rozptýlená výztuž; Dynamika; Setrvačnost; Rychlost zatěžování

Bibliografic citation

KVĚTONĚ, Josef. *Static and Dynamic Analysis of Plain and Fiber-Reinforced Concrete Using Discrete Meso-Scale Model*. Brno, 2019. 93 p. Doctoral Thesis. Brno University of Technology, Faculty of Civil Engineering, Institute of Structural Mechanics. Supervised by Jan Eliáš

Institute of Structural Mechanics
Faculty of Civil Engineering
Brno University of Technology
Czech Republic

Typeset by L^AT_EX 2_ε

Declaration of originality

This doctoral thesis is made in order to fulfill the requirements to obtain the degree of Doctor of Philosophy at Brno University of Technology, study program 3607V009 Structures and Traffic Constructions. I declare that this doctoral thesis titled *Static and Dynamic Analysis of Plain and Fiber-Reinforced Concrete Using Discrete Meso-Scale Model* represents my own work and the results of my original research. I have clearly indicated the presence of quoted or paraphrased material and provided references for all sources.

Brno

.....

Josef Květoň

Acknowledgement

First of all, I would like to acknowledge the supervision of my work by doc. Jan Eliáš. He was always very supportive and also friendly to me. I am glad that I could have been his doctoral student and I am looking forward to our future teamwork.

Next, I would like to thank my family for their support during this and also previous studies. They gave me all the support and perfect background so I could become the person who I am today.

I would also like to thank the other colleagues from the Institute of Structural Mechanics. I thank prof. Mirek Vořechovský for including me into his team to work on joint projects. I also thank colleagues from our office and other doctoral students from our faculty, Petr Král, Martin Kalina, Michal Vyhlídal, Jan Mašek, Petr Miarka, Lukáš Novák and Vašek Sadílek. I always enjoyed our discussions, common lunches and many other events we organizes together.

I would also like to thank the team of Micro-lab from TU Delft, where I spent 6 months during my Erasmus Internship. All of them were very nice to me and took me as a part of their team. Special thanks go to prof. Erik Schlangen and Stefan Chaves Figueiredo for introducing me to the topic of fiber reinforced composites.

Finally, I would like to thank my friends from 16th Scout Unit Brno – Duha, from futsal club Brno – Jehnice, from high-school or our church and all of my friends. If I wanted to state all of them here, number of pages of this thesis would be doubled at least, so just a few of them: Kuba Šmerda, Vojtěch Kolář, Dominik Schmidt and Vít Pospíchal. I am glad for all these people I could have meet during my life up to this point.

Thank you

Apart from support from the mentioned individuals, the work on this thesis was financially support by:

Czech Science Foundation under projects GA16-22230S, GJ15-19865Y, GA19-12197S, GA19-06684J and Ministry of Education, Sports and Youth of under Specific University Research projects FAST-J-17-4583 and FAST-J-18-5412.

This support is gratefully acknowledged.

CONTENTS

1	Introductory remarks	1
1.1	Fracture of concrete	2
1.2	Modelling approaches	3
1.3	Objectives	5
I	Discrete modeling approach	7
2	Discrete formulation	9
3	Meso-scale discrete model	11
3.1	Spatial domain discretization	11
3.2	Contact behavior	11
3.3	Integration of stress over the facet	18
3.4	Random field	20
II	Fiber reinforced concrete	21
4	Fibers and concrete	23
4.1	Cementitious composites with fibers	23
4.2	Fiber representation in computational model	24
5	Fibers in meso-scale model	27
5.1	Fiber bridging force	27
5.2	Multiple cracking	28
5.3	Micro-effects at fiber exit point	29
5.4	Fibers in discrete model	31
6	Numerical simulations	33
6.1	Two sided pullout	33
6.2	Volume fraction effect	34
6.3	Preliminary study on uniaxial tensile test	35
6.4	Detail study on model parameters influence	36
6.5	Random concrete strength	40
6.6	Comparison to experimental data	40
6.7	Conclusions about the fiber model	42

III	Dynamics	45
7	Strain-rate effect in concrete fracture	47
8	Transient solution	49
8.1	Balance equation - time integration	49
8.2	Mass matrix	50
8.3	Elastic behavior in dynamic regime	51
8.4	Strain rate dependency of constitutive law	54
9	Numerical simulations	59
9.1	Available experimental data	59
9.2	L-shaped specimen	60
9.3	Compact tension specimens	67
9.4	Brazilian disk specimen	70
9.5	Spalling test	73
9.6	Conclusions about the dynamic model	82
10	Closing remarks	85
10.1	Future work	86
	Bibliography	87
	Curriculum vitae	95
	List of publications	96

LIST OF FIGURES

2.1	Various types of discrete formulation in 2D. Left: lattice of trusses or beams, center: projection of concrete structure and different element properties and right: rigid polygonal particles	9
3.1	(a) 3D Voronoi rigid cell with connections to neighbouring particle centers, (b) decomposition of polyhedron into tetrahedrons, (c) <i>simple</i> and (d) <i>discretized</i> facet.	13
3.2	Schematic description of tensile part of the meso-scale constitutive law with strain-softening.	15
3.3	Top: elastic limit in terms of straining direction angle $\omega \in \langle -\frac{\pi}{2}; \frac{\pi}{2} \rangle$; bottom: different post-critical behavior for different angle ω	17
3.4	Difference in model results obtained with beam loaded in uni-axial tension.	19
3.5	Difference in model results obtained for four point bending test.	19
4.1	(a) fiber bridging crack in material, (b) representation of different material phase in lattice model, (c) indirect fiber representation in discrete particle model and (d) frictional and bond stress distribution along the fiber length.	24
5.1	Crack length divided into pullout on each side according to different stage of fiber behavior – debonding on the left, pullout on the right. Superscripts R and L refer to the right and left side of the crack respectively.	27
5.2	Schematic explanation of angles used in Eqs.(5.8-5.10).	29
5.3	Influence of parameters describing micro-scale fiber behavior – Eqs. (5.8-5.10)	30
6.1	Influence of material parameters to results of two-sided pullout simulation.	33
6.2	Influence of fiber volume fraction on a single contact response.	34
6.3	Settings of uni-axial tensile test with fibers aligned with loading direction or randomly oriented.	35
6.4	Influence of material parameters to results of uni-axial test simulation of prism made of fiber reinforced composite.	36
6.5	Sensitivity of loading and straining capacity to model input parameters.	37
6.6	Influence of concrete parameters.	38
6.7	Influence of shear stress between fiber and matrix τ_0 and hardening parameter β_f	39
6.8	Influence of parameters related to micro-spalling at the fiber exit point.	40

6.9	Application of random field on concrete material parameters; top: load-displacement curves, center: spatial fluctuation of concrete strength, bottom: crack pattern at the final stage.	41
6.10	Comparison of the numerical load-displacement curves and crack patterns with the experimental data reported by Li et al. (2001).	42
8.1	Modeled geometry and deformed shape showing the discrete structure with 100 times magnified deformation.	52
8.2	Dynamic response of cantilever beam using various time discretizations.	53
8.3	Dynamic response of cantilever beam using various parameters of Newmark method.	54
8.4	Dynamic response of a cantilever beam using different particle sizes.	54
8.5	Influence of parameters on increase function and scaling the elastic envelope for increasing strain rate.	55
8.6	Increase in tensile strength for various settings of the model compared with experimental data (Yan and Lin, 2006; Wu et al., 2005; Brara and Klepaczko, 2006a) and modified CEB formulation (Malvar and Crawford, 1998).	57
9.1	Geometry of simulated L-shaped specimen showing particle model structure.	60
9.2	Effect of selected material properties on the maximum loading force at various displacement rates.	61
9.3	Load-displacement curves and crack patterns for different material strength used in numerical simulations compared with experimental data reported by Ozbolt et al. (2015).	62
9.4	Comparison of nonlinear vs. elastic response of the model.	63
9.5	Relation between maximum loading force and displacement rate.	64
9.6	Effect of gradual increase of displacement rate and different particle size.	65
9.7	Response of the model using strain rate dependent constitutive law and steel platen at the loading point.	66
9.8	Different response for different random field realizations applied.	67
9.9	Geometry of the specimen (left) and reaction-displacement curves for various loading rates (right).	68
9.10	Crack patterns obtained from numerical simulations compared with experimental data from Ozbolt et al. (2013) for lower loading rates.	68
9.11	Crack patterns obtained from numerical simulations compared with experimental data from Ozbolt et al. (2013) for higher loading rates.	69

9.12	Relation between displacement rate and the maximum reaction (left) or the maximum loading force (right).	69
9.13	Setup of the model representing Brazilian discs.	70
9.14	Left: force vs. displacement curve for thin mortar specimens, right: damaged volume obtained by simulation (with magnified displacements).	72
9.15	Dynamic increase factor of material tensile strength obtained by the model compared with experimental measurements (Jin et al., 2017).	73
9.16	Visualization of model geometry used in numerical simulation of spalling test – concrete cylinder discretized into particles loaded by a stress wave.	74
9.17	Results for different time step length Δt , left: rear face velocity evolution in time, right: stress profile along the elastic bar in particular times.	75
9.18	Two stress waves reported by Erzar and Forquin (2011), wave 3 with half intensity of wave 1 is introduced for study of model behavior.	76
9.19	Preliminary study on various material model settings.	77
9.20	Two different ways to estimate the residual velocity to calculate the pull-back velocity ΔV_{pb} .	78
9.21	Stress profile along the specimen and crack pattern in time of maximum tensile σ_x for simulation with $0.25 \times f_t$.	79
9.22	Stress profile along the specimen and crack pattern in time of maximum tensile σ_x for simulation with $0.5 \times G_f$.	80
9.23	Stress profile along the specimen and crack pattern in time of maximum tensile σ_x for reference simulation.	80
9.24	Results of numerical simulations compared to the experimental data by Erzar and Forquin (2011).	81
9.25	Different fraction of damaged volume relative to different specimen size.	83
9.26	Different amount of damaged volume for different strain rate for specimen of width = $400 \mu\text{m}$.	83

LIST OF TABLES

8.1	Parameters of strain rate dependency for various settings of constitutive law used in calculations.	56
9.1	Material parameters used from simulations of concrete and mortar discs.	71
9.2	Peak load and tesile strength obtained by the model assuming quasi-static loading compared to the experiments by Jin et al. (2017)	71
9.3	Different $f_{t,dyn}$ according to different points considered for values of residual velocity v_r	78

1 INTRODUCTORY REMARKS

In construction industry, there is a great demand on reduction of material consumption nowadays. Possibilities leading to more efficient material usage are being investigated. It is not only trend of past few years but more likely decades. There are various reasons for such demand. One of them is economical sustainability of newly built structures, that has always been important factor. Besides, nowadays, developed countries start to reflect the fact that also environmental point of view should be taken into consideration. It is not only the limited amount of limestone or other material resources, but also the emission of CO_2 during cement production. When calcium carbonate is thermally decomposed lime and carbon dioxide is produced. According to Worrell et al. (2001), the cement industry contributes about 5% to the global anthropogenic CO_2 emissions.

On the other hand, some kinds of industrial waste can be further used in construction industry. Materials producing clinker minerals can be used instead of Portland cement or as its partial replacement in concrete mix. These are, for example, blast furnace slag, which is a waste from the processing of iron ore, fly ash that comes from burning of coal or a side product of manufacturing silicon - silica fume (Aİtçin, 2016).

Various admixtures have been introduced to improve concrete performance, for example old tires (Bignozzi and Sandrolini, 2006). Also short fiber reinforcement can lead to better tensile performance of concrete and reduction of crack width (Bentur and Mindess, 2007). Part II of this thesis is devoted to numerical modeling of fiber reinforced concrete.

The reduction of material consumption can also be achieved by more detailed understanding of material behavior, which is the essential part of structural design. In modern industry, material engineering plays a crucial role. This branch, in a way we know it nowadays, is being developed since the mid-20th century. The knowledge of a material composition is very important and, based on this insight, the behavior of a material during its life-cycle can be described in detail.

Cracks and discontinuities significantly influence overall behavior and durability of structural elements, therefore it is important to understand the processes of their formation and growth. Disciplines dealing with fracture of materials were at first focused on homogeneous materials like glass or steel, where the failure can be described by linear elastic fracture mechanics. With growth of industrial production, more detailed and reliable description of material behavior is required also for heterogeneous materials. Typical heterogeneous material is concrete, where, besides relatively homogeneous cement paste, mineral aggregates appear. Their size, shape and placement within the volume affects the resulting composite quality.

A great progress that has been done in this field in the past decades is closely related to development in the numerical mathematical methods and a growth of computing possibilities. In the early days of material engineering, analytical models were commonly used (Shah and Carpinteri, 1991). Where analytical descriptions are not possible, numerical solutions can provide approximations of high accuracy. With the growth of computing, ability to use more computationally demanding techniques arises.

1.1 Fracture of concrete

Materials are often distinguished according to their behavior under loading. There is a group of materials with ductile behavior. For this group, plastic yielding is typical. If such material is loaded, plastic deformation occurs after reaching the elastic limit and loading force typically further increases (for materials with strain-hardening). On the other side of the range, there are brittle materials. They collapse immediately after reaching the material strength, which is typically close to the elastic limit. But there is also a group of materials that exhibit so called quasi-brittle behavior. Their response after reaching the elastic limit is neither brittle nor ductile and changes with size of the specimen. Their collapse is not instantaneous, but, after reaching maximum strength, ability to transfer load slowly decreases with increasing deformation. This group of materials comprises e.g. rocks, ice and also material widely used in civil engineering – concrete.

When we distinguish between either homogeneous and heterogeneous or ductile and brittle (eventually quasi-brittle) materials, we need to take into account the scale. The classification of materials in previous paragraph is done with consideration of dimensions commonly used in construction industry. Looking at the micro-structure of steel, we would observe dislocations and heterogeneities. Relation between inner structure of the material and dimensions of an investigated element is of importance. The material behavior could be considered as scale dependent rather than a constant property.

Cusatis et al. (2014) distinguish among seven length scales for concrete, namely (I) full structure scale, (II) structural element scale, (III) plain concrete scale, (IV) concrete meso-scale (distinguishing aggregates), (V) mortar scale, (VI) cement paste scale and finally (VII) C-S-H gel scale. When developing a concrete model, it is necessary to determine at which scale it will be used. This thesis is focused at the meso-scale modelling.

Looking closer at the concrete meso-scale structure, one can distinguish different phases that are closely related to the process of material fracturing. The following

concrete phases are usually characterized: aggregates, cement paste and inter-facial-transition zone (ITZ), which is a thin layer on the contact of aggregate with cement paste. Sometimes, voids are considered as a separate phase too.

The fracture of concrete usually initiates from ITZ (or voids), which is the weakest part of material. Under increasing loading, a lot of micro-cracks grow in material. Finally some of them connect and form the macro-crack, i.e. crack localizes. The crack then propagates through the material and usually does not cross the aggregates, whose strength is considered much higher than the strength of the cement paste. There is a significant difference between high performance and normal strength concrete (usually taken as concrete up to class C50/60). In the case of high strength concrete, crack often propagates across the aggregates.

1.2 Modelling approaches

There is a large effort to develop robust and reliable numerical models of materials behavior. No universal model for every material at every scale exists. Every numerical model is a simplification of reality and is convenient for a particular purpose. Some of them have a wide range of purposes, some are focused to a small area of interest. Deeper understanding of material behavior can be obtained from fine, low-scale model and behavior derived at the fine scale can be further used in continuous models at scale of structural members and whole constructions. Also for concrete, various models are used at different length scales. Model used for simulation of overall behavior of whole structure is different than the one used for modeling the interaction of atoms in C-S-H gel (Calcium-Silicate-Hydrate).

Homogeneous models are suitable for material scales where material can be simplified as homogeneous. In case of steel, this can be also applied for relatively small structural members, e.g. bolts. In case of concrete, homogeneity assumption is widely used in case of modelling of whole buildings. The homogeneous models are typically treated as continuous, i.e. unknown displacement field must be continuous.

Problems treated as continuous are described by partial differential equations. An approximate solution of such problems can be provided by various numerical methods. Nowadays, *finite element method* (FEM) is widely used in many different branches of engineering.

Besides geometric and balance equations, mechanical model needs also constitutive equation relating strain and stress. The tensile failure of quasi-brittle materials is often simulated using constitutive relation with strain-softening. The descending part of the constitutive law can be expressed by various kinds of plastic or damage models. Anytime a negative slope appears in the stress – strain relation, localization

of inelastic deformation may occur. This localization phenomenon causes so called spurious mesh sensitivity – the results of the simulations are dependent on the discretization of the material body. Various regularization techniques were established to prevent this behavior.

Crack band model (Bažant and Oh, 1983) uses *fracture energy density* dependent on the element size to ensure that the amount of work dissipated during the fracture process is mesh-independent. *Nonlocal* approach (Bažant and Lin, 1988; Jirásek, 1998) calculates the damage according to a nonlocal variable – e.g. strain (depends on the type of nonlocal formulation). In both of the mentioned approaches, crack is smeared, the material remains continuous, but its integrity is being degraded. Some other approaches allow the discontinuity in a continuous body, e.g. *embedded crack model* (Oliver, 1996) or *extended finite elements* – XFEM (Belytschko and Gracie, 2007).

Concrete fracture takes place at the scale, where one can distinguish individual aggregates. Material is far from homogeneous at this scale. It is therefore convenient to use a model that account for material heterogeneity. Alternatively to the continuous approach, material can be represented by a system of interconnected discrete particles. Various versions of discrete formulation has been proposed in literature. Discrete meso-scale model can be conveniently used for fracture of concrete in particular. Detailed description of the discrete approach and meso-scale model is presented in Part I.

In reality, any process happens in a certain time period. If the loading is applied slowly enough, the static equilibrium can be considered. In particular cases, neglecting viscous effects or structural inertia is, however, not possible. For fast events like impact or blast, dynamic equilibrium that take into account inertia effects is more appropriate. Both static and dynamic solutions are presented in this thesis. Part III is devoted to detailed description of dynamic concrete behavior simulated by discrete meso-scale model.

1.3 Objectives

The aim of the thesis is to present discrete meso-scale model for concrete, describe its advantages and weak spots as well. Since it is directed towards meso-scale, it is inapplicable for structural design due to large computational demands. It is suitable for design of smaller structural parts, but primarily for detailed description of fracture processes.

The thesis is structured into three parts. The first part introduces discrete approach and presents the discrete particle model used in further parts for numerical simulations. The next two parts present two modifications, representation of short fiber reinforcement and extension of the code by an implicit dynamic solver.

The objectives of the thesis are:

- Extend the existing model with representation of short fiber reinforcement.
- Incorporate dynamic solver into existing static version of the model.
- Show the model performance and sensitivity to the input parameters.
- Validate the model on comparison with data presented in literature.

Part I

Discrete modeling approach

2 DISCRETE FORMULATION

Many versions of discrete approach has been introduced in literature (van Mier, 2013; Cusatis et al., 2003; Grassl et al., 2012). One of the first attempts was a lattice of elasto-brittle elements that provides quasi-brittle behavior at macro-scale. Various enhancements were proposed to this model, e.g. random placement of the lattice nodes (Fig. 2.1 left) or random material properties for each element. Spatial fluctuation of material properties can be represented by random assignment of material properties to the particular truss or beam. Such an assignment can be independent or material properties can be spatially correlated (Vořechovský, 2008).

Another option is to project material inner structure on a fine lattice model and assign the material properties accordingly (Fig. 2.1 center). Then one can distinguish particular material phase (aggregate, cement paste or interfacial transitional zone - ITZ) that each lattice element represents. In this type of models, elasto-brittle constitutive law is usually used and different material parameters are assigned according to the material phase. Even with such simple settings, the model is capable of representing complex material behavior (van Mier, 2013).

Unfortunately, such a fine lattice model leads to a computational system with a large number of degrees of freedom (DOF), especially in 3D, which makes it inefficiently demanding. These fine models are therefore usually used for representation of small material volume only.

The work in the thesis is based on the meso-scale particle model where the volume domain is discretized into a system of rigid bodies with a convex polyhedral shape (Fig. 2.1 right) (Cusatis and Cedolin, 2007). The interaction between particles takes place on the facets, where normal, shear and rotational resistance of the contact is prescribed.

Comparing fine lattice and meso-scale particle model, indisputable advantage of

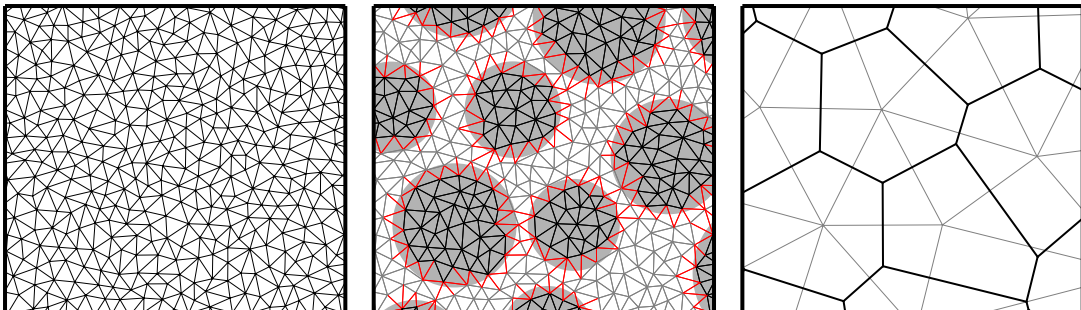


Fig. 2.1: Various types of discrete formulation in 2D. Left: lattice of trusses or beams, center: projection of concrete structure and different element properties and right: rigid polygonal particles

the later is large reduction of number of DOFs. On the other hand, more complex constitutive law needs to be used, since the lower scale phenomena are omitted.

3 MESO-SCALE DISCRETE MODEL

The mechanical problem is formulated directly in discrete form. The material is represented by a system of interconnected particles with three translational and three rotational degrees of freedom. Rigid particles represent larger mineral aggregates with surrounding cement matrix, smaller grains are omitted. The kinematics of the model is provided by rigid-body motion of the particles that results in displacement jumps between them. The origin of this approach is attributed to work of Kawai (1978). Similar models are often referred to as rigid-body-spring networks. The mathematical model used within this thesis is adopted according to Cusatis and Cedolin (2007).

3.1 Spatial domain discretization

Material inner structure represented by a system of interconnected particles is based on Voronoi tessellation. At first, particle centers are generated within the volume domain. Nodes positions are generated randomly in a sequential process, rejecting those with minimal distance to the others below chosen model parameter l_{\min} . This internal length dictates the particle size and to large extent also the nonlinear behavior of the model.

Then Voronoi tessellation is performed to get the geometry of the particles. The Voronoi tessellation is a dual projection of Delaunay triangulation. Circumscribing circle (sphere) of any simplex of this triangulation does not contain any other node. Connections of centers of the circumscribing circles then form the ridges of Voronoi tessellation. In other words, Voronoi cell belonging to one node is a set of all points that are closer to the particular node than to any other. In case of 3D model, Voronoi cells are convex polyhedrons. To obtain Voronoi tessellation, *qhull* library is used (Barber et al., 1996).

Since the discretization of a material body comes from pseudo-random process, the response of simulations with different meso-scale geometry differs as well. This can be compared with reality, where material internal structure is also random and so is the response of each specimen.

3.2 Contact behavior

3.2.1 Kinematics

Displacement \mathbf{u}_p of arbitrary point \mathbf{p} within a rigid body can be expressed in terms of displacements \mathbf{u}_a of particle center \mathbf{a} and rotations $\boldsymbol{\theta}_a$ of the rigid body a

as

$$\mathbf{u}_p = \mathbf{u}_a + \boldsymbol{\theta}_a \times (\mathbf{p} - \mathbf{a}) \quad (3.1)$$

in matrix-vector form

$$\begin{Bmatrix} u_1^p \\ u_2^p \\ u_3^p \end{Bmatrix} = \underbrace{\begin{bmatrix} 1 & 0 & 0 & 0 & x_3^p - x_3^a & x_2^a - x_2^p \\ 0 & 1 & 0 & x_3^a - x_3^p & 0 & x_1^p - x_1^a \\ 0 & 0 & 1 & x_2^p - x_2^a & x_1^a - x_1^p & 0 \end{bmatrix}}_{\mathbf{A}_a^p} \begin{Bmatrix} u_1^a \\ u_2^a \\ u_3^a \\ \theta_1^a \\ \theta_2^a \\ \theta_3^a \end{Bmatrix} \quad (3.2)$$

where subscripts 1, 2 and 3 refer to 3 directions of coordinate basis. In this description of rigid body motion, small deformations and rotations are assumed. Consider two rigid bodies a and b with one common contact facet as in Fig. 3.1(c). Assuming arbitrary displacements and rotations for a and b , displacement of point c at contact facet can be expressed substituting c and a (respectively b) into Eq. 3.1. Difference between displacement from both sides of the contact results in the following expression for displacement jump $\Delta \mathbf{u}_{ab}$ between rigid bodies a and b at point c

$$\Delta \mathbf{u}_{ab} = \mathbf{A}_b^c (\mathbf{u}_b \boldsymbol{\theta}_b)^T - \mathbf{A}_a^c (\mathbf{u}_a \boldsymbol{\theta}_a)^T \quad (3.3)$$

Since the constitutive law is formulated in normal and shear direction, strain in the local contact coordinate system is needed.

$$\mathbf{e}_{ab} = \begin{Bmatrix} e_N \\ e_M \\ e_L \end{Bmatrix} = \underbrace{\begin{bmatrix} n_1 & n_2 & n_3 \\ m_1 & m_2 & m_3 \\ l_1 & l_2 & l_3 \end{bmatrix}}_{\mathbf{R}} \frac{\Delta \mathbf{u}_{ab}}{L} \quad (3.4)$$

Substituting Eqs. (3.2) into (3.4) we obtain relation between nodal displacements and rotations and contact strain

$$\mathbf{e}_{ab} = \mathbf{R} \frac{1}{L} \underbrace{\begin{bmatrix} -\mathbf{A}_a^c & \mathbf{A}_b^c \end{bmatrix}}_{\mathbf{B}} \begin{Bmatrix} \mathbf{u}_a \\ \boldsymbol{\theta}_a \\ \mathbf{u}_b \\ \boldsymbol{\theta}_b \end{Bmatrix} \quad (3.5)$$

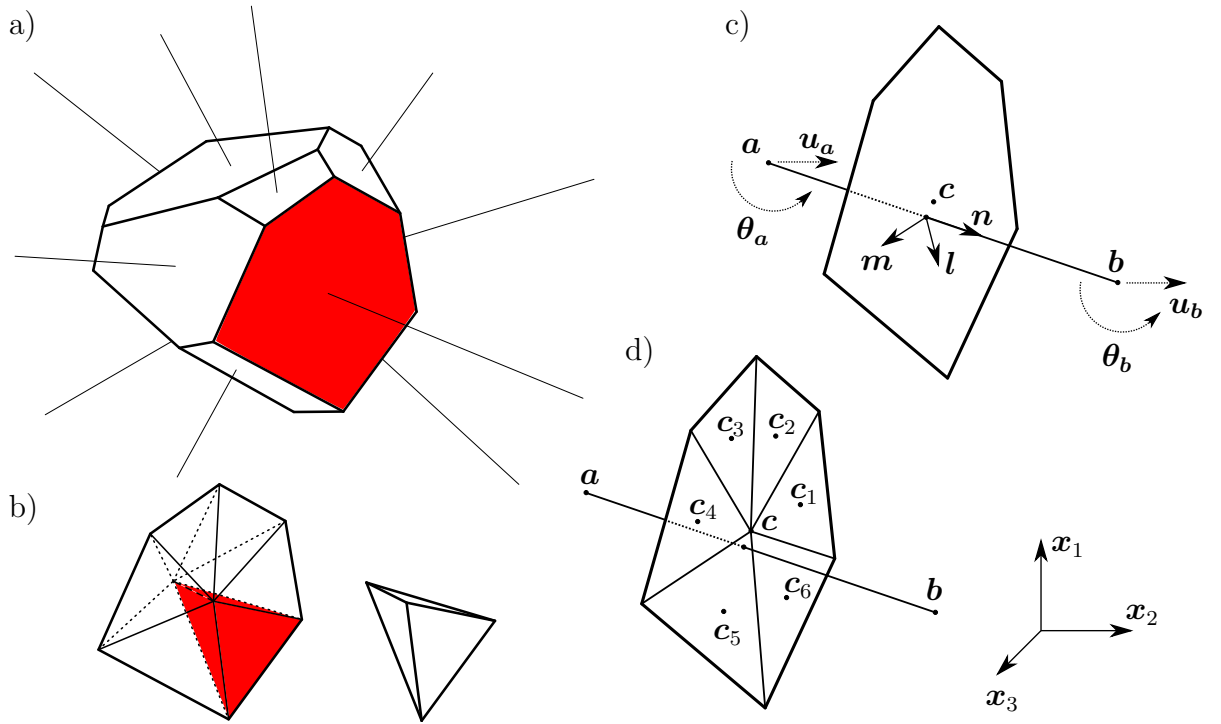


Fig. 3.1: (a) 3D Voronoi rigid cell with connections to neighbouring particle centers, (b) decomposition of polyhedron into tetrahedrons, (c) *simple* and (d) *discretized* facet.

The displacement jump $\Delta \mathbf{u}$ divided by the contact length L (distance between particle centers) and projected into the local coordinate system, represents contact (meso-scale) strain vector \mathbf{e} . Here \mathbf{R} is transformation matrix, \mathbf{n} is the direction normal to the facet and \mathbf{m} and \mathbf{l} are two arbitrarily chosen directions forming with \mathbf{n} an orthonormal basis, see Fig. 3.1(c). Subscripts N , M and L refer to components in local contact coordinates.

3.2.2 Elastic constitutive behavior

Interaction of particles is governed by constitutive relations that are applied at their contact facets. The meso-scale elastic behavior is controlled by two parameters, namely elastic modulus E_0 and ratio between tangential and normal stiffness α . On the contacts (facets), normal and shear stiffness of particle connection is prescribed.

The meso-scale stress is denoted \mathbf{s} . The relation between stress \mathbf{s} and strain \mathbf{e} in elastic regime on each facet yields

$$\mathbf{s} = E_0 \alpha \mathbf{e}$$

$$\begin{Bmatrix} s_N \\ s_M \\ s_L \end{Bmatrix} = E_0 \begin{bmatrix} 1 & & \\ & \alpha & \\ & & \alpha \end{bmatrix} \begin{Bmatrix} e_N \\ e_M \\ e_L \end{Bmatrix} \quad (3.6)$$

Multiplying the stress \mathbf{s} by the contact area A , we get the contact force \mathbf{f} .

$$\mathbf{f} = A\mathbf{s} = A E_0 \alpha \mathbf{R} \mathbf{B} \mathbf{u}$$

$$\begin{Bmatrix} f_N \\ f_M \\ f_L \end{Bmatrix} = A \begin{Bmatrix} s_N \\ s_M \\ s_L \end{Bmatrix} = A E_0 \alpha \mathbf{R} \underbrace{\frac{1}{L} \begin{bmatrix} -\mathbf{A}_a^c & \mathbf{A}_b^c \end{bmatrix}}_{\mathbf{B}} \begin{Bmatrix} \mathbf{u}_a \\ \boldsymbol{\theta}_a \\ \mathbf{u}_b \\ \boldsymbol{\theta}_b \end{Bmatrix} \quad (3.7)$$

Since the parameters E_0 and α are applied at meso-scale, one needs some estimation of overall material behavior observed at macro-scale. The theoretical relation between these meso-scale parameters and macro-scale Young's modulus and Poisson's ratio can be derived (Eliáš, 2017). This relation reads

$$E_0 = \frac{1}{1 - 2\nu} E ; \quad \alpha = \frac{1 - 4\nu}{1 + \nu} \quad (3.8)$$

Note that Eq.(3.6) postulates limitation on Poisson's ratio, that must be within interval $(-1, 0.25)$. Nevertheless, value of Poisson's ratio for concrete is around 0.2.

Relation (3.8) is only theoretical based on relatively strong assumption about model rotations and displacements. Behavior of the numerical model is also influenced by the presence of boundaries. The real model response using parameters obtained from Eq.(3.8) would be slightly more compliant compared to analytical solution (Eliáš, 2017).

3.2.3 Balance equation

The solution of unknown displacements comes from principle of virtual work. We know that work of forces (forces \mathbf{f}_a , \mathbf{f}_b and moments \mathbf{m}_a , \mathbf{m}_b) acting on virtual nodal displacements ($\delta\mathbf{u}_a$, $\delta\mathbf{u}_b$ and $\delta\boldsymbol{\theta}_a$, $\delta\boldsymbol{\theta}_b$) must be equal to work of forces (\mathbf{f} from

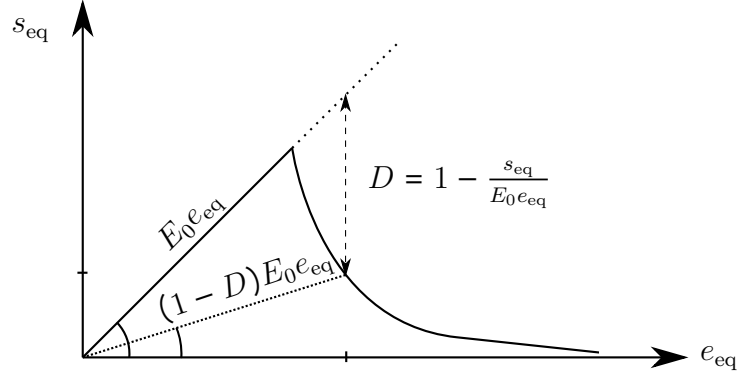


Fig. 3.2: Schematic description of tensile part of the meso-scale constitutive law with strain-softening.

Eq. 3.7) acting on facet virtual jumps ($\delta \Delta \mathbf{u}_{ab} = L \delta \mathbf{e}_{ab}$).

$$\begin{aligned} \begin{pmatrix} \mathbf{f}_a & \mathbf{m}_a & \mathbf{f}_b & \mathbf{m}_b \end{pmatrix} \begin{pmatrix} \delta \mathbf{u}_a & \delta \boldsymbol{\theta}_a & \delta \mathbf{u}_b & \delta \boldsymbol{\theta}_b \end{pmatrix}^T &= \mathbf{f}^T \delta \Delta \mathbf{u}_{ab} \\ \begin{pmatrix} \mathbf{f}_a & \mathbf{m}_a & \mathbf{f}_b & \mathbf{m}_b \end{pmatrix} \begin{pmatrix} \delta \mathbf{u}_a & \delta \boldsymbol{\theta}_a & \delta \mathbf{u}_b & \delta \boldsymbol{\theta}_b \end{pmatrix}^T &= \\ &L \mathbf{f}^T \mathbf{R} \mathbf{B} \begin{pmatrix} \delta \mathbf{u}_a & \delta \boldsymbol{\theta}_a & \delta \mathbf{u}_b & \delta \boldsymbol{\theta}_b \end{pmatrix}^T \end{aligned} \quad (3.9)$$

Substituting (3.7) into (3.9) we obtain system of equations relating nodal displacements and rotations with nodal forces and moments

$$\underbrace{\begin{pmatrix} \mathbf{f}_a & \mathbf{m}_a & \mathbf{f}_b & \mathbf{m}_b \end{pmatrix}^T}_{\mathbf{F}} = \underbrace{E_0 A L \mathbf{B}^T \mathbf{R}^T \boldsymbol{\alpha} \mathbf{R} \mathbf{B}}_{\mathbf{K}} \underbrace{\begin{pmatrix} \mathbf{u}_a & \boldsymbol{\theta}_a & \mathbf{u}_b & \boldsymbol{\theta}_b \end{pmatrix}^T}_{\mathbf{u}} \quad (3.10)$$

Here, \mathbf{K} is the stiffness matrix, \mathbf{u} is the vector of nodal displacements and \mathbf{F} is the loading vector.

3.2.4 Inelastic constitutive behavior

In nonlinear regime, isotropic damage model is applied. After reaching the elastic limit f_{eq} , the integrity of any contact is described by a damage parameter $D \in \langle 0, 1 \rangle$. Zero value stands for intact material, 1 means that the contact is not able to transfer any stress. Then, stress-strain relation described by Eq. (3.11) is modified

$$\mathbf{s} = (1 - D) E_0 \boldsymbol{\alpha} \mathbf{e} \quad (3.11)$$

Evolution of damage D is a crucial part of the constitutive law. For the case of tensile loading, damage calculation is schematically described in Fig. 3.2. It is calculated

in an equivalent space defined by equations (3.12) and (3.13).

$$e_{\text{eq}} = \sqrt{e_N^2 + \alpha(e_M^2 + e_L^2)} \quad (3.12)$$

$$s_{\text{eq}} = \sqrt{s_N^2 + (s_M^2 + s_L^2)/\alpha} \quad (3.13)$$

$$D = 1 - \frac{s_{\text{eq}}}{E_0 e_{\text{eq}}} \quad (3.14)$$

Note that s_{eq} in Eq.(3.14) is unknown value dependent on straining direction $\omega \in \langle -\pi/2, \pi/2 \rangle$. This is calculated from local components of contact strain

$$\omega = \arctan\left(\frac{e_N}{\alpha\sqrt{e_M^2 + e_L^2}}\right) \quad (3.15)$$

Straining direction $\omega = -\pi/2, 0$ and $\pi/2$ indicates compressive, pure shear and tensile loading, respectively. Any angle within these limits is a combination of normal and shear loading.

At first, value of the elastic limit $f_{\text{eq}}(\omega)$ for a particular straining direction ω is calculated, see upper part of Fig. 3.3

$$f_{\text{eq}} = \begin{cases} \frac{16f_t}{\sqrt{\sin^2 \omega + \alpha \cos^2 \omega}} & \omega < \omega_0 \\ f_t \frac{4.52 \sin \omega - \sqrt{20 \sin^2 \omega + 9\alpha \cos^2 \omega}}{0.04 \sin^2 \omega - \alpha \cos^2 \omega} & \omega \geq \omega_0 \end{cases} \quad (3.16)$$

If corresponding strain is exceeded, equivalent stress s_{eq} is calculated from

$$s_{\text{eq}} = \min\left(\begin{array}{c} (1 - D_{\text{max}})E_0 e_{\text{eq}} \\ f_{\text{eq}} \exp\left(\frac{K}{f_{\text{eq}}}\left\langle e_{\text{eq}} - \frac{f_{\text{eq}}}{E_0} \right\rangle\right) \end{array}\right) \quad (3.17)$$

Here, value of maximum previously reached level of damage D_{max} provides its irreversibility and is stored for every contact individually. If the currently reached equivalent strain e_{eq} is larger than the one reached previously, equivalent stress s_{eq} comes from the lower part of Eq.(3.17). Note that only the positive part of values in Macaulay brackets is considered. Evolution of s_{eq} reflects the complexity of the combination of normal and tangential loading. Initial slope K of the soften-

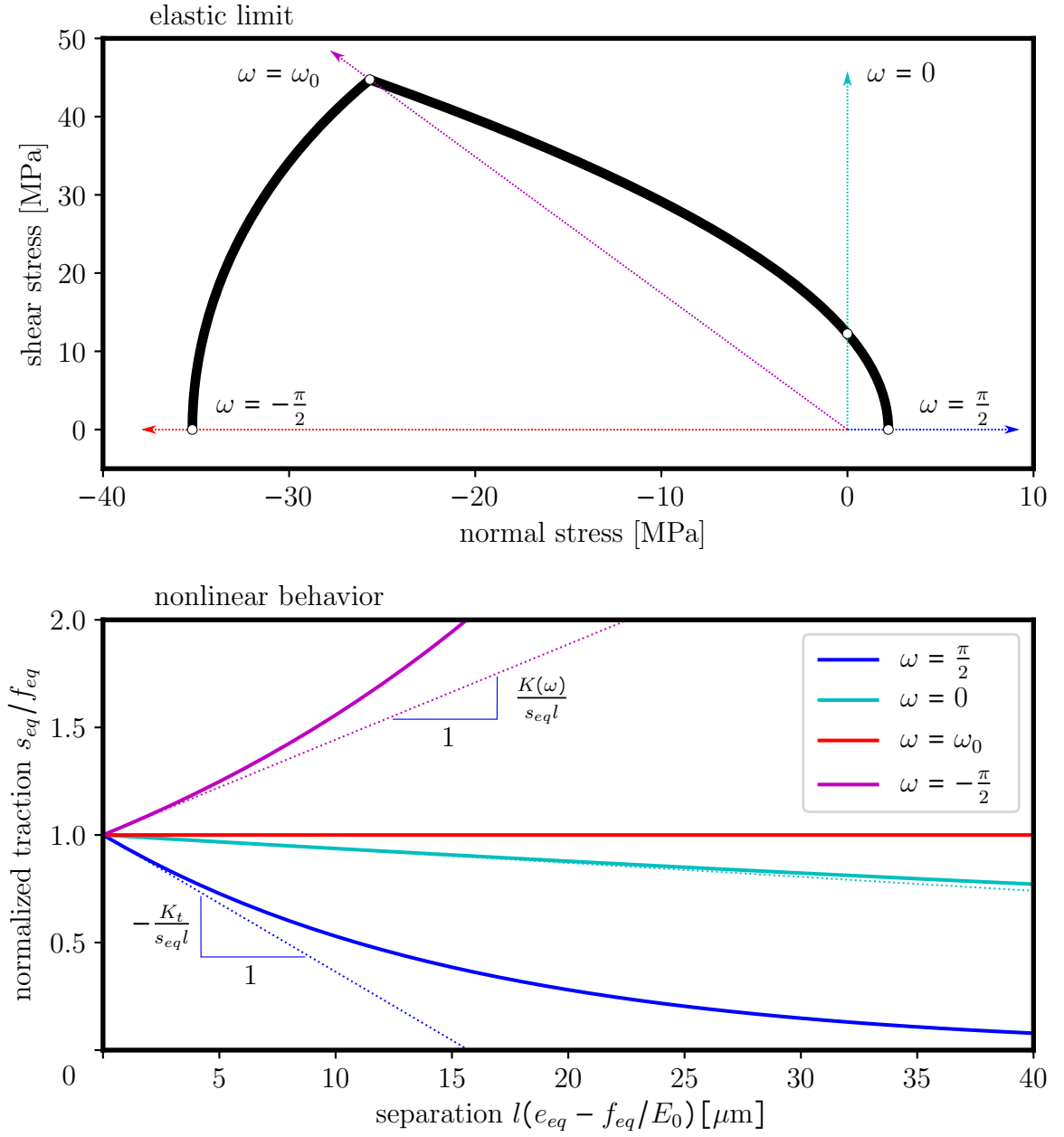


Fig. 3.3: Top: elastic limit in terms of straining direction angle $\omega \in \langle -\frac{\pi}{2}; \frac{\pi}{2} \rangle$; bottom: different post-critical behavior for different angle ω .

ing/hardening curve depends on angle ω , too (see lower part of Fig. 3.3).

$$K = \begin{cases} 0.26 E_0 \left(1 - \left(\frac{\omega + \pi/2}{\omega_0 + \pi/2} \right)^2 \right) & \omega < \omega_0 \\ K_t \left(1 - \left(\frac{\omega + \pi/2}{\omega_0 + \pi/2} \right)^{n_t} \right) & \omega \geq \omega_0 \end{cases} \quad (3.18)$$

Straining direction corresponding to value ω_0 is on the border between softening and

hardening behavior. The exponent from lower part of Eq. 3.18 reads

$$n_t = \frac{\ln(K_t/(K_t - K_s))}{\ln(1 - 2\omega_0/\pi)} \quad (3.19)$$

where K_t and K_s are the initial slopes for tension and pure shear respectively.

$$K_t = \frac{2 E_0 f_t^2 l}{2 E_0 G_t - f_t^2 l} ; \quad K_s = \frac{18 \alpha E_0 f_t^2 l}{32 \alpha E_0 G_t - 9 f_t^2 l} \quad (3.20)$$

The original model has more parameters, e.g. compressive or shear elastic limits. Here, only two governing parameters for material in nonlinear regime are used, namely tensile strength f_t and fracture energy in tension G_t , the remaining parameters are derived from them according to the recommendations (Cusatis and Cedolin, 2007).

Constitutive law at the contact is in Eqs. (3.20) scaled according to the crack band approach (Bažant and Oh, 1983) to ensure constant energy dissipation per unit contact area, independent on particle size.

3.3 Integration of stress over the facet

A displacement jump for a single contact is calculated at the facet centroid as explained in Sec. 3.2.1. Let us call this mechanical model *simple* facet. In this case, all the contact area is lumped into a single point, therefore rotational stiffness is neglected. Perhaps more correct approach would be to integrate stresses over the whole facet continuously accounting also for possible material nonlinearity all over the facet.

Such integration can be performed numerically introducing more integration points over the facet area, where calculation of displacement jump is performed, see Fig. 3.1(d). For example, polygonal facet can be decomposed into triangular sub-domains with common vertex in polygon centroid. Constitutive law is then applied in centroids of all triangles. Using such *discretized* facet, rotational stiffness is, up to some point, preserved and also possible nonlinear behavior is represented in more detail.

In general, any other set of points over the facet area can be chosen. However, one should also take into account increase in computational demand with more integration points.

Here, simple study on uni-axial tensile test and four-point-bent beam is presented. For the purpose of this study, simulations using different particle size dictated by parameter l_{\min} and *simple* or *discretized* facets are performed. Results are

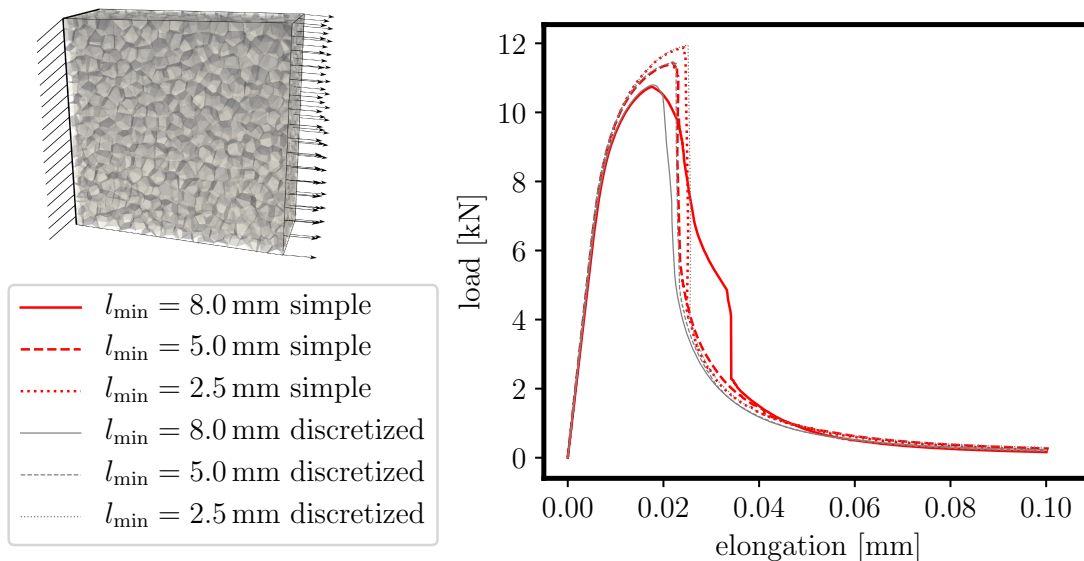


Fig. 3.4: Difference in model results obtained with beam loaded in uni-axial tension.

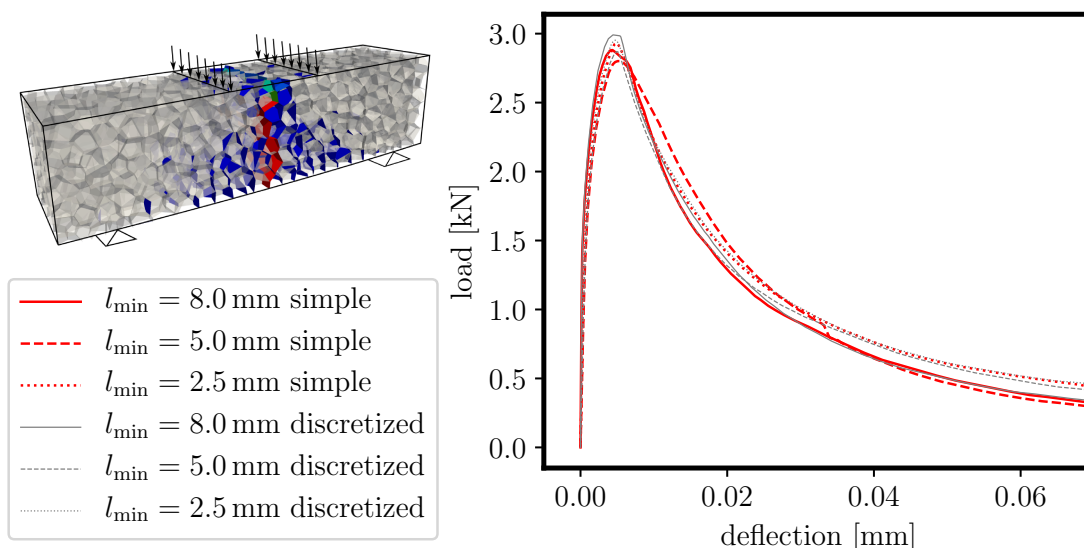


Fig. 3.5: Difference in model results obtained for four point bending test.

plotted in Figs. 3.4 and 3.5. Two longer sides of prism under tension shown in the upper left part of the figure are 100 mm long and its thickness is 40 mm. Bent beam length is 160 mm, depth and thickness 40 mm.

In case of uni-axial tensile test, greater difference is caused by different particle size then by different integration method, see Fig. 3.4. The difference for various particle size used is caused by two facts. First, small influence has the randomness of the internal structure represented by random placement of particle centers in a volume domain. Second the damage is, up to the point of final localization, distributed over the volume domain. In the case of distributed damage, crack band

concept is overestimating results of the numerical simulation (Le and Eliáš, 2016). Greater difference can be observed for the largest used particle size l_{\min} . Note that for this size, there are only 4-5 particles per thickness of the volume domain.

Results of four point bending tests are shown in Fig. 3.5. The simulations using *discretized* facets are predicting higher loading capacity than the ones using *simple* facets. The bending at facet level helps to resist bending at the level of whole specimen. When bending is present, rotational stiffness makes the difference. The graphs also show that when the finer discretization is used, the influence of rotational stiffness decreases.

3.4 Random field

Concrete exhibit spatially fluctuating material properties. Some part of this randomness is included in the discrete model via direct representation of its heterogeneous structure. The remaining part can be conveniently incorporated with help of random field. Single random field $h(\mathbf{x})$ is applied on tensile strength f_t and tensile fracture energy G_t according to (Le et al., 2018)

$$f_t(\mathbf{x}) = \bar{f}_t h(\mathbf{x}) \quad G_f(\mathbf{x}) = \bar{G}_f [h(\mathbf{x})]^2 \quad (3.21)$$

where symbol $\bar{\bullet}$ denotes the mean value of variable \bullet . Since values of many other material parameters are derived from these two via recommendations by Cusatis and Cedolin (2007), random field affects them as well. Distribution function of $h(\mathbf{x})$ is considered normal (Gaussian) with grafted Weibull tail in the left part (Bažant and Pang, 2007). The mean value of h is 1.

Autocorrelation function of $h(\mathbf{x})$ is considered square exponential (Eliáš et al., 2015) with governing parameter called correlation length. The random field is generated initially on regular grid via Karhunen–Loève expansion and than projected onto the model by EOLE method (Li and Der Kiureghian, 1993). The autocorrelation function allows decomposition of the problem into individual directions (Vořechovský, 2008), which greatly simplifies the problem of searching for eigendecomposition of covariance matrix.

Randomness of material properties is not a subject of this thesis, it is only used for a particular studies of parameters influence.

Part II

Fiber reinforced concrete

4 FIBERS AND CONCRETE

It is well known that plain concrete suffers from poor performance in tension, therefore it is usually reinforced with steel rebars that help transfer tensile stress. However, steel tends to corrode when not sufficiently protected. Such a protection demands quite thick concrete layer. Great progress has been done in a past decades on improving the poor performance of concrete in tension by adding short fibers.

4.1 Cementitious composites with fibers

One of the possible ways of enhancing the tensile properties of concrete-based materials is to add short fibers as a reinforcement. Use of tiny fibers can lead to a significant increase in composite tensile performance. Then, the material can be used also for very thin structural members.

Various types of fiber materials are used in this field. For example, industrial floors are nowadays typically reinforced by steel fibers. The modern development of so called *engineered cementitious composites* (ECC) also reflects the advantages of plastic materials as a fiber reinforcement. Tiny *poly-vinyl alcohol* (PVA) fibers are considered as a very good choice thanks to their flexibility and rough surface promising good slip-frictional behavior. Their frictional resistance can be so high that it is necessary to coat them in oil to ensure that they are pulled out instead of being broken (Yang et al., 2008b; Li et al., 2001; Redon et al., 2001). One of the ideas behind the design of these materials is to increase strain capacity. Loaded specimen is, after initial cracking, further able to transfer increasing value of load. That is the reason why they are also referred to as *strain hardening cementitious composites* (SHCC). Strain hardening behavior is obtained only if crack density is high, than, overall elongation of specimen is distributed in whole volume (Adendorff et al., 2009). Higher crack density can be obtained using artificial flaws (Li and Wang, 2006).

Amount of fibers in material volume is important. According to Fantilli et al. (2009) volume fraction around 2% ensures multiple cracking with sufficient crack density, which leads to strain hardening behavior. On the other hand, excessive volume fraction reduces workability of the raw material, which can lead to formation of fiber clusters that cause reduction of bond between fibers and cement paste which results in poor composite performance.

Many factors affect resultant composite behavior. Influence of some material properties go against each other, e.g. greater tensile strength of cement paste increases the maximum loading capacity on one side, but reduces the strain capacity

of composite on the other side, because the fibers are not able to transfer higher load and break. Also if fibers are too long, they break instead of being pulled out.

4.2 Fiber representation in computational model

Progress in development of new, enhanced materials requires also a progress in the field of computational mechanics to be able to predict their behavior. Short fiber reinforcement influence material behavior at the meso – or even lower – scales. Furthermore, heterogeneity of the material is increased by the presence of fibers. In homogeneous model, this needs to be taken into account phenomenologically.

To determine such phenomenological description, discrete model with higher resolution can be conveniently used. There are more possibilities of fiber representation in discrete models. In case of low-scale lattice model, different elements can

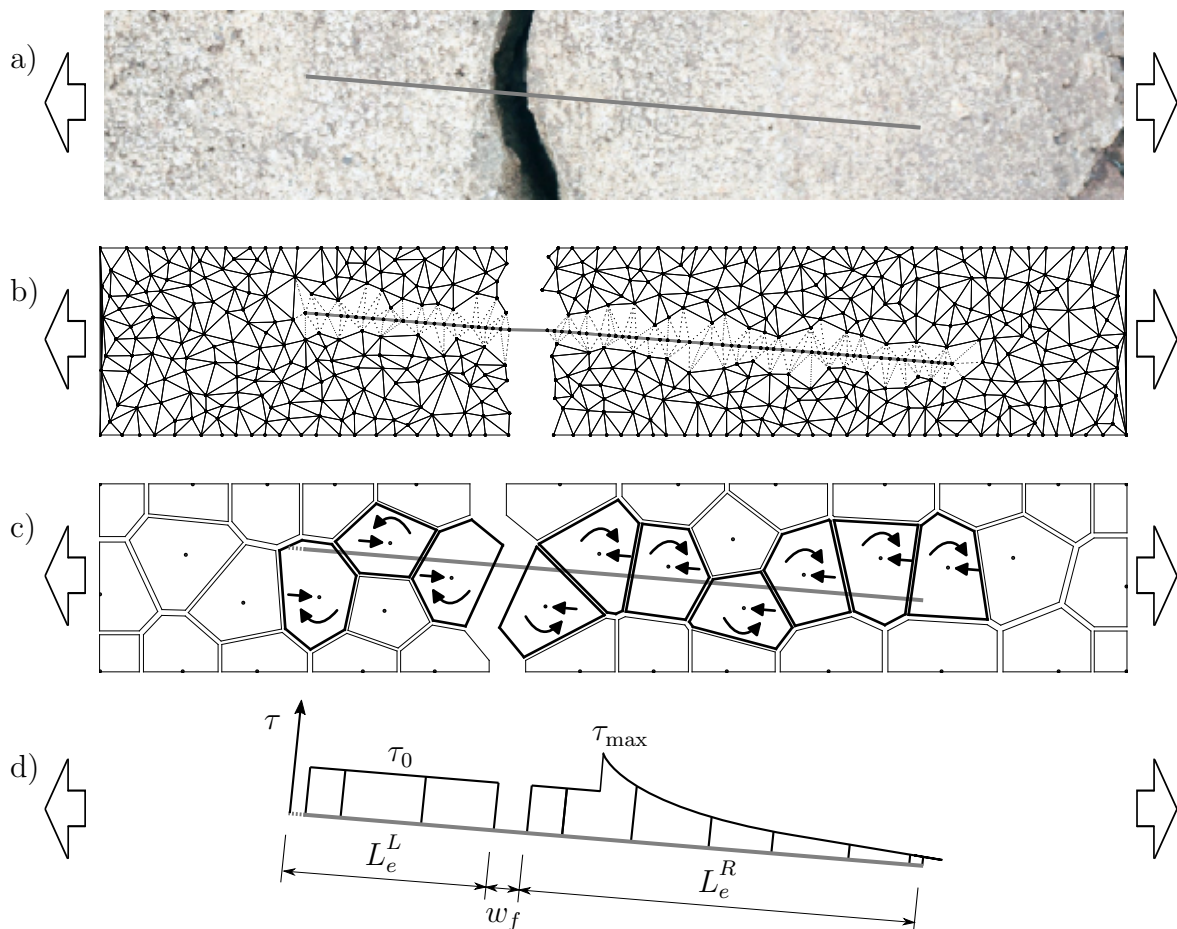


Fig. 4.1: (a) fiber bridging crack in material, (b) representation of different material phase in lattice model, (c) indirect fiber representation in discrete particle model and (d) frictional and bond stress distribution along the fiber length.

be used for fiber, cement paste and bond between them (Bolander et al., 2008), see Fig.4.1(b). At higher scales, phenomenological description can be used in discrete models as well. The constitutive law of particular facet can be adjusted according to the number of fibers crossing it. In case of the presented meso-scale discrete particle model, the fibers can be represented by additional elements connected to the meso-scale structure. However, such direct representation brings large increase in number of DOFs, because the amount of fibers is in tens of thousands even for small laboratory specimen made of composite reinforced with PVA fibers with volume fraction 2%.

It appears to be convenient to take into account only frictional forces of fiber bridging crack in the material. These forces are then distributed into particles that are crossed by particular fiber (Kang et al., 2014) as depicted in Fig. .4.1(c). In this thesis, pullout frictional resistance is for the sake of simplicity applied at contact only as a crack closing force. In that case, number of DOFs is not increased and at the same time every single fiber is taken into account.

Particle models incorporating fiber reinforcement are used by Jin et al. (2016) for simulations of steel fiber reinforced concrete or by Schaufert and Cusatis (2012) for simulations of PVA reinforced composites.

5 FIBERS IN MESO-SCALE MODEL

Phenomenological description of fiber pullout force is broadly reported in literature, though, most of the cases refer to the work of Naaman et al. (1991). The mentioned article provides an insight into two main stages of fiber pullout, debonding and pullout slip.

5.1 Fiber bridging force

There is a significant difference between behavior of a single fiber that is being pulled out from a material on one side and fiber that is bridging crack on the other side. The former is so called one-sided pullout, the later two-sided pullout.

According to Naaman et al. (1991), the following relation between pullout slip v and force $P(v)$ due to fiber resistance is described (Schauffert and Cusatis, 2012; Yang et al., 2008b),

$$P(v) = \begin{cases} \sqrt{\frac{\pi^2 E_f d_f^3}{2} (\tau_0 v + G_d)} & \text{for } v \leq v_d \\ P_0 \left(1 - \frac{v-v_d}{L_e}\right) \left[1 + \frac{\beta_f(v-v_d)}{d_f}\right] & \text{for } v > v_d \end{cases} \quad (5.1)$$

$$v_d = \frac{2\tau_0 L_e^2}{E_f d_f} + \sqrt{\frac{8G_d L_e^2}{E_f d_f}} \quad (5.2)$$

$$P_0 = \pi L_e d_f \tau_0 \quad (5.3)$$

Here, d_f denotes fiber diameter, v is fiber pullout and L_e is an embedment length, see Fig. 5.1. Parameters of the fiber constitutive law are: frictional stress between fiber and surrounding matrix τ_0 , fiber elastic modulus E_f , bond fracture energy G_d and parameter β_f describing the slipping behavior of debonded fiber. $\beta_f = 0$ refers to constant slip frictional behavior, whereas negative or positive value is used

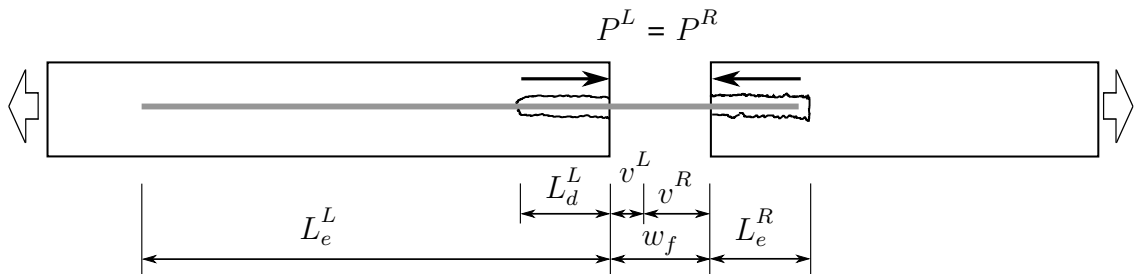


Fig. 5.1: Crack length divided into pullout on each side according to different stage of fiber behavior – debonding on the left, pullout on the right. Superscripts R and L refer to the right and left side of the crack respectively.

when softening respectively hardening slip behavior is considered. Critical pullout v_d (pullout at complete debonding of considered fiber part) is described by Eq. (5.2).

It has been reported that frictional behavior of fully debonded PVA fibers tends to increase (Li et al., 2002). This phenomenon is caused by rough surface of such fibers, that is being scraped off by surrounding material during pullout. Such behavior can be approximately characterized by positive value of parameter $\beta_f > 0$.

The stated relation describes a one-sided pullout, the two-sided pullout behavior is schematically depicted in Fig. 5.1. A crack propagates through material over the fiber. To determine crack bridging force, crack width w_f is divided into two parts, belonging to each fiber part on both sides of the crack. With increasing crack width, two of the fiber parts are partially debonded ($v < v_d$). The shorter embedment lengths L_e^R is fully debonded first. The debonded part is still resistant against pullout, but only due to friction between fiber and matrix – Eq. (5.1). Different part of crack w_f is assigned to pullout from the left v^L or the right side v^R of the crack, see Fig. 5.1. Calculation of bridging force is an iterative process, in which an equilibrium between forces from both sides of the crack must be reached.

5.2 Multiple cracking

When the fiber bridges multiple cracks, the interaction needs to be taken into account. The value of debonded length from another crack that is crossed by the same fiber is needed. Eq. (5.2) describes the value of critical pullout v_d according to embedment length L_e . It can be rewritten for unknown L_e

$$\frac{2\tau_0}{E_f D_f} L_e^2 + \sqrt{\frac{8G_d}{E_f d_f}} L_e - v_d = 0 \quad (5.4)$$

Solution of this quadratic equation can be found with a value of the actual pullout v instead of v_d . Then, the value of actual debonded length L_d can be obtained according to

$$L_d = \frac{\sqrt{2E_f d_f}}{2\tau_0} \left(\sqrt{G_d + \tau_0 v} - \sqrt{G_d} \right) \quad (5.5)$$

To calculate the critical value v_d (slip at full fiber debonding), embedment length is reduced of debonded lengths due to other cracks.

When multiple cracking occurs over one fiber, both ends of a fiber are connected through the particles they are crossing. If the middle particle is fully separated by cracks and its part of fiber is fully debonded, it should be able to move independently on surrounding particles, only due to friction. Because the fibers are in the model approximately represented only by their frictional forces, this case is not captured.

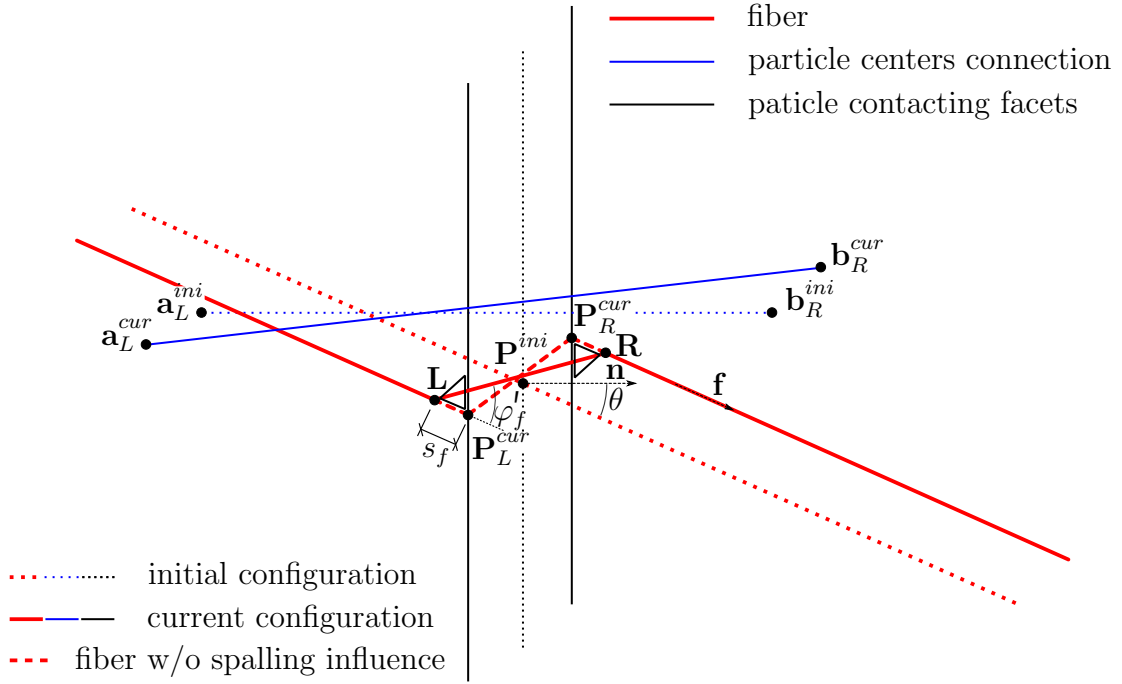


Fig. 5.2: Schematic explanation of angles used in Eqs.(5.8-5.10).

5.3 Micro-effects at fiber exit point

When the fiber is not parallel with the normal facet direction, micro-spalling of the cement matrix occurs in the vicinity of fiber exit point.

The fiber inclination is schematically depicted in Fig. 5.2, where one contact of two neighboring particles is shown in its initial and deformed (current) configuration. Calculation of angle φ_f^i is performed according to

$$\varphi_f^i = \arccos \frac{(\mathbf{R} - \mathbf{L})^T \mathbf{f}}{\|\mathbf{R} - \mathbf{L}\| \|\mathbf{f}\|} \quad (5.6)$$

where \mathbf{f} is fiber direction and points \mathbf{R} and \mathbf{L} are fiber exit points for particles on right and left sides of a crack respectively. Taking into account spalling length, these points differ from the fiber exit point \mathbf{P} . Their subtraction can be calculated from

$$\mathbf{R} - \mathbf{L} = 2 (\Delta \mathbf{u}_{ab}/2 + s_f \mathbf{f}) \quad (5.7)$$

where $\Delta \mathbf{u}_{ab}$ is a displacement jump between particles, s_f refers to spalling length and \mathbf{f} is fiber direction.

The embedment length is reduced of spalling length s_f that is, according to

Schauffert and Cusatis (2012), calculated as

$$s_f = \frac{P_N \sin(\theta/2)}{k_{sp} f_t d_f \cos^2(\theta/2)} \quad (5.8)$$

where P_N is the normal component of crack bridging force, k_{sp} is spalling coefficient, θ is angle between facet normal and fiber and f_t is meso-scale tensile strength of cement matrix.

Inclination of fiber at exit point also causes additional friction and bearing between fiber and matrix. Schauffert and Cusatis (2012) refer to this as a snubbing effect that increases the resistance of a fiber against pullout. The following relation is used to take this phenomenon into account.

$$P_f = \exp(k_{sn} \varphi_f') P(v) \quad (5.9)$$

Here, φ_f' is the angle between fiber and straining direction reduced by spalling length, see. Fig. 5.2, k_{sn} is snubbing coefficient.

Together with increase of the fiber pullout resistance, the fiber strength is reduced due to “bending” of an inclined fiber at the exit point (Schauffert and Cusatis, 2012; Yang et al., 2008b).

$$f_{tf_{incl}} = f_{tf} \exp(-k_{rup} \varphi_f') \quad (5.10)$$

where f_{tf} stands for fiber tensile strength and k_{rup} is material coefficient.

The influence of parameters k_{sp} , k_{sn} and k_{rup} on the spalling length, increase of pullout force and decrease of fiber strength is shown in Fig. 5.3.

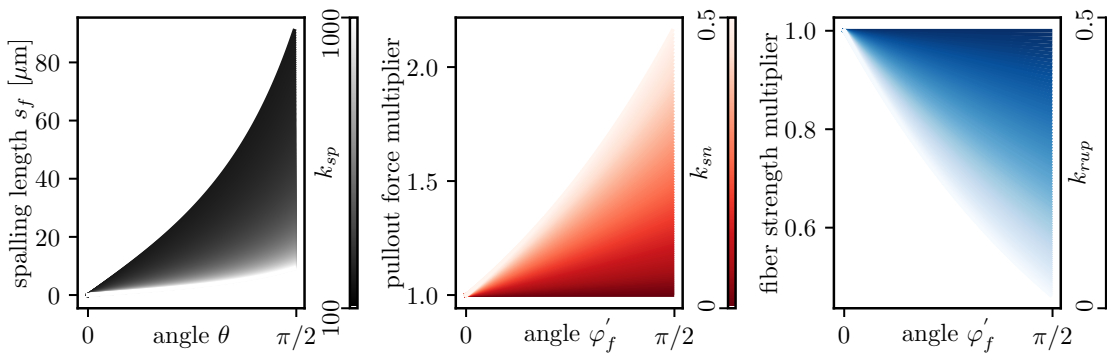


Fig. 5.3: Influence of parameters describing micro-scale fiber behavior – Eqs. (5.8-5.10)

5.4 Fibers in discrete model

For elastic behavior, fibers contribution to the stiffness of the system is neglected. Single fiber is taken into account only if it bridges any contact of particles undergoing fracture. When cracking occurs in the material, every fiber that crosses some crack is visited, bridging force is calculated and stiffness of the cracked contact is modified accordingly.

In nonlinear regime, stiffness of particle contacts is increased by contribution due to fiber bridging force. Meso-scopic contact stress s_{eq} used for calculation of damage – Eq. (3.14) – is then calculated as a sum of contributions of both concrete (s_{eq}^c) and fiber (s_{eq}^f)

$$s_{\text{eq}} = s_{\text{eq}}^c + s_{\text{eq}}^f \quad (5.11)$$

s_{eq}^f is calculated from crack bridging force acting against crack opening on a virtual facet placed in the point of intersection between fiber and particle contact. This virtual facet area then corresponds to fiber cross-section.

A fiber behavior is assumed to be elasto-brittle and ideally flexible. Each fiber is simplified by a straight line of a certain length. These lines are generated within volume of the specimen with prescribed or random orientation. Fibers with random orientation are directionally biased close to the boundary, because only fibers inside the specimen are allowed. If any part of generated fiber appears outside the prescribed volume domain, it is removed and a new fiber is generated instead.

6 NUMERICAL SIMULATIONS

6.1 Two sided pullout

A simple study of two sided pullout was conducted. The contact of two particles is crossed by a fiber. The two particles have all DOFs prescribed to 0 except the right particle horizontal displacement prescribed to v . The contact facet is pre-cracked from the beginning to show only the pullout representation.

For this demonstrative example, the following material parameters were used. Fiber elastic modulus $E_f = 30$ GPa, fiber length $l_f = 10$ mm (and $2l_f$ for long fiber) with 35% of fiber length on the right side of the contact, fiber diameter $d_f = 40$ μ m, energy needed for fiber debonding $G_d = 5$ N/m, friction between fiber and cement paste $\tau_0 = 2$ MPa after debonding and parameter $\beta_f = 0$ for constant friction or $\beta_f = \pm 0.01$ for increase respectively decrease of frictional resistance. Fiber strength is $f_{tf} = 1000$ MPa

The influence of fiber parameters is shown in Fig. 6.1. Nonzero bond fracture energy (thin lines) brings instant drop in fiber force after debonding. If the fiber is too long, it breaks instead of being pulled out (red line).

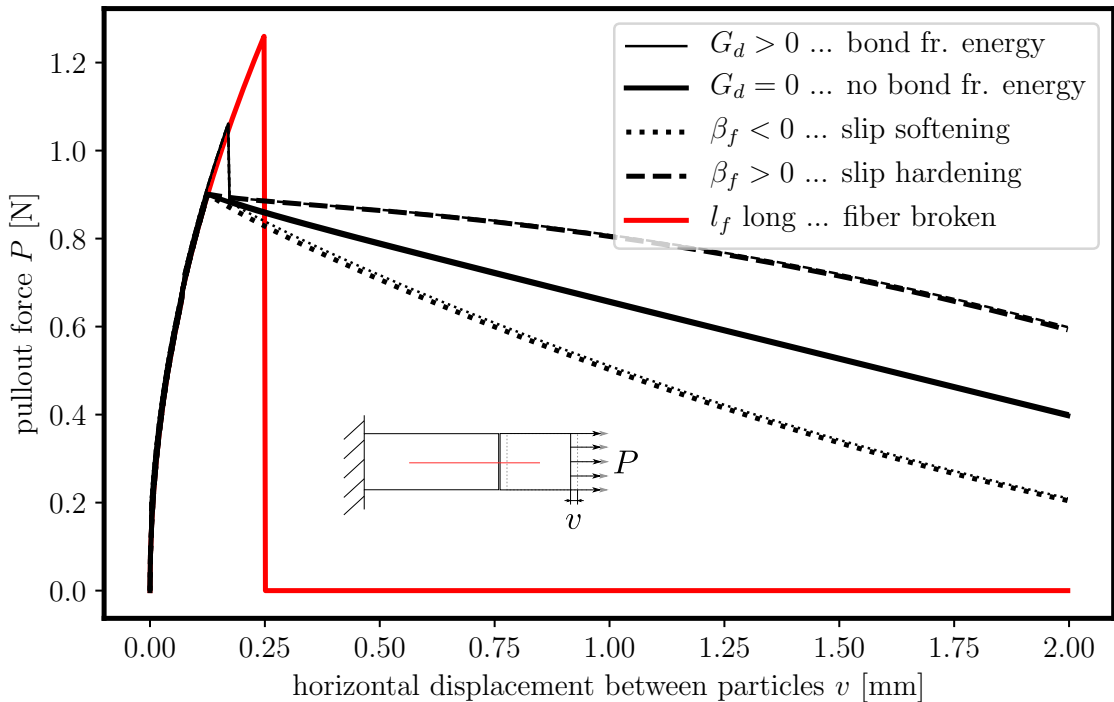


Fig. 6.1: Influence of material parameters to results of two-sided pullout simulation.

6.2 Volume fraction effect

After single fiber pullout, the influence of number of fibers n_f crossing a single contact was investigated. The same geometry as in case of pullout test was used, but this time the contact was not pre-cracked. Simulations with 1, 2, 10 and 20 fibers crossing the contact were calculated. Fiber volume relative to the whole volume is denoted volume fraction V_f . In this case of a single contact, it is calculated from fibers cross-section relative to the facet area. The results of simulations are shown in Fig. 6.2. The model responses are shown also in semi-logarithmic plot. For comparison, response of contact without fibers is plotted in black. For all cases, after the contact reaches the elastic limit, sudden drop occurs. This is caused by the fact that the fiber pullout force depends on crack opening, which is zero at the crack initiation. If the bond fracture energy G_d is nonzero (dotted lines), the initial peak (before the first drop) is higher, because the fiber pullout force according to Eq. 5.1 does not start at zero $P(v=0) = \sqrt{0.5 \pi^2 E_f d_f^3 G_d}$. The second peak, long after the crack has been created, is higher due to G_d as well. There is no sudden drop as in the case of single fiber pullout, because the fibers have different embedment lengths. After the initial drop, loading force further increases, however, only for $V_f > 1\%$ the force exceeds the initial peak. To ensure strain hardening behavior in fiber reinforced cementitious composites, the volume fraction $V_f = 2\%$ is recommended in literature (Fantilli et al., 2009).

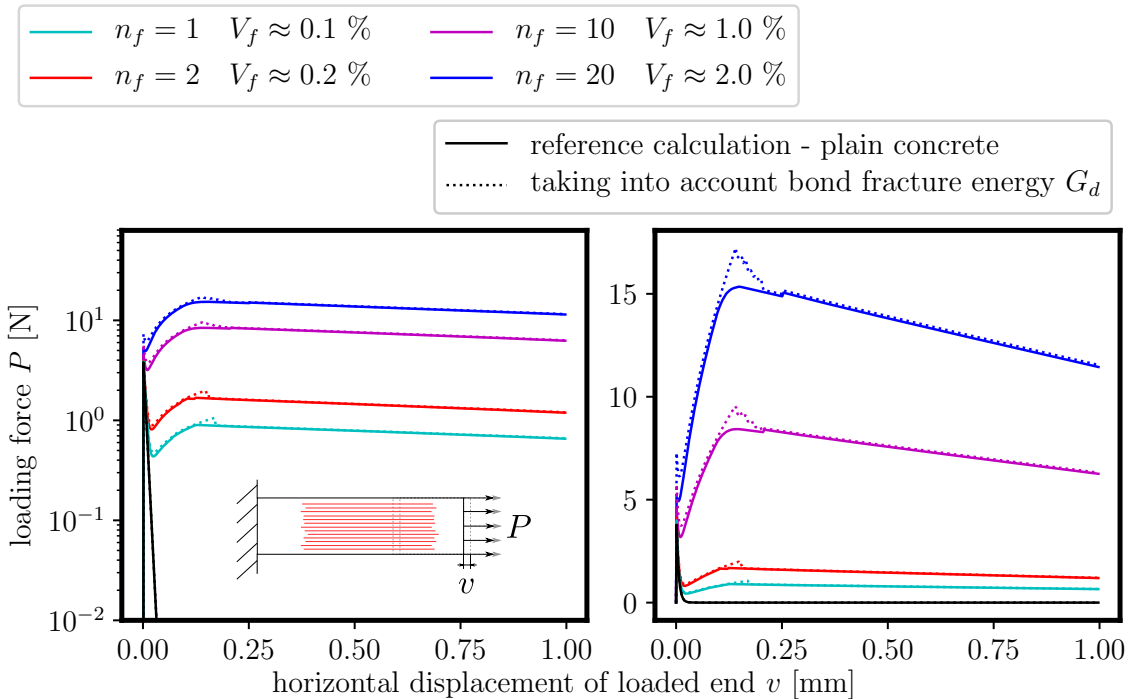


Fig. 6.2: Influence of fiber volume fraction on a single contact response.

6.3 Preliminary study on uniaxial tensile test

Simple uni-axial tensile test of a prismatic beam was performed. Again, various model settings were used, including concrete and fiber material parameters as well as fiber orientation. Setting of the model is shown in Fig. 6.3.

Beam length was $L = 60$ mm, width $W = 20$ mm and thickness $T = 10$ mm. Parameter $l_{\min} = 2.5$ mm. The results of simulations shown in Fig. 6.4 were obtained using the following material parameters: fiber elastic modulus $E_f = 30$ GPa, bond fracture energy $G_d = 0$ or 5 N/m, frictional stress $\tau_0 = 2$ MPa, parameter $\beta_f = 0$, fiber length $l_f = 10$ mm and fiber strength $f_{tf}^0 = 1000$ MPa. Concrete meso-scale parameters used here are $E_0 = 48$ GPa, parameter $\alpha = 0.237$, concrete tensile strength $f_t = 3.8$ MPa and fracture energy dictating the quasi-brittle behavior $G_f = 20$ J/m². Special case of elasto-brittle concrete behavior is considered as well.

The simulated load-displacement curves are shown in Fig. 6.4. Reduction of fiber strength results in their breakage instead of pullout (dotted lines). As expected, lower forces values are obtained with zero bond fracture energy (lines with cross mark), furthermore, these results does not exhibit instantaneous drop-down after second peak as in the case of nonzero G_d . Response using elasto-brittle contact behavior (thin lines) has quite smoother transition to hardening after the initial crack-

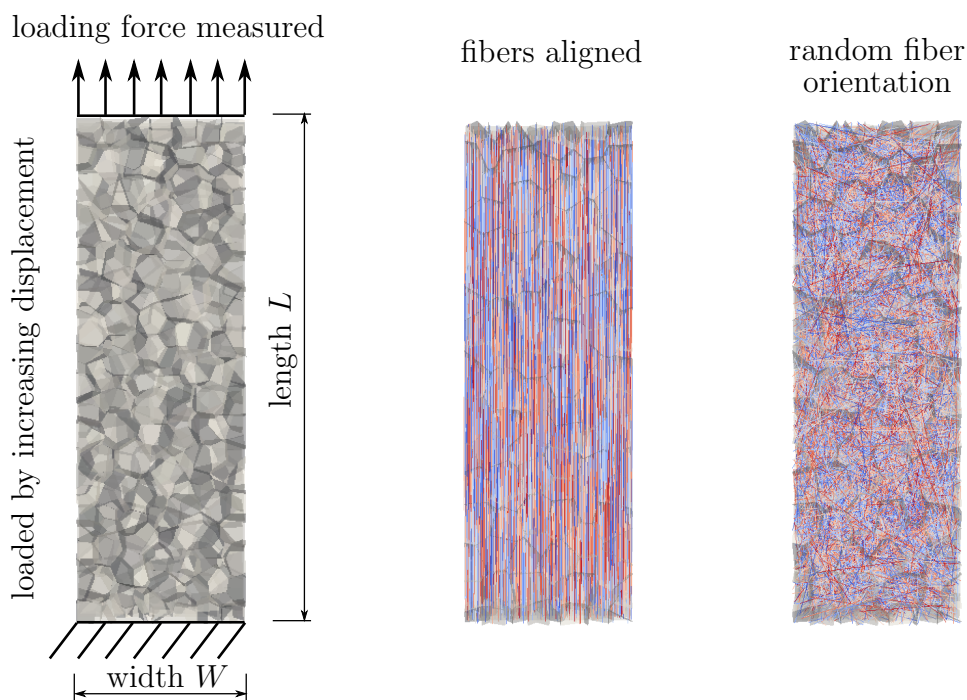


Fig. 6.3: Settings of uni-axial tensile test with fibers aligned with loading direction or randomly oriented.

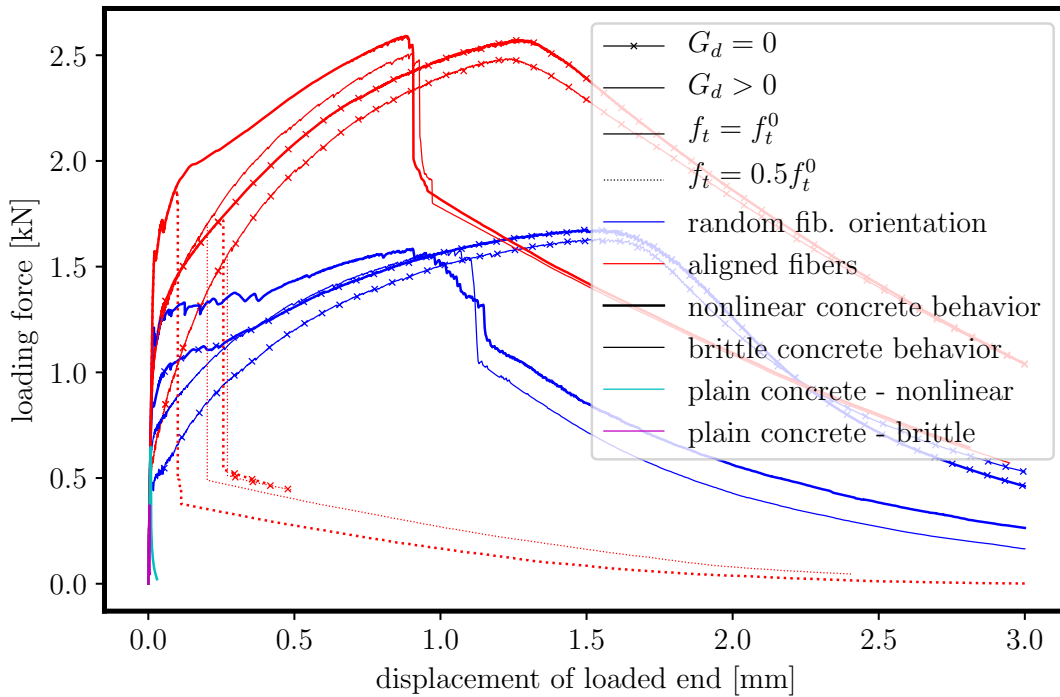


Fig. 6.4: Influence of material parameters to results of uni-axial test simulation of prism made of fiber reinforced composite.

ing compared to responses with nonlinear constitutive law used for concrete (thick lines). Finally, the fibers aligned in a loading direction (red lines) give much higher loading capacity than the ones randomly distributed (blue lines). Since straight alignment is barely possible in reality, any further calculations are performed with randomly oriented fibers. Responses of plain concrete assuming elasto-brittle and nonlinear behavior are plotted for comparison.

The meso-scale model assumes small deformations and rotations for representation of rigid body motion as stated in Sec. 3.2. Having displacement in order of millimeters for a specimen of length 60 mm, the assumption is not really correct. In this case, at least the deformation is distributed into a whole volume, and not localized into a single crack.

6.4 Detail study on model parameters influence

The preliminary study showed influence of bond energy and fiber length that needs to be taken into account. In this section, series of simulations with various material parameters is presented.

Initially, the sensitivity study on influence of five model parameters was conducted. Results are shown in Fig. 6.5 as a normalized relative change in the model

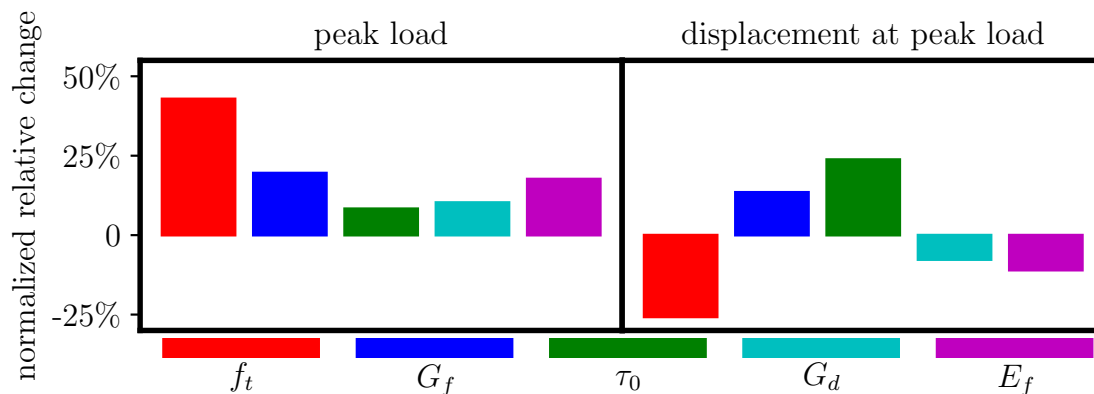


Fig. 6.5: Sensitivity of loading and straining capacity to model input parameters.

response based on change in different parameters. Since the calculations are quite computationally demanding, simple sensitivity study using fractional factorial design (Montgomery, 2017) was performed. The left graph shows that increase in any of these five model parameters results in greater peak load predicted by the model. On the other hand, the right graph shows the effect of parameter changes to the predicted straining capacity. Three of the parameters influence the results negatively, namely concrete strength f_t , bond fracture energy G_d and fiber elastic modulus. Different influence of the material parameters would be obtained for the case when fibers break instead of being pulled out.

Further parameter studies are performed to show more than this simple sensitivity. Larger beams than in the case of preliminary study (sec. 6.3) are simulated. This time, length was $L = 120$ mm, width $W = 40$ mm and thickness equal to $T = 10$ mm. Fibers of length $l_f = 8$ mm were used. Material parameters used are the following: concrete parameters $E_0 = 48$ GPa, $\alpha = 0.237$, $f_t = 1.5$ MPa and $G_f = 20$ J/m²; fiber parameters: $E_f = 20$ GPa, $f_{tf} = 1000$ MPa, $G_d = 5$ N/m, $\tau_0 = 2$ MPa and $\beta_f = 0$. Simulations using these values are plotted with magenta color.

Lower concrete strength was chosen because the sensitivity study showed its negative influence on predicted straining capacity. This negative influence will be emphasized in Sec. 6.5 on simulations using random spatial distribution of concrete strength.

6.4.1 Influence of concrete strength

Based on comparison of the simulations considering plain and fiber reinforced concrete in Fig. 6.4, it seem that the concrete itself has a very little effect. However, simulations of fiber reinforced composite considering brittle or nonlinear concrete behavior show that this influence has quite a large impact.

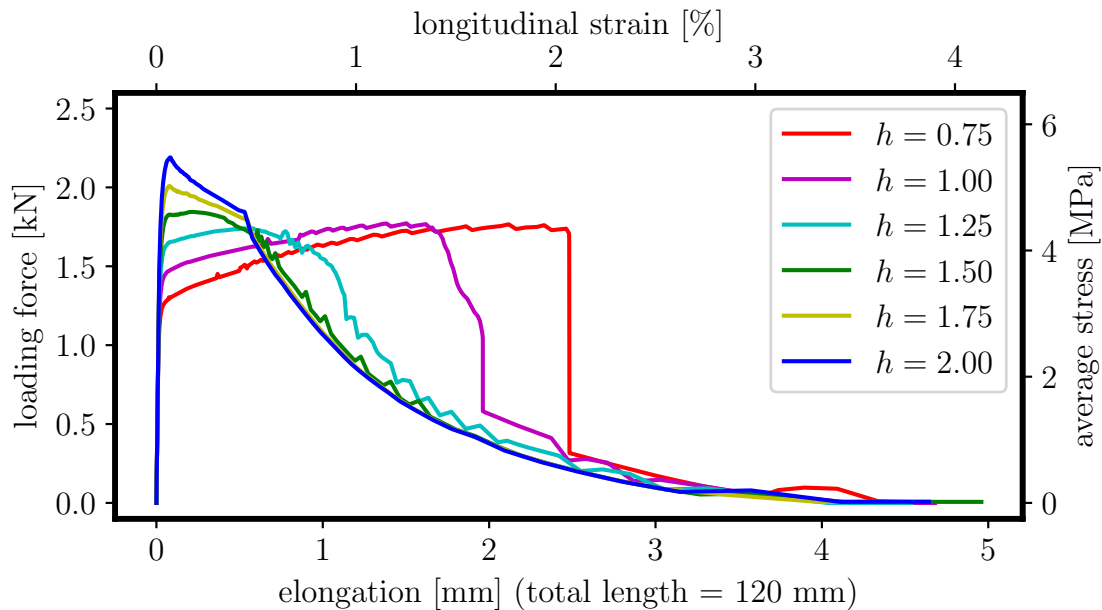


Fig. 6.6: Influence of concrete parameters.

For this purpose, more simulations were calculated using lower concrete strength and fracture energy. The material strength was scaled similarly to application of random field – Eq.(3.21), but the function $h(\mathbf{x})$ is kept constant in space (for interpretation, see Sec.3.4). The results plotted in Fig.6.6 show the influence of concrete strength to material response predicted by the numerical model. If the higher strength is assumed for concrete, the predicted loading capacity is higher. Even though the post-peak behavior is more ductile than in case of plain concrete, strain-hardening response is not obtained. This happens for simulations with lower concrete strength. In that case, multiple cracking occurs.

6.4.2 Influence of frictional parameters

Influence of frictional stress τ_0 between fiber and matrix is addressed here. The results of simulations using wide range of values τ_0 are plotted in Fig.6.7. Using frictional stress $\tau_0 > 1.5$ MPa the model predicts strain-hardening response. We also focus on the parameter β_f that describes increase/decrease of friction during fiber pullout and change its value to 0.5. We can see that τ_0 influences mainly the initial angle of strain-hardening/softening behavior. Using positive value for parameter β_f , strain capacity predicted by the numerical model is increased. But combination of higher values of both τ_0 and β_f results into too high force that leads to fiber breakage instead of pullout.

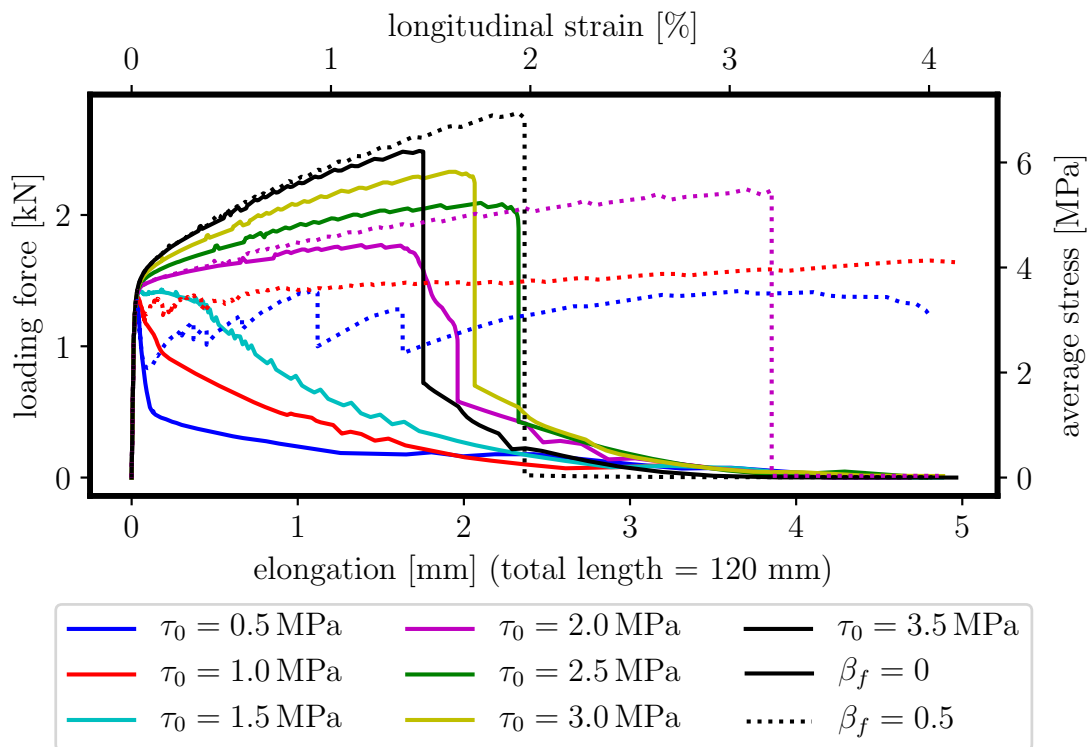


Fig. 6.7: Influence of shear stress between fiber and matrix τ_0 and hardening parameter β_f .

6.4.3 Influence of micro-effects

In the previous simulations, influence of micro-spalling at the fiber exit point was not taken into account. In Fig. 6.8, various values of these parameters are used to show how they affect the model behavior. Parameters used for simulation of reference spalling were $k_{rup} = 0.33$, $k_{sn} = 0.1$ and $k_{sp} = 500$. These values are considered according to Schaufert and Cusatis (2012). Three more calculation are performed here, each one considering half value for one of the parameters and for comparison the calculation with no micro-effects taken into account is added. It can be observed that considering micro-effects results into prediction of higher initial peak but this also leads to earlier collapse of the simulated specimen. Considering half value of parameter managing spalling length, k_{sp} , does not have much influence on the model results. Change in two other parameters, k_{rup} and k_{sn} has noticeable influence. The former affects the fiber strength, therefore, decreasing this parameter leads to higher strength and thus later fiber breakage that results in higher both loading and straining capacity. The latter influences the pullout force, so its reduction decreases fiber pullout force, which leads to decrease in the peak load but increase in the straining capacity.

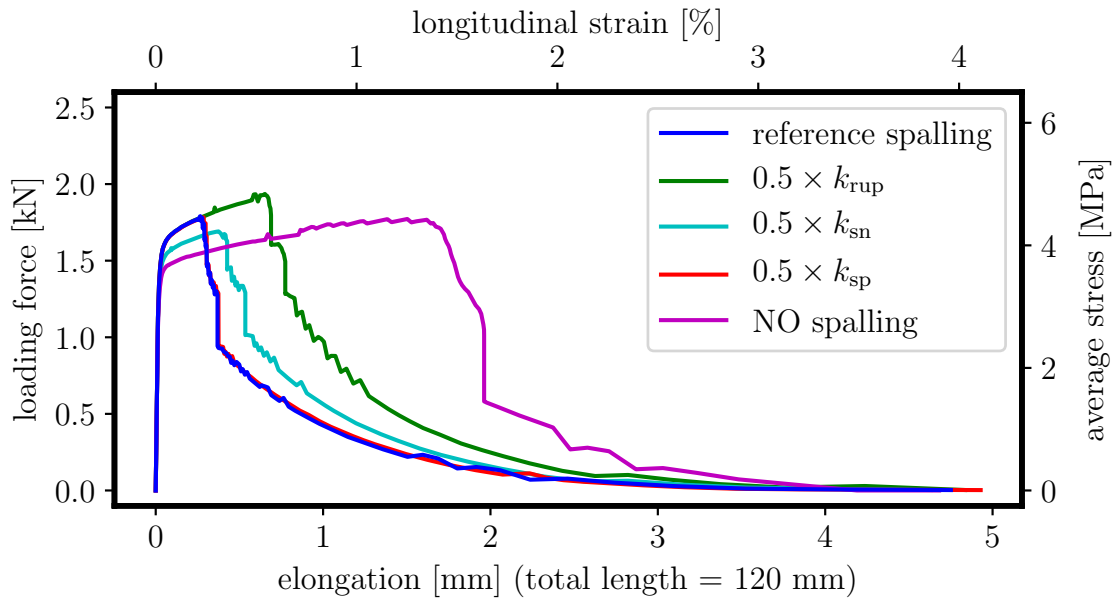


Fig. 6.8: Influence of parameters related to micro-spalling at the fiber exit point.

6.5 Random concrete strength

In the final study, a random field was applied to concrete material properties. This time, simulations on prisms with the following dimensions were performed: length $L = 100$ mm, width $W = 40$ mm and thickness $T = 10$ mm. Material parameters from Sec. 6.3 are used, only the fiber length and strength are changed to $l_f = 8$ mm and $f_{tf} = 1600$ MPa. Concrete parameters f_t and G_f vary over the volume domain according to auto-correlated random field (sec. 3.4). The auto-correlation length is $l_c = 20$ mm and the standard deviation is 0.25. Load-displacement curves from the simulations are shown in Fig. 6.10 together with crack pattern at the final stage and different random fields applied. Only one simulation exhibits the desired strain-hardening behavior, i.e. a further increase of the loading capacity after initial cracking. This simulation marked as No. 10 is the one calculated with relatively weak concrete, almost all volume has strength around 1/2 of the mean value depicted by dark blue color. This corresponds to the effect of concrete strength presented in Sec. 6.4.1

6.6 Comparison to experimental data

Experimental series reported by Li et al. (2001) was chosen for comparison of the model prediction. In this series, coupon specimens of dimensions $304.8 \times 76.2 \times 12.7$ mm were subjected to tensile tests after 28 days of curing in water at room

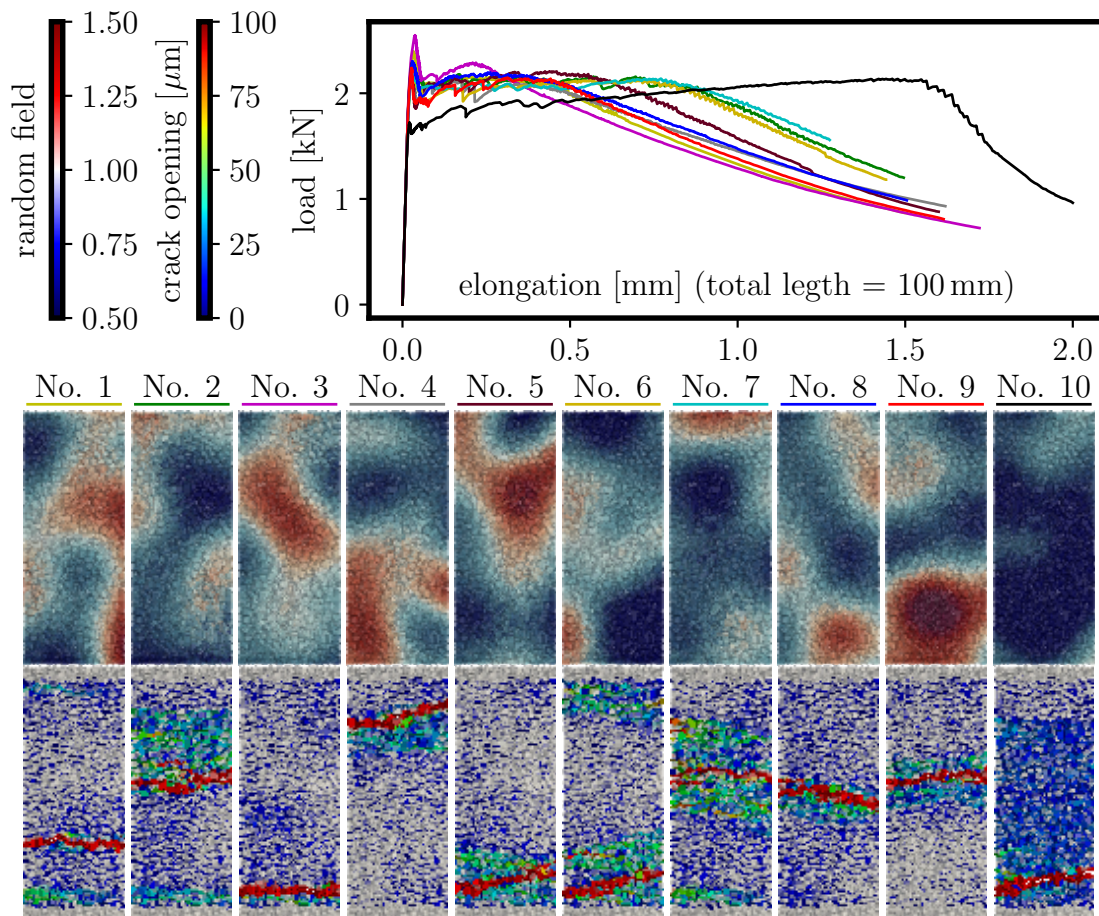


Fig. 6.9: Application of random field on concrete material parameters; top: load-displacement curves, center: spatial fluctuation of concrete strength, bottom: crack pattern at the final stage.

temperature. Water to cement (w/c) ratio was the same for all the batches and its value was 0.45. Fibers parameters reported in experimental series (Li et al., 2001) are: fiber strength $f_{tf} = 1660$ MPa, fiber elastic modulus $E_f = 42.8$ GPa, frictional stress $\tau_0 = 3.5$ MPa and bond fracture energy $G_d = 3.5$ J/m². Fiber volume fraction is $V_f = 2\%$, fiber diameter $d_f = 39$ μ m and fiber length $l_f = 12$ mm. Fibers were coated with oil to ensure their pull-slip behavior and prevent their breakage. The experiments with 0.3% of oil volume content were chosen for comparison.

For numerical simulations, the geometry of the fibers, volume fraction and tensile strength were chosen according to the experimental data. The other parameter values were chosen to obtain response comparable to the experimental results. Their values are: concrete meso-scale parameter elastic modulus $E_0 = 48$ GPa, parameter $\alpha = 0.237$, tensile strength $f_t = 0.75$ MPa, fracture energy $G_f = 5$ J/m² and $l_{\min} = 3$ mm; parameters related to fiber are fiber elastic modulus $E_f = 20$ GPa, bond fracture energy $G_d = 2$ J/m², friction $\tau_0 = 1$ MPa and parameter $\beta = 0.05$.

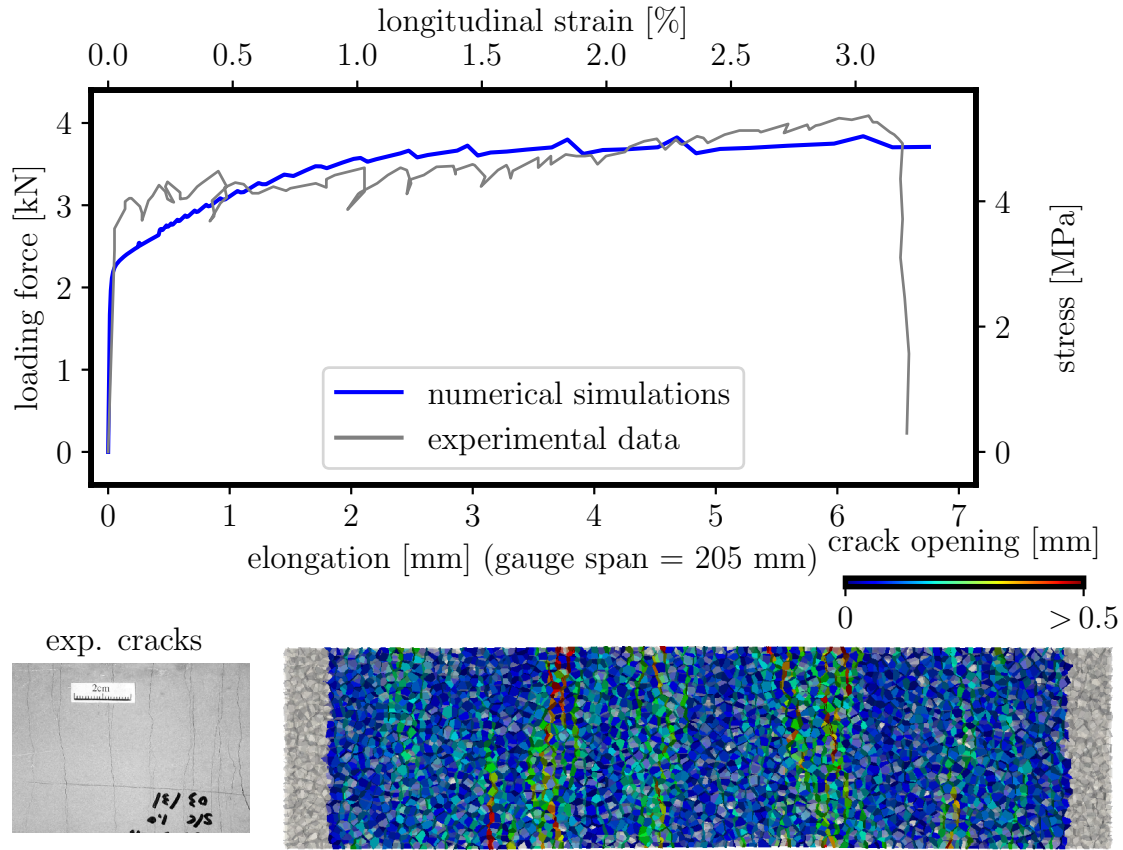


Fig. 6.10: Comparison of the numerical load-displacement curves and crack patterns with the experimental data reported by Li et al. (2001).

Parameters accounting for micro-effects at the fiber exit point k_{sp} , k_{sn} and k_{rup} are 500, 0.2 and 0.33 respectively.

The load-displacement curves of numerical simulations compared to the experiments performed by Li et al. (2001) are plotted in the upper part of Fig. 6.10. The lower part of the figure shows crack pattern obtained by the numerical model. Crack spacing from experiments (Li et al., 2001) is shown for comparison. In case of quite large elongation and multiple cracking, the simulations often end up with the loss of convergence, which is considered as a final collapse. No drop is plotted in the graph, since at the last step the model terminated due to convergence problems.

6.7 Conclusions about the fiber model

The parameters of the mathematical model are related to the actual physical phenomena of the material behavior at meso-scale. Even if the fibers are represented indirectly, the constitutive law contains information about their behavior during loading. Experimental data on a single fiber pullout (Yang et al., 2008a; Scheffler

et al., 2013; Redon et al., 2001) as well as on whole specimens made of fiber reinforced composite (Li et al., 2001; Zhou et al., 2010) are broadly reported in literature, however, the connection between them is missing. For example the correlation between concrete strength on one side and bond and frictional fiber characteristics on the other side would be extremely helpful.

The numerical model is able to represent the fiber reinforced composites behavior, strain-hardening after the initial cracking and also multiple cracks are captured. However, the parameters used for the numerical model are quite different compared to those reported experimentally.

Part III

Dynamics

7 STRAIN-RATE EFFECT IN CONCRETE FRACTURE

Macroscopic mechanical behavior of concrete is dependent on the strain rate. Damaging specimens under higher strain rate typically leads to increase of the loading forces and energy dissipation. In case of quasi-static loading, the initial micro cracks localize into one highly damaged zone – macro crack. For higher rates, the work done by loading forces is not consumed by one crack only, but dissipates via multiple cracking and crack branching (Jirásek and Bažant, 1995). For processes that are slow, but not slow enough to be considered as quasi static, the increase in loading forces is attributed to viscous effects and can possibly be captured by strain rate dependent material properties, for high loading rates the influence of inertia forces is the main factor responsible for increase in strength and crack branching. For high strain rates, fragmentation of the material occurs. With increasing strain rate, the amount of very small fragments increases (Fowler and Scheu, 2016). The model needs to take these small fragments into account either by modeling them directly or representing them in constitutive law phenomenologically. Direct modeling of such small particles enables more detailed description of material behavior, but it is computationally demanding when modeling structures of reasonable dimensions. With the strain rate dependent constitutive relation that accounts for small fragments phenomenologically, the computational cost can be significantly reduced.

Such a phenomenological description can be easily provided by dynamic increase factor (DIF). With help of DIF, the material properties are usually set to fit large series of experimental results. Several examples of such approach can be found in literature (Eibl and Schmidt-Hurtienne, 1999; Leppänen, 2006).

The eurocode (CEB, 1990) accounts for the difference between quasi-static tensile strength f_t and the dynamical strength $f_{t,imp}$ using the dynamic increase factor (DIF) for strain rates in two ranges, lower and higher with the boundary strain rate value of 30 s^{-1} . Malvar and Crawford (1998) reported that the progressive increase occurs already for strain rates around 1 s^{-1} and the following modification was proposed.

$$f_{t,imp}/f_t = \begin{cases} (\dot{\epsilon}_t/\dot{\epsilon}_{t0})^{\delta_s} & \text{for } \dot{\epsilon}_t \leq 1 \text{ s}^{-1} \\ \beta_s(\dot{\epsilon}_t/\dot{\epsilon}_{t0})^{1/3} & \text{for } \dot{\epsilon}_t > 1 \text{ s}^{-1} \end{cases} \quad (7.1)$$

where $\dot{\varepsilon}_t$ is tensile strain rate and other constants are calculated according to

$$\begin{aligned}\delta_s &= \frac{1}{1 + 8 f_{cm} / f_{cm0}} \\ \log \beta_s &= 6\delta_s - 2 \\ \dot{\varepsilon}_{t0} &= 10^{-6} \text{ s}^{-1} \\ f_{cm0} &= 10 \text{ MPa}\end{aligned}$$

and f_{cm} is static compressive strength of concrete. Malvar and Crawford (1998) claim that this formula is applicable up to strain rate 160 s^{-1} .

It is not only the strength itself that changes with high strain rate. For quasi-brittle materials like concrete, fracture energy is an important material parameter. The eurocode (CEB, 1990) states that the data regarding the strain rate effect on fracture energy are too incomplete to include it into model code, nevertheless, the existence of its dependency is mentioned there. Experimental data concerning also dynamic fracture energy were published e.g. by Weerheijm and Doormaal (2007) or Schuler and Hansson (2006).

However, direct multiplication of material strength (or fracture energy) by DIF demands the constant strain rate during the investigated time period. It is therefore suitable for rough estimation of material dynamic strength only.

For more detailed analysis, dynamic solution accounting for inertia forces is more suitable. Solution of material dynamic behavior with discrete meso-scale model is described in the following sections.

8 TRANSIENT SOLUTION

Simulations of material behavior under various strain-rates bring necessity of dynamic solution that consider inertia and damping forces.

8.1 Balance equation - time integration

The calculations are performed in dynamic regime, the time dependent response is obtained from the solution of equations of motion

$$\mathbf{M}\ddot{\mathbf{u}} + \mathbf{C}\dot{\mathbf{u}} + \mathbf{K}\mathbf{u} = \mathbf{F} \quad (8.1)$$

where \mathbf{M} , \mathbf{C} and \mathbf{K} stand for mass, damping and stiffness matrix respectively, \mathbf{F} is a loading vector and \mathbf{u} is vector of unknown displacements and rotations, dotted symbols represent first and second time derivative – accelerations and velocities respectively.

Equations of motion are solved using an implicit time integration scheme according to Newmark (1959). In this case, time-derivatives of accelerations and velocities are approximated

$$\ddot{\mathbf{u}}_{t+\Delta t} = \frac{1}{\beta\Delta t^2} (\mathbf{u}_{t+\Delta t} - \mathbf{u}_t) - \frac{1}{\beta\Delta t} \dot{\mathbf{u}}_t - \left(\frac{1}{2\beta} - 1\right) \ddot{\mathbf{u}}_t \quad (8.2)$$

$$\dot{\mathbf{u}}_{t+\Delta t} = \dot{\mathbf{u}}_t + \Delta t (1 - \gamma) \ddot{\mathbf{u}}_t + \gamma\Delta t \ddot{\mathbf{u}}_{t+\Delta t} \quad (8.3)$$

Substituting Eqs. (8.2)-(8.3) into (8.1), the following system is obtained (Bathe, 1996)

$$\left(\mathbf{K} + \frac{1}{\beta\Delta t^2}\mathbf{M} + \frac{\gamma}{\beta\Delta t}\mathbf{C}\right)\mathbf{u}_{t+\Delta t} = \mathbf{F}_{t+\Delta t} + \mathbf{M}\left(\frac{1}{\beta\Delta t^2}\mathbf{u}_t + \frac{1}{\beta\Delta t}\dot{\mathbf{u}}_t + \left(\frac{1}{2\beta} - 1\right)\ddot{\mathbf{u}}_t\right) + \mathbf{C}\left(\frac{\gamma}{\beta\Delta t}\mathbf{u}_t + \left(\frac{\gamma}{\beta} - 1\right)\dot{\mathbf{u}}_t + \frac{\Delta t}{2}\left(\frac{\gamma}{\beta} - 2\right)\ddot{\mathbf{u}}_t\right) \quad (8.4)$$

where on the left side, the part multiplied by unknown displacements $\mathbf{u}_{t+\Delta t}$ is the effective stiffness and the right-hand side is the effective loading vector. Δt is time step length and β and γ are parameters of Newmark method, that should be kept within the following limits to get unconditionally stable solution

$$2\beta \geq \gamma \geq 0.5 \quad (8.5)$$

The system is in nonlinear regime damped by dissipation of energy. Such effect is considerably more important than damping due to viscous effect and friction that

are collected in matrix \mathbf{C} . Therefore damping by matrix \mathbf{C} is omitted hereinafter.

8.2 Mass matrix

Lumped mass matrix is commonly used in dynamic simulations. Such simplification neglects the influence of the moments of inertia and takes into account only the mass of particle concentrated in its center. However, neglecting the inertia moments might provide inaccurate solution. Furthermore, the Voronoi node does not have to coincide with Voronoi cell center of gravity. The full matrix is therefore used here.

Symmetric mass matrix of a single particle then consists of 6×6 values corresponding to 3 translational and 3 rotational DOFs as follows

$$\mathbf{M} = \left[\begin{array}{ccc|ccc} m & & & \text{additional} & & \\ & m & & \text{momentum} & & \\ & & m & \mathbf{S}_m & & \\ \hline & s & & \text{inertia} & & \\ & & y & \text{tensor} & & \\ & & & \mathbf{E}_Q & & \end{array} \right] \quad (8.6)$$

where m stays for particle mass $m = \rho V$. Since the mass matrix is based on the geometry of rigid particles and the fracture is allowed only on their contacts, the matrix itself is considered constant during the whole solution time. Description of sub-matrices called additional momentum \mathbf{S}_m and inertia tensor \mathbf{E}_Q is in following subsections 8.2.1 and 8.2.2.

8.2.1 Additional momentum

Translation and rotational DOFs are related to the node of Voronoi cell. That node, in general, does not coincide with particle center of gravity. Inertia of particle mass relative to Voronoi node brings to the system additional momentum that is taken into account by sub-matrix \mathbf{S}_m

$$\mathbf{S}_m = m \begin{bmatrix} 0 & \Delta z & -\Delta y \\ -\Delta z & 0 & \Delta x \\ \Delta y & -\Delta x & 0 \end{bmatrix} \quad (8.7)$$

where Δx , Δy and Δz describes positional shift between particle gravity center and Voronoi node in terms of coordinates x , y and z .

8.2.2 Inertia tensor

The matrix representing inertia tensor consists of moments and products of inertia

$$\mathbf{E}_Q = \begin{bmatrix} I_{xx} & -I_{xy} & -I_{xz} \\ -I_{xy} & I_{yy} & -I_{yz} \\ -I_{xz} & -I_{yz} & I_{zz} \end{bmatrix} \quad (8.8)$$

Moments and products of inertia are obtained from integration over the volume domain, in our case, over volume of the particle.

$$I_{xx} = \int_V \rho(y^2 + z^2) dV \quad (8.9)$$

$$I_{yz} = \int_V \rho yz dV \quad (8.10)$$

The rigid bodies obtained from the Voronoi tessellation are convex polyhedrons. To calculate the inertia moments, these polyhedrons are decomposed into simplexes (tetrahedrons) for which analytical formula for inertia tensor exists (Tonon, 2005). One can calculate moment of inertia for a single tetrahedron (relative to its centroid) from its vertex coordinates. For example, equation for I_{xx} reads

$$I_{xx} = \rho V (y_1^2 + y_1y_2 + y_2^2 + y_1y_3 + y_2y_3 + y_3^2 + y_1y_4 + y_2y_4 + y_3y_4 + y_4^2 + z_1^2 + z_1z_2 + z_2^2 + z_1z_3 + z_2z_3 + z_3^2 + z_1z_4 + z_2z_4 + z_3z_4 + z_4^2) / 10 \quad (8.11)$$

Similarly, product of inertia I_{yz} can be obtained

$$I_{yz} = \rho V (2y_1z_1 + y_2z_1 + y_3z_1 + y_4z_1 + y_1z_2 + 2y_2z_2 + y_3z_2 + y_4z_2 + y_1z_3 + y_2z_3 + 2y_3z_3 + y_4z_3 + y_1z_4 + y_2z_4 + y_3z_4 + 2y_4z_4) / 20 \quad (8.12)$$

Here, subscripts 1–4 refer to four tetrahedron vertices. Expressions for moments and products of inertia related to other two base axes are analogical.

The tensors obtained from Eqs.(8.11)-(8.12) need to be further transformed to Voronoi cell node. This is achieved using the Steiner's (parallel axis) theorem.

8.3 Elastic behavior in dynamic regime

In this section, elastic response of the model is compared with analytical solution. The elastic behavior of the model is tested using a cantilever beam loaded by a force

$F = 1$ N at the free end (Fig. 8.1). Its dimensions are following: length L is 200 mm, depth and width are 20 mm. Particle radii, parameters of the Newmark method and the time step length are varying in order to investigate the influence of their change to the model behavior. For comparison, one (reference) setting is kept in all studies the same: $l_{\min} = 2$ mm, time step 0.05 ms and parameters $\beta = 0.25$ and $\gamma = 0.5$.

Simplifying the cantilever as an ideal Euler-Bernoulli beam and assuming that it is vibrating in its first natural shape only, the deflection of the free end can be calculated analytically. The solution is

$$u(t) = \frac{FL^3}{3EI}(\cos(\omega_I t) - 1) \quad (8.13)$$

where F stands for loading force at the free end, L for length of the beam, E is the elastic modulus and I is the moment of inertia of the beam cross section. The first natural frequency ω_I can be expressed

$$\omega_t = \lambda_I \sqrt{\frac{EI}{mL^3}} \quad (8.14)$$

where λ_I is according to Brepta et al. (1994) equal to 1.875. In all the graphs on the following pages, this analytical solution is plotted in gray while static solution appears as thin straight line. The response of the model is shown in Figs. 8.2-8.4. In each figure, the upper graph displays evolution of deflection of the free end in time, and the lower graph the time dependence of the vertical reaction in the support. Each figure shows the sensitivity of the model to the change of one input parameter. The elastic parameters of the meso-scale model used here are $E_0 = 48$ GPa and $\alpha = 0.29$.

At first the solution with different length of the time step was examined (Fig. 8.2). Time step length is $\Delta t \in \{0.005, 0.05, 0.5\}$ ms. On the lower graph, we can observe

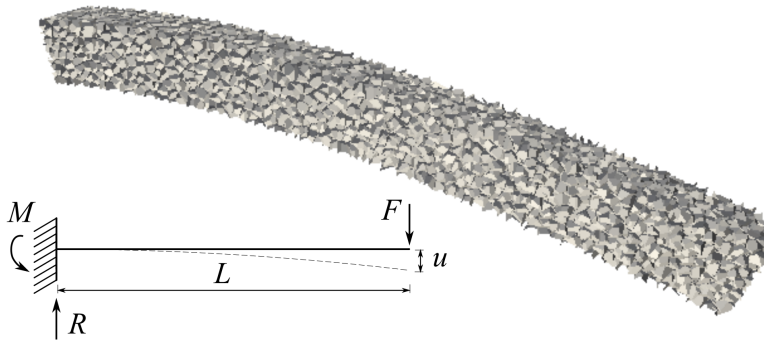


Fig. 8.1: Modeled geometry and deformed shape showing the discrete structure with 100 times magnified deformation.

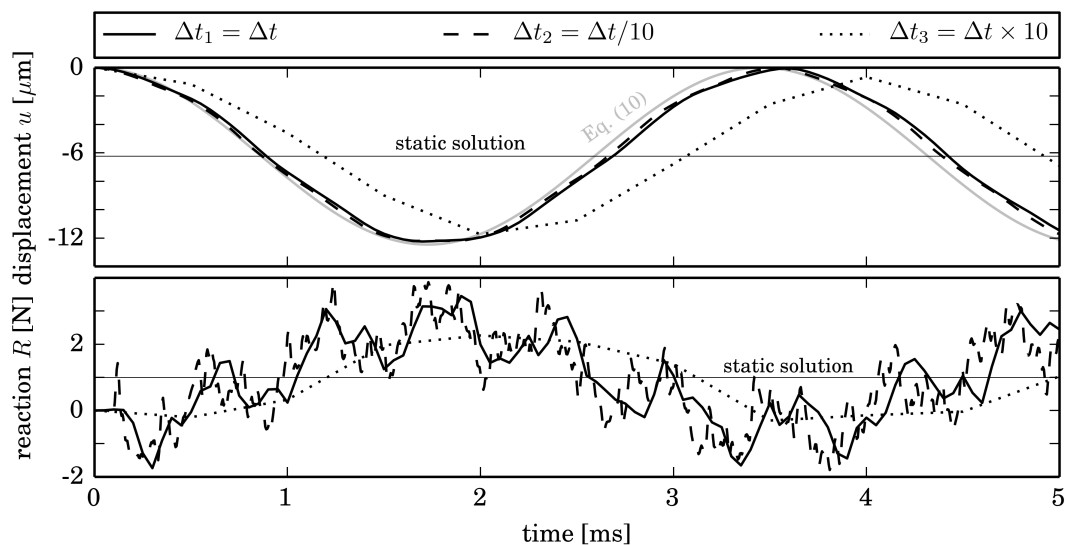


Fig. 8.2: Dynamic response of cantilever beam using various time discretizations.

that the longer the time step, the more high frequencies are damped as a side effect of numerical solution. The difference between the two finer time discretizations is quite small compared to the difference between any of them and the longest time step. high frequency oscillations in reaction R are caused by the fact that for the shorter time step length, the initial “impact” of the constant force happens in shorter time. To damp high order modes it is recommended to use Newmark constants that satisfy (Bathe, 1996)

$$\beta \geq 0.25(0.5 + \gamma)^2 \quad (8.15)$$

Fig. 8.3 shows the dependence of the model behavior on change of the parameters of the Newmark method, beam is loaded by the same constant force. It can be seen, that if we use the parameters for the trapezoidal rule ($\beta = 0.25$ and $\gamma = 0.5$), we are taking into account more high order modes than if we use higher values of these parameters, for which, the response becomes smoother.

Since the model is based on a concept of rigid body motion of particles of finite size, it is important to understand the influence of their size. In all previous simulations, particle size is 2 mm, which gives us approximately 10 bodies per cross section depth/width. In Fig. 8.4, the change of response with the change of the particle size is shown. The difference is obvious particularly for size 6.67 mm. In this case, only 3 particles are filling the depth/width of the beam.

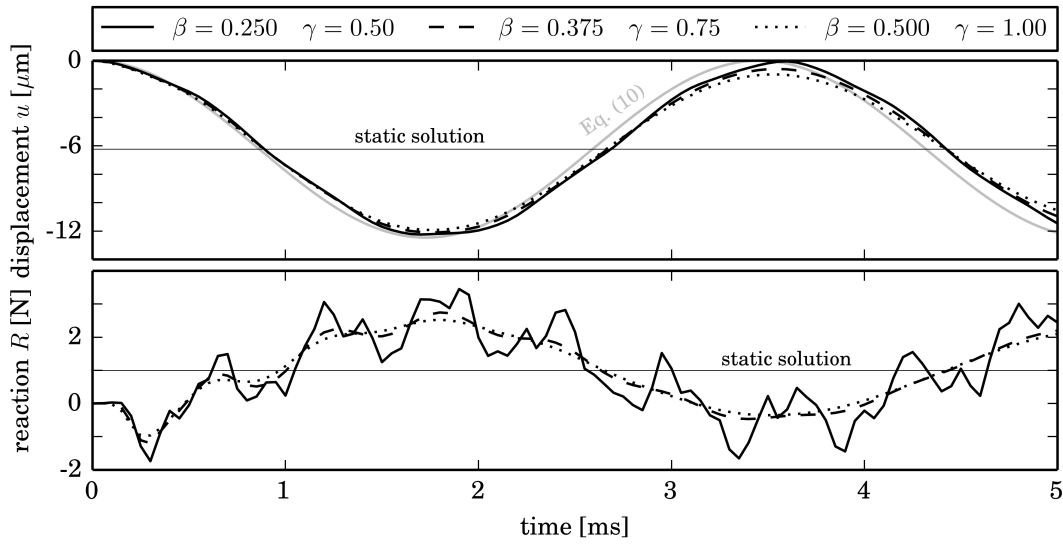


Fig. 8.3: Dynamic response of cantilever beam using various parameters of Newmark method.

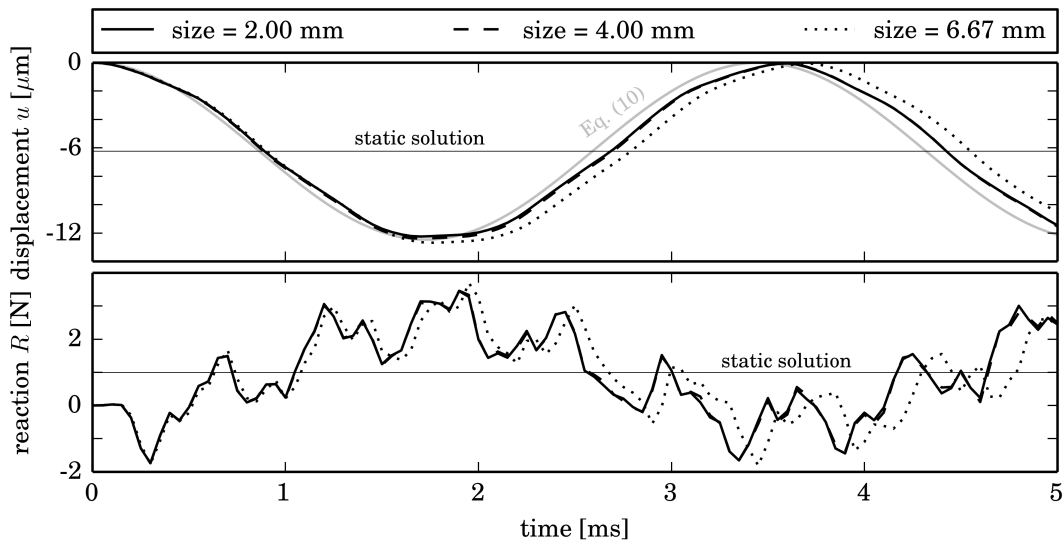


Fig. 8.4: Dynamic response of a cantilever beam using different particle sizes.

8.4 Strain rate dependency of constitutive law

The discrete model is able to capture some part of strain rate dependency at macroscopic level by correctly accounting for heterogeneity and inertia in the meso-structure. However, since used resolution does not capture all the possible cracking in the material undergoing fast damage and also viscous effect of free water in the material are not explicitly addressed, some strain rate dependency needs to be incorporated phenomenologically. To account for inertia of the interparticle material

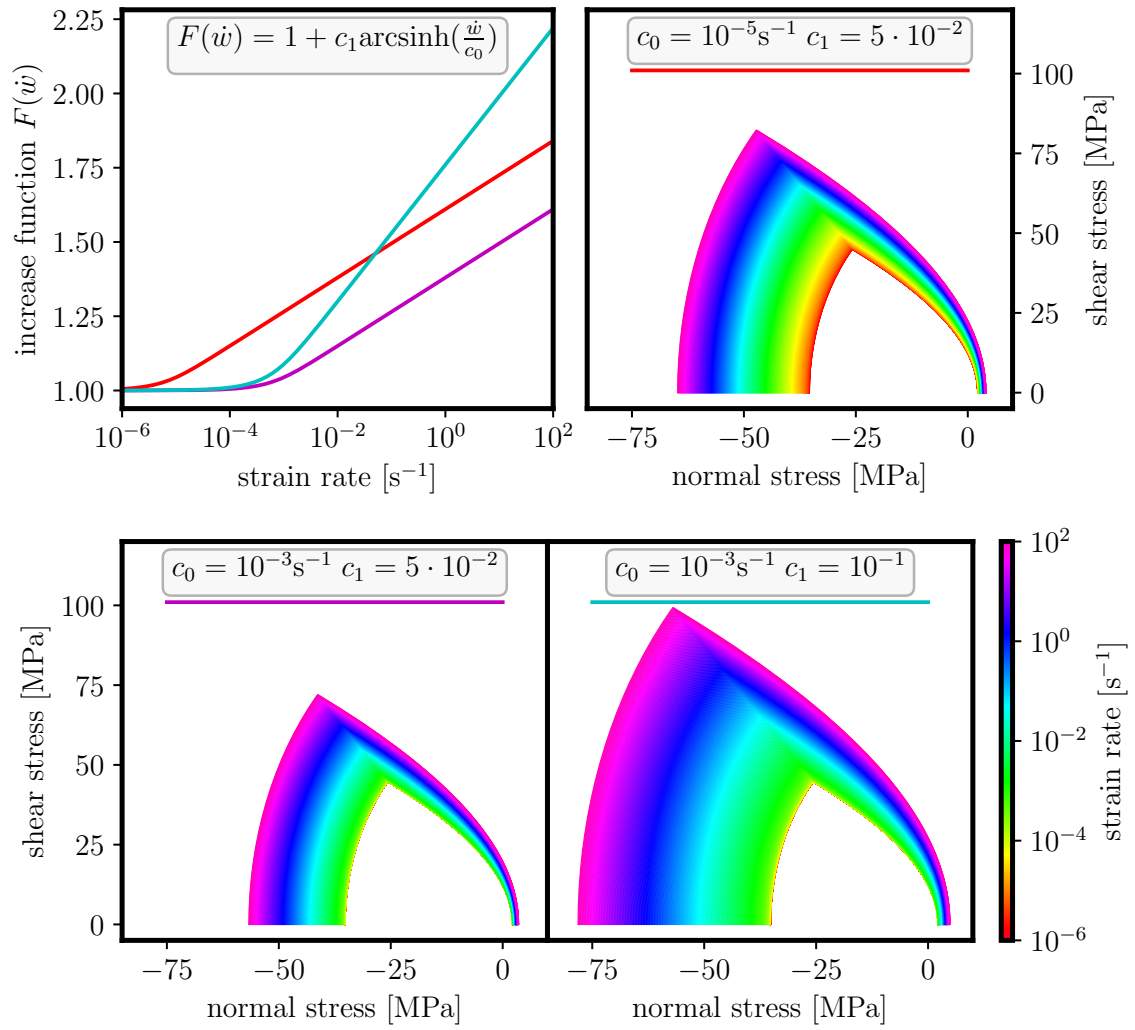


Fig. 8.5: Influence of parameters on increase function and scaling the elastic envelope for increasing strain rate.

in inelastic regime, the constitutive behavior of contact facets is enriched by dependency on difference in velocities of particles it connects. Calculation of s_{eq} takes into account rate of crack opening, \dot{w} , of contact element through increase function $F(\dot{w})$ provided Cusatis (2011).

$$s_{\text{eq}} = F(\dot{w})f_{\text{eq}} \exp\left(\frac{K}{f_{\text{eq}}}\left\langle e_{\text{eq}} - \frac{F(\dot{w})f_{\text{eq}}}{E_0} \right\rangle\right) \quad (8.16)$$

$$F(\dot{w}) = 1 + c_1 \operatorname{arcsinh}\left(\frac{\dot{w}}{c_0}\right) \quad (8.17)$$

where variables c_0 and c_1 are additional material parameters.

The influence of parameters c_0 and c_1 is depicted in left part of Fig. 8.5, c_0 is

responsible for length of initial rate-independent part and c_1 for increase of slope of the second, rate-dependent part. The left part of the figure shows the elastic limit f_{eq} for different straining direction; the elastic envelope is scaled according to the strain rate. Initial slope of the softening curve remains unchanged, therefore more energy is dissipated. This accounts for less localized strain in material loaded by high strain rate compared to quasi-static fracture.

8.4.1 Numerical study of strain rate effect

The model was applied to simulate a simple tensile test of a prismatic beam in uniaxial tension. The beam width and depth is 100 mm, thickness 40 mm. One end of the beam is fixed, whereas the other one is loaded by an increasing deformation, under wide range of strain rates, from 10^{-6} to 10^2 s $^{-1}$.

Various settings of an increase function from Eq. (8.17) used are listed in Tab. 8.1. Other material parameters used in calculations have the following values: elastic modulus $E_0 = 50$ GPa, tangential/normal stiffness ratio $\alpha = 0.25$, tensile strength $f_t = 2.5$ MPa, meso-scale fracture energy $G_f = 25$ N/m 2 . Inertia is governed by the material density, $\rho = 2500$ kg/m 3 .

	c_0 [s $^{-1}$]	c_1 [-]
set 1	$1 \cdot 10^{-5}$	$5 \cdot 10^{-2}$
set 2	$2.5 \cdot 10^{-5}$	$8 \cdot 10^{-5}$
set 3	$1 \cdot 10^{-2}$	$8 \cdot 10^{-5}$
set 4	$1 \cdot 10^{-5}$	$5 \cdot 10^{-1}$

Tab. 8.1: Parameters of strain rate dependency for various settings of constitutive law used in calculations.

Results are plotted in Fig. 8.6. Dynamic increase factor (DIF) for any model response is calculated as ratio between dynamic and static strength f_{dyn}/f_{stat} . Static strength f_{stat} is taken from simulation under strain rate $\dot{\epsilon}_{stat} = 10^{-6}$ s $^{-1}$. Reference calculation is performed using *basic* constitutive law with $F(\dot{w}) = 1$.

The response of the model is compared to experimental results (Yan and Lin, 2006; Wu et al., 2005; Brara and Klepaczko, 2006a), which are also shown in Fig. 8.6 together with dotted curve representing the modified CEB relation for DIF presented in (Malvar and Crawford, 1998).

It can be observed that setting of strain rate dependency of constitutive law changes overall response, however, it should be noted that sudden increase in DIF for rates $\dot{\epsilon} \geq 1$ s $^{-1}$ is also due to inertia forces.

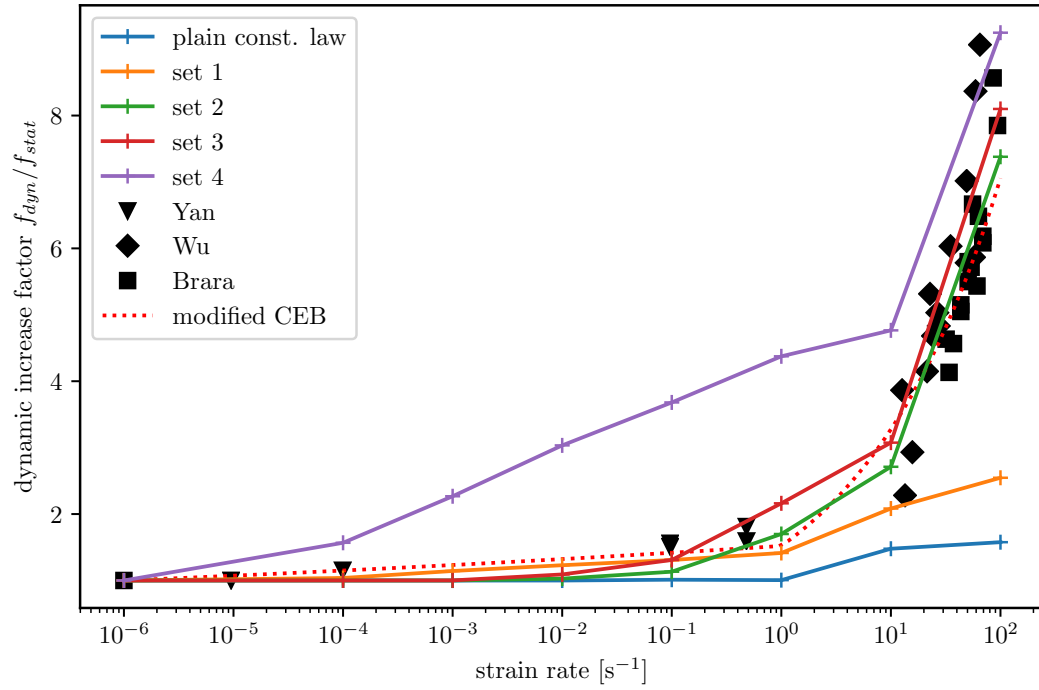


Fig. 8.6: Increase in tensile strength for various settings of the model compared with experimental data (Yan and Lin, 2006; Wu et al., 2005; Brara and Klepaczko, 2006a) and modified CEB formulation (Malvar and Crawford, 1998).

9 NUMERICAL SIMULATIONS

9.1 Available experimental data

Experimental data regarding increase in compressive strength are quite abundantly reported in literature already since the half of 20th century, e.g. (Mellinger and Birkimer, 1966). On the other hand, data qualifying tensile properties of concrete under different strain-rates, especially when concerning more information than simply dynamic tensile strength, are quite limited.

Very little experiments using conventional techniques for testing of concrete tensile properties are published. As an example, experiments on concrete L-shape specimens or compact tension tests can be found (Ožbolt et al., 2016). These test are performed in dynamic regime under relatively low loading rates, up to 2.4 m/s and simulated here with the discrete meso-scale model.

More convenient technique for estimation of high-rate tensile strength was reported by Gran et al. (1985) where long concrete bar was loaded in compression along the bar length, as well as in radial direction. The compressive force applied in longitudinal bar direction was released suddenly by an explosive (decrease from pre-stressing force to zero happened during period of 30 μ s) and as the relaxing wave approached from both sides, it meets in the middle where tensile failure occurs.

Another technique using Hopkinson Pressure Bar setup (Brara and Klepaczko, 2006b) is based on imposing pressure on a concrete bar that finally breaks in tension after the compressive wave is reflected at the rear face as a tensile stress wave. Several techniques for estimation of dynamic tensile strength from this spalling test are reported in literature, e.g. using a distance where the failure occurs or various techniques based on observation of the specimen velocity field. Simulations of spalling test by homogeneous discrete model with rate dependency due to viscous material model are reported in (Hwang et al., 2016). Erzar and Forquin (2011) published large set of spalling experiments is published in , including velocity of the rear face of the specimen. These experimental data are chosen for comparison with the presented meso-scale discrete model.

The following sections present simulations of the experiments from literature with the numerical discrete model. Also several studies are presented. Material parameters are different for each experiment, since the model is applied on experimental data performed on different materials. The only constants in all further calculations are Newmark's parameters $\beta = 0.3$ and $\gamma = 0.55$ chosen according to Bathe and Noh (2012).

9.2 L-shaped specimen

In this section, simulations of the experimental series of concrete specimens with a shape of an upside down letter L (Ožbolt et al., 2015) are presented.

9.2.1 Geometry and material properties

Specimen dimensions are $W, D = 500$ mm and $W_1, D_1 = 250$ mm (Fig. 9.1). Specimen thickness is $t = 50$ mm. Depth of the bottom support is 100 mm and loading is applied by prescribed displacement in a distance of 30 mm from the edge of the specimen. The loading is applied via rigid plate that can freely rotate. The loading force is calculated during the simulations. Loading rates are chosen according to Ožbolt et al. (2015) as 0.25 mm/s for quasi-static loading and 0.1, 0.35, 0.74, 1.0 and 2.4 m/s to study influence of the strain-rate.

Material parameters are also taken from Ožbolt et al. (2015). Macroscopic Young's modulus is $E = 32.2$ GPa and Poisson's ratio is $\nu = 0.18$; the elastic mesoscopic parameters at the interparticle contacts are obtained from Eq. (3.8): meso-scale elastic modulus $E_0 = 50$ GPa and normal-tangential stiffness ratio $\alpha = 0.237$, respectively. Further material properties taken from Ožbolt et al. (2015) are: material density $\rho = 2210$ kg/m³ and tensile strength $f_t = 3.12$ MPa. The meso-scopic

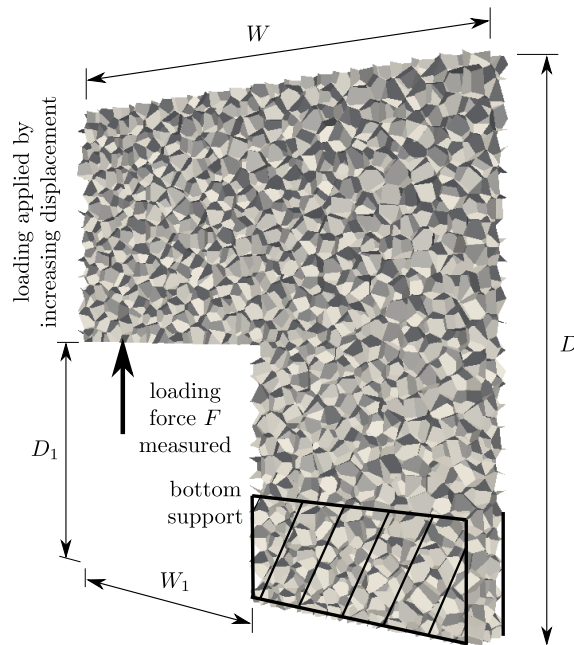


Fig. 9.1: Geometry of simulated L-shaped specimen showing particle model structure.

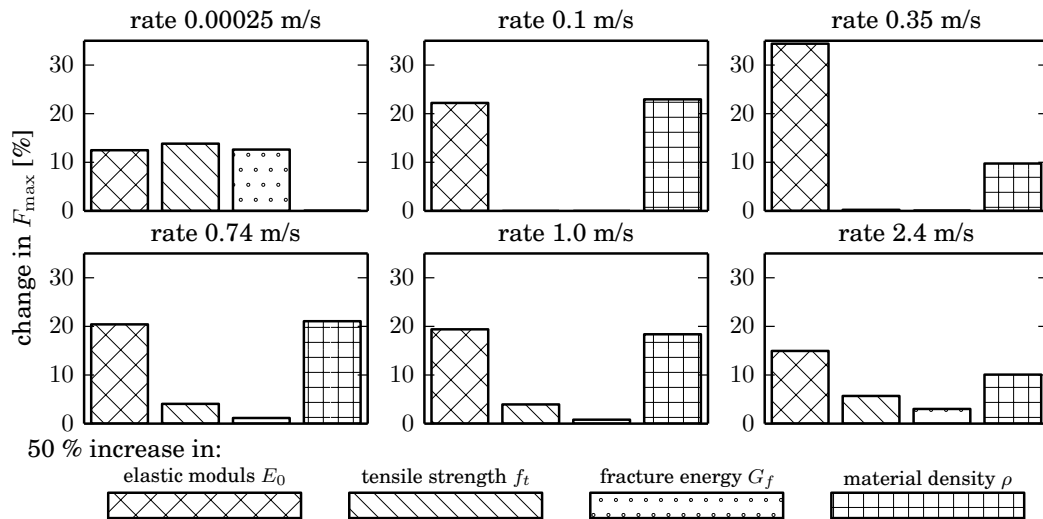


Fig. 9.2: Effect of selected material properties on the maximum loading force at various displacement rates.

fracture energy for tensile failure was identified from the quasi-static loading rate according to the experiments as $G_f = 35.5 \text{ N/m}^2$.

9.2.2 Influence of material parameters

For static loading, the influence of fracture material characteristics – f_t and G_f – plays a crucial role. The maximum loading force is mainly influenced by the tensile strength f_t and the descending part of load – displacement (time) diagram is affected by the value of fracture energy G_f . With increasing loading rate, the major influence moves towards inertia.

To demonstrate this trend, influence of selected material properties was studied, namely elastic modulus E_0 , tensile strength f_t , fracture energy G_f and material density ρ . Simulations with the mentioned parameters magnified 1.5 times were calculated. The change of maximum load is shown in Fig. 9.2. It can be observed, that the greatest increase in loading forces is caused by increase in elastic modulus E_0 for all displacement rates. The influence of tensile strength f_t and fracture energy G_f diminish with increasing loading rate, while the influence of material density ρ appears. Effect of fracture parameters can be observed again even for higher rates starting at 0.74 m/s, which is caused by cracking in the area of applied load which was not observed in experiments (Ožbolt et al., 2015).

To show this effect of strength and fracture energy in detail, these are scaled similarly to application of spatial material randomness (Sec. 3.4), $h(\mathbf{x}) = m$, where m is a strength multiplier. From load displacement curves in Fig. 9.3, one can observe

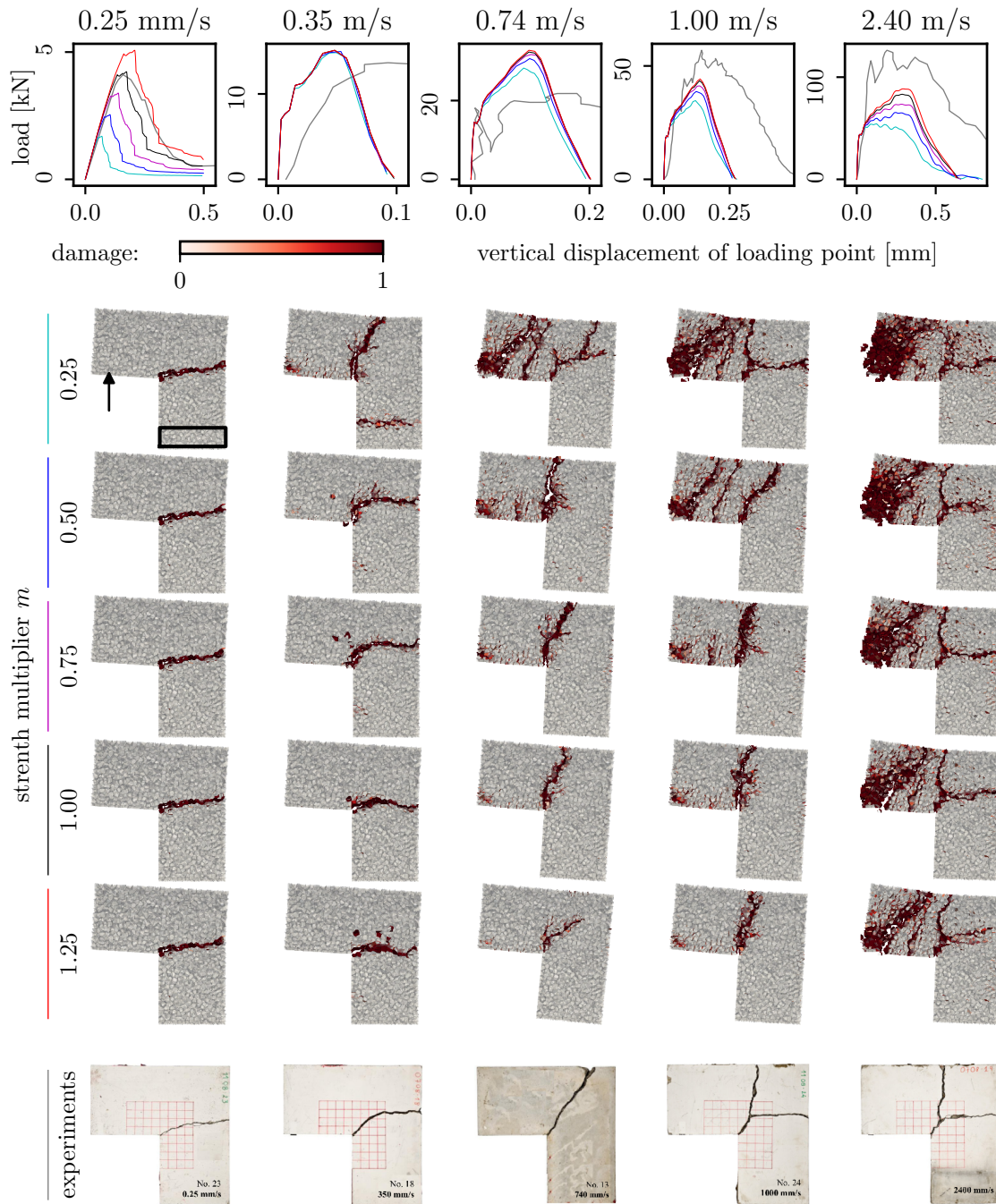


Fig. 9.3: Load–displacement curves and crack patterns for different material strength used in numerical simulations compared with experimental data reported by Özbolt et al. (2015).

that the value of the peak load for quasi-static rates is largely influenced, whereas the effect for other loading rates is substantially lower, especially for loading velocity 0.35 m/s. For higher rate, the dependency is caused by crushing at the loading area. In the same figure, the crack patterns are plotted at the end of each simulation.

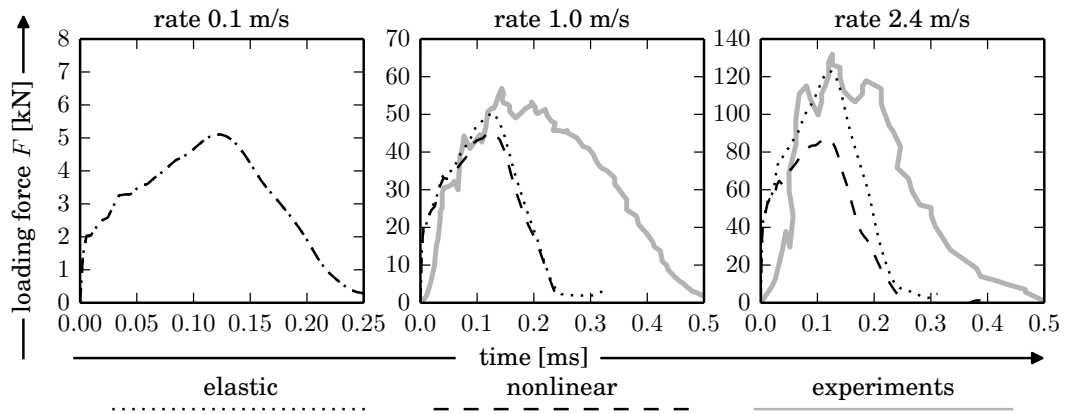


Fig. 9.4: Comparison of nonlinear vs. elastic response of the model.

The crack pattern changes with increasing rate. For quasi-static loading, the crack propagates in the horizontal direction. With an increasing rate, the inclination angle grows up to the vertical direction. With further increase of the loading velocity, crack branching occurs. These results correspond to experimental observations (Ožbolt et al., 2015) added in Fig.9.3 in the bottom row. Comparing crack patterns for different scaling parameter m , weaker material results in greater inclination angle of crack direction and also crack branching occurs at lower loading velocity than for stronger material.

It is interesting to compare the results with simulations considering elastic material. In Figs.9.4 and 9.5, elastic is compared with nonlinear response and experiments from Ožbolt et al. (2015). A theoretical maximum load for elastic simulations would be in infinity, but the time dependent response oscillates around the static response and the first such wave is plotted in Fig.9.5. Comparing the elastic calculation with the experimental response, it seems that material in the whole measured response is purely elastic. The cracking in the corner of the specimen happens later when the loading wave reaches the corner. For higher rates, the nonlinear model prediction of the peak load is affected by crushing of the material close to the loading point. This undesired effect was already mentioned because it is responsible for f_t and G_f effects in high rate regimes.

Trying to avoid this crushing, gradual increase in displacement rate v is applied. Loading constraint is then calculated according to

$$u_l = \begin{cases} \left(0.5t^2 + \frac{t_0}{4\pi^2} \cos(2\pi \frac{t}{t_0}) - \frac{v_l}{t_0} \right) \frac{v_l}{t_0} & t \leq t_0 \\ v_l t - v_l t_0 u_l(t_0) & t > t_0 \end{cases} \quad (9.1)$$

where u_l is applied displacement constraint at the area of loading, v_l is a specified

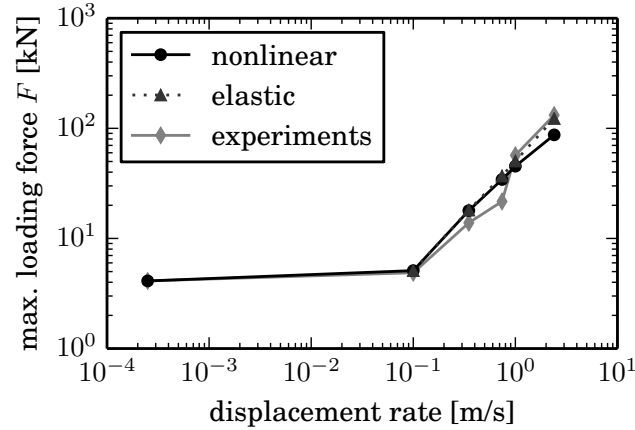


Fig. 9.5: Relation between maximum loading force and displacement rate.

loading rate and t_0 is an initial transition period (length of gradual increase of displacement rate). This analytical formula was chosen to obtain smooth transition at the beginning as well as at the end of gradual increase for all displacements, velocities and accelerations. Using this formula with different transition period t_0 , simulations of specimens loaded under displacement rate 2.4 m/s were performed. Both time dependent response and crack pattern are shown in upper part of Fig. 9.6. Using this gradual increase, the crushing in the area of applied load is reduced. On the other hand, longer initial transition period t_0 causes reduction of loading forces, because the mass is actually accelerated under lower rate.

Up to this point, particle size $l_{\min} = 15$ mm was used. Since this model uses crack band theory (Bažant and Oh, 1983), the discretization does not influence the model response for cases when the crack is localized. However, when crushing occurs and cracks are distributed in volume, the model becomes discretization dependent. The results for simulation using doubled and half particle size are shown in the lower part of Fig. 9.6. Note that for coarse discretization there are only two particles across the specimen thickness. For the finer discretization, the peak load is a bit lower and for the coarser a bit higher than for the reference particle size. But, this increase or decrease can be also attributed to the randomness of spatial discretization of the volume domain resulting in random response as mentioned in Sec. 3.1. Though that the distributed cracking occurs, the response is not influenced much by the discretization.

9.2.3 Application of rate dependent constitutive law

As has been shown in Fig. 9.3, the numerical model predicts cracking in the area of applied load, which does not occur in the experimental study, see (Ožbolt et al.,

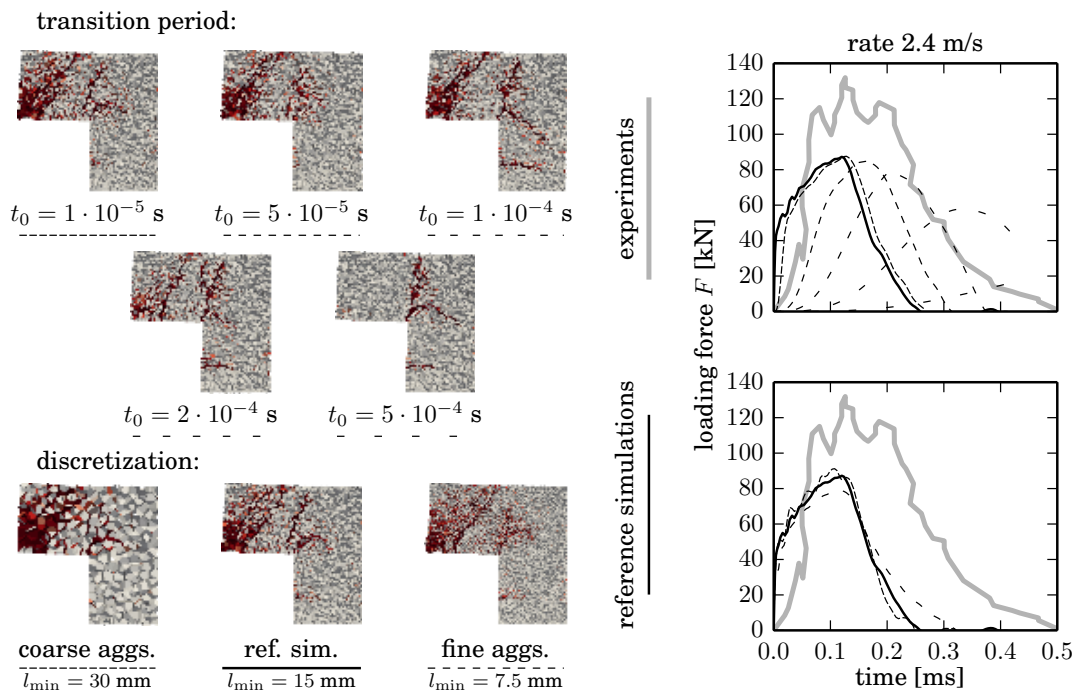


Fig. 9.6: Effect of gradual increase of displacement rate and different particle size.

2015). Furthermore the model does not sufficiently capture the increase in maximum load obtained for high strain rates measured experimentally and this is again due to distributed fracture in the loading area. This phenomenon can be attributed to missing strain-rate dependency in constitutive law, which should compensate for insufficient resolution of the model inner structure and viscous effects. The constitutive law was therefore enhanced with strain rate dependency according to Cusatis (2011), as explained in Sec. 8.4

Calculations using two different sets of parameters c_0 and c_1 are performed. The first one (set 1) has $c_0 = 1 \cdot 10^{-5} \text{ s}^{-1}$ and $c_1 = 5 \cdot 10^{-2}$, and the second one (set 2) has $c_0 = 4 \cdot 10^1 \text{ s}^{-1}$ and $c_1 = 1 \cdot 10^3$. Response of the models is shown in Fig. 9.7. The reference simulation without rate dependency is the one shown in Fig. 9.3 using $m = 1$. With increasing rate parameters, cracking in the area of the applied load diminishes, however, it also changes in the shape of damaged zone not corresponding to experimental evidence appears.

Loading force can also be influenced by steel mass between the force sensor and concrete material, which has to be accelerated as well and which also helps to distribute the loading force into the specimen. In the right bottom part of Fig. 9.7, response of the model with additional steel piston (steel part modeled by elastic finite elements with total mass 0.277 kg) is shown. Value of the maximum load increases significantly, however, arbitrary loading force can be obtained using different size of

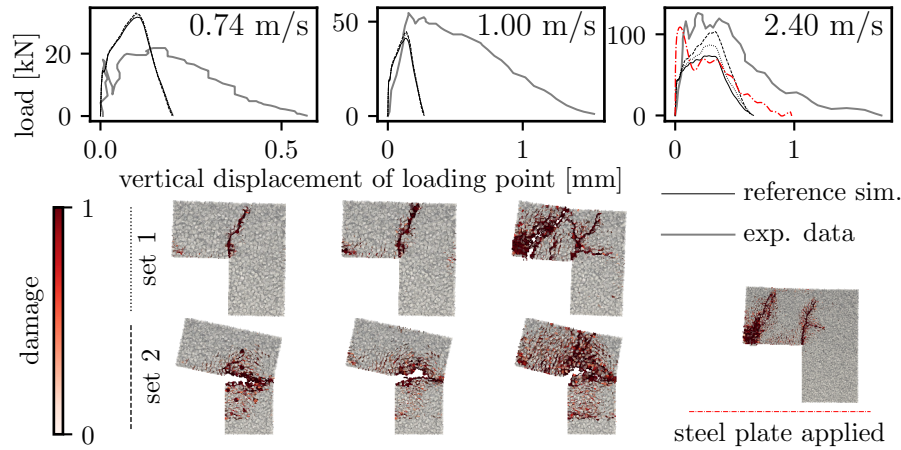


Fig. 9.7: Response of the model using strain rate dependent constitutive law and steel platen at the loading point.

this steel cylinder. Since this mass is not known to us, it is not applied for any other simulations here.

9.2.4 Application of random field

It has been shown that the change in material properties has large influence on model response for all the simulated displacement rates. Here, the focus is on faster loading rates from 0.74 to 2.4 m/s. For these loading velocities, 10 different random field realizations are applied. Correlation length $l_c = 20\text{mm}$ and standard deviation 0.25, mean fracture energy and These realizations are shown in Fig. 9.8 in the first row. Further rows show crack patterns for corresponding realization and displacement rate applied. Similarly to the change of material properties, the load-displacement response is not influenced much, but crack pattern is highly affected by presence of locally stronger or weaker material.

9.2.5 Summary

L-shaped specimens loaded by several displacement rates according to experiments by Ožbolt et al. (2015) are simulated. The peak load is highly influenced by inertia (i.e. by accelerating the mass above the loading point), while the crack pattern is highly influenced by material fracture properties. Contrary to the experimental evidence, the model predicts large zone of distributed cracking above the loading point for high loading velocities. Strain rate dependency in constitutive load helps to reduce this cracking as well as smooth loading acceleration, however, these remedies lead to incorrect crack pattern in later stages of too low loading forces.

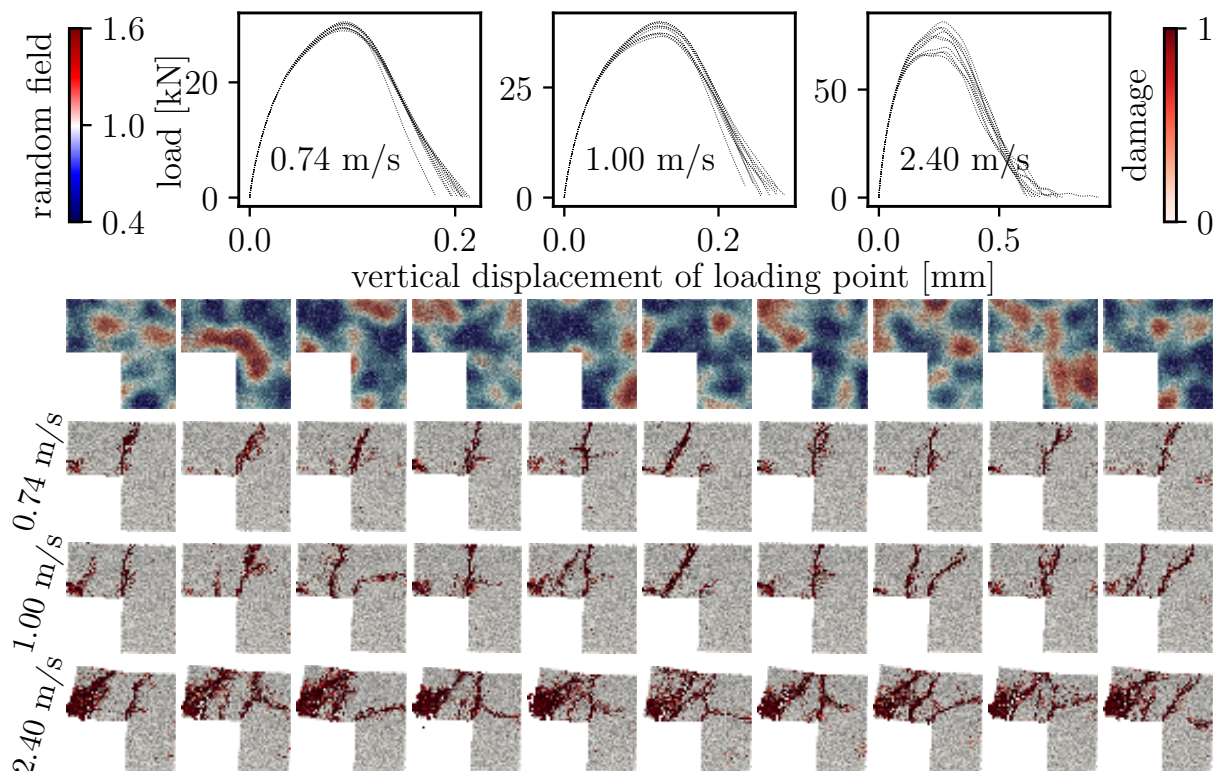


Fig. 9.8: Different response for different random field realizations applied.

9.3 Compact tension specimens

The discrete model was further applied on a recently published experimental series of notched compact tension specimens – CTS (Ožbolt et al., 2013). Also these specimens were loaded under various displacement rates.

Specimen dimensions (Fig. 9.9-left) are: width and depth $W = D = 200$ mm, notch depth $n = 64$ mm and specimen thickness is 25 mm. One side of the notch is fixed, whereas opposite side of the notch is loaded. Loading is applied in the middle of the loading area by prescribed displacement. Loaded/supported area is up to $p = 50$ mm of the notch depth. These areas are formed by rigid plates that can freely rotate around the horizontal axis pointing out of the figure plane (Fig. 9.9).

Material properties were chosen according to experiments (Ožbolt et al., 2013): elastic modulus $E_0 = 56.25$ GPa, tensile-shear stiffness ratio $\alpha = 0.237$, tensile strength $f_t = 3.5$ MPa. Fracture energy for tensile failure was set according to best fit for loading rate 0.035 m/s as $G_f = 39$ N/m². Parameter dictating the average particle size was set $l_{\min} = 7.5$ mm according to maximum aggregate size in experiments.

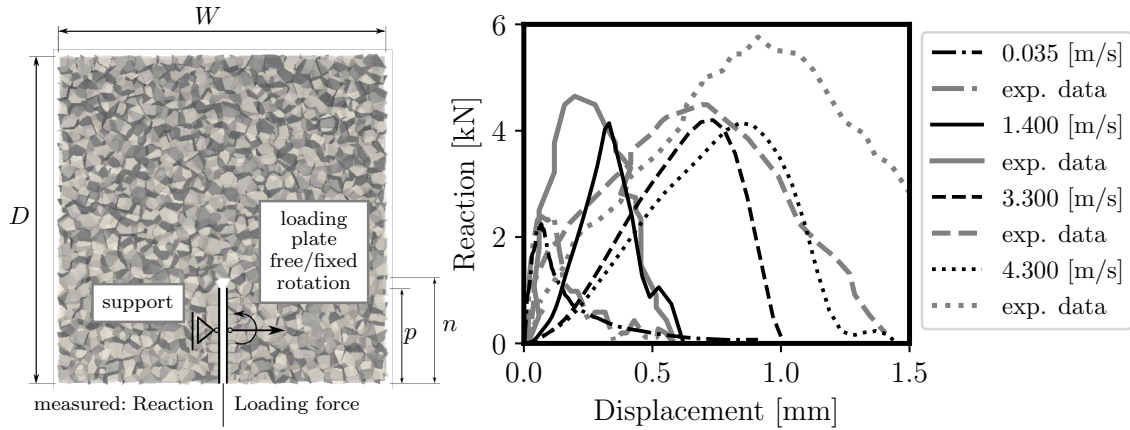


Fig. 9.9: Geometry of the specimen (left) and reaction-displacement curves for various loading rates (right).

9.3.1 Results of simulations

In the right part of Fig. 9.9, displacement of the loading point vs. reaction in fixed support is plotted and compared with the experimental curves from Ozbolt et al. (2013). Relation between the maximum reaction/loading force and applied loading rate is shown in Fig. 9.12. For this purpose, simulations under rates from 0.25 mm/s to 4.3 m/s were performed. Two sets of simulations were calculated, where rotation of loading plate was (i) allowed or (ii) restricted. Simulations with the restricted rotation provide small increase in the loading force compared to those with the free

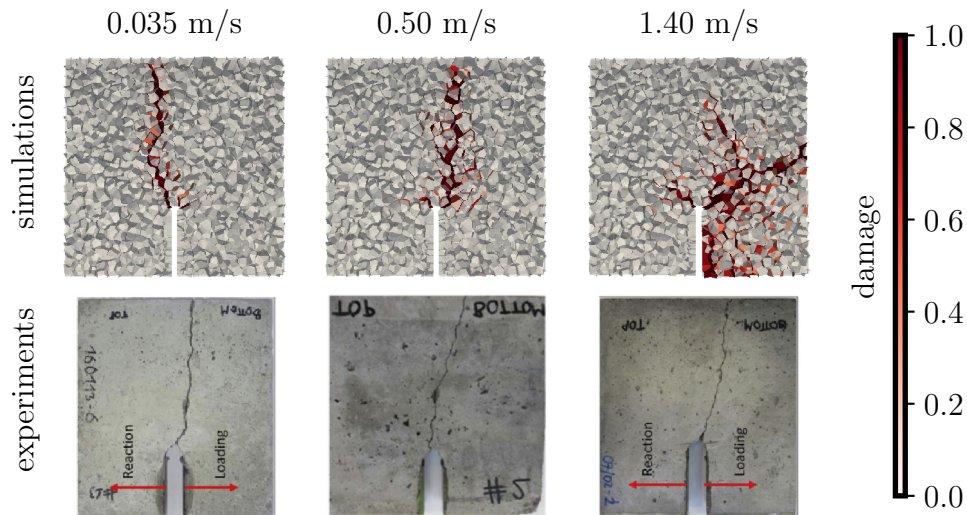


Fig. 9.10: Crack patterns obtained from numerical simulations compared with experimental data from Ozbolt et al. (2013) for lower loading rates.

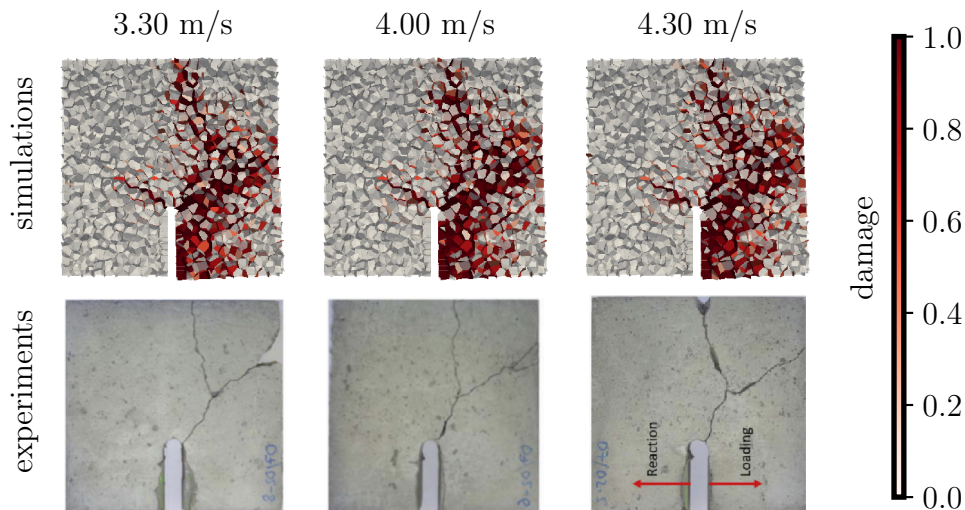


Fig. 9.11: Crack patterns obtained from numerical simulations compared with experimental data from Ožbolt et al. (2013) for higher loading rates.

rotation. In the case of max. reaction the trend is similar, but for loading rates $\geq 0.5 \text{ m/s}$, the maximum reaction decreases due to excessive crushing and changes in the crack pattern. The experimental data (Ožbolt et al., 2013) shown in left graph in Fig. 9.12 exhibit large scatter, but the trend is obvious. The simulations using rate independent constitutive law do not provide high enough reaction for higher loading rates. Using rate dependent constitutive law, higher loading forces and reactions are obtained, but for loading rates above 1 s^{-1} crushing of the material results in decrease of reaction with increasing loading rate. Change in the mechanism

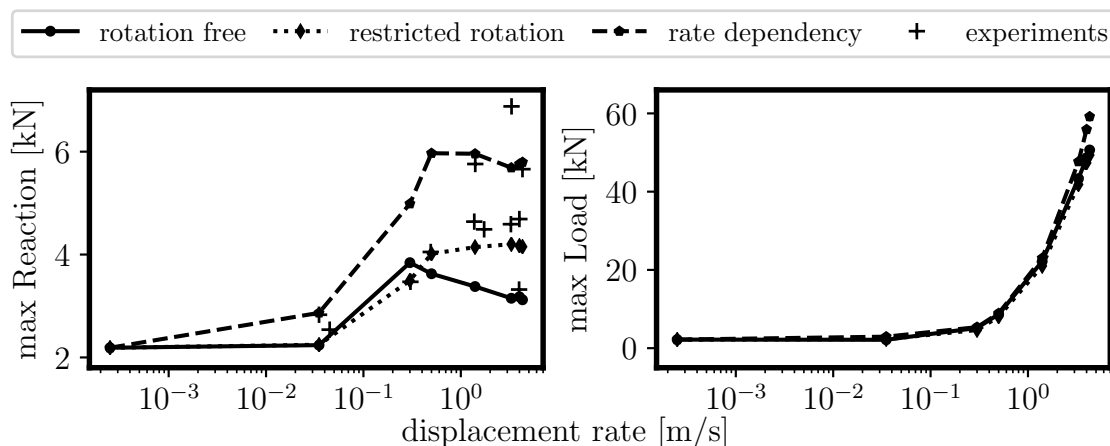


Fig. 9.12: Relation between displacement rate and the maximum reaction (left) or the maximum loading force (right).

of failure observed experimentally and simulated is shown in Figs. 9.10 and 9.11. Here, particle contacts are colored according to the value of damage parameter D . With increasing loading rate, the direction of the crack changes and crack branching occurs. For slow loading, crack propagates in the direction of the initial notch. With increasing loading rate, the crack bends towards the horizontal direction and crack branching occurs. The same trend can be seen in experiment, however, for higher loading rates, the simulation predicts crushing in the area of applied load.

9.4 Brazilian disk specimen

Simulations presented in this section were calculated using mathematical models corresponding to experimental series on Brazilian splitting tests reported by Jin et al. (2017). Simplified models of Brazilian discs were supported (respectively loaded) by line of boundary aggregates as shown in Fig. 9.13. The loading is applied by increasing deformation under prescribed loading rate. It does not fully correspond to experimental loading, which was applied by Hopkinson bar setup. Loading by pressure (force) wave would be more realistic, but in this case, the desired displacement rate can be exactly specified. The experiments as well as simulations were performed on concrete and mortar discs with diameter $D = 70$ mm and with thickness $T = 30$ (further referred to as thin) and 55 mm (further referred to as thick).

Two materials (concrete and mortar) were used in experimental study, therefore also two sets of material parameters were used for the modeling, see Tab. 9.1. Parameter l_{\min} was set according to maximum aggregate size used in experiments. The material fracture parameters were estimated with help of the maximum load obtained by quasi-static tests on thin discs. with displacement rate of $1.67 \cdot 10^{-6}$ m/s.

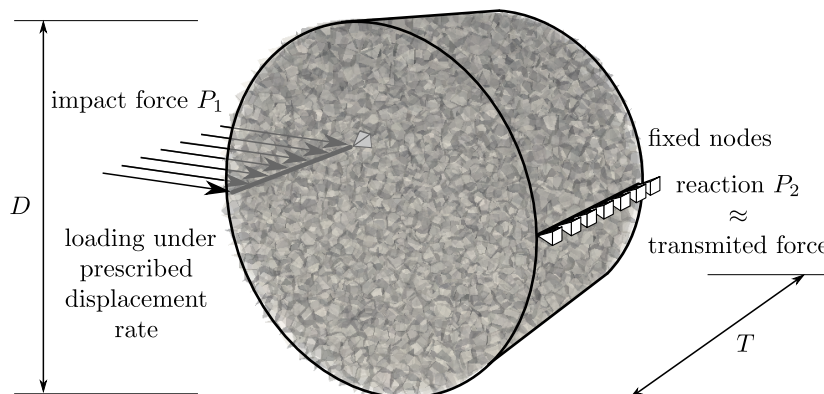


Fig. 9.13: Setup of the model representing Brazilian discs.

	E_0 [GPa]	α	f_t [MPa]	G_f [N/m ²]	ρ [kg/m ³]	l_{\min}
concrete	44	0.237	2.64	9.93	2400	7.50
mortar	40	0.237	3.47	40.66	2020	2.36

Tab. 9.1: Material parameters used from simulations of concrete and mortar discs.

Value of material meso-scale tensile strength was set to the value of macro-scopic tensile strength of the material and meso-level fracture energy was then found by fitting the model response to match the peak load only, since the post-peak behavior is hard to capture in the case of splitting test. The fit was performed separately for both simulated materials – concrete and mortar.

In this section, strain-rate is calculated as displacement rate divided by disc diameter. This is actually not correct, since the actual strain-rate varies in space. This simplification was chosen to enable comparison with the experimental data.

For Brazilian splitting tests, the material tensile strength f_{tu} is estimated according to

$$f_{tu} = \frac{P_1 + P_2}{\pi TD} \quad (9.2)$$

where P_1 and P_2 are impact and transmitted force respectively. In the case of dynamic loading, the forces from both sides are different at each time-step. But they must be equal in the case of quasi-static loading.

9.4.1 Results of simulations

After finding the best possible set of parameters to match the quasi-static response on thin specimens, the response of thick specimens was calculated. Values of the peak load and tensile strengths obtained by the model are listed in Tab.9.2 together with the experimental values. Note that rows corresponding to thin specimens are from the fitted response, while thick sample simulations are model predictions.

		experiments		simulations	
		peak [kN]	strength [MPa]	peak [kN]	strength [MPa]
concrete	thin	8.71	2.64	<i>fit</i> 8.71	2.64
	thick	15.71	2.6	15.24	2.52
mortar	thin	11.44	3.47	<i>fit</i> 11.44	3.47
	thick	20.26	3.35	23.01	3.80

Tab. 9.2: Peak load and tesile strength obtained by the model assuming quasi-static loading compared to the experiments by Jin et al. (2017)

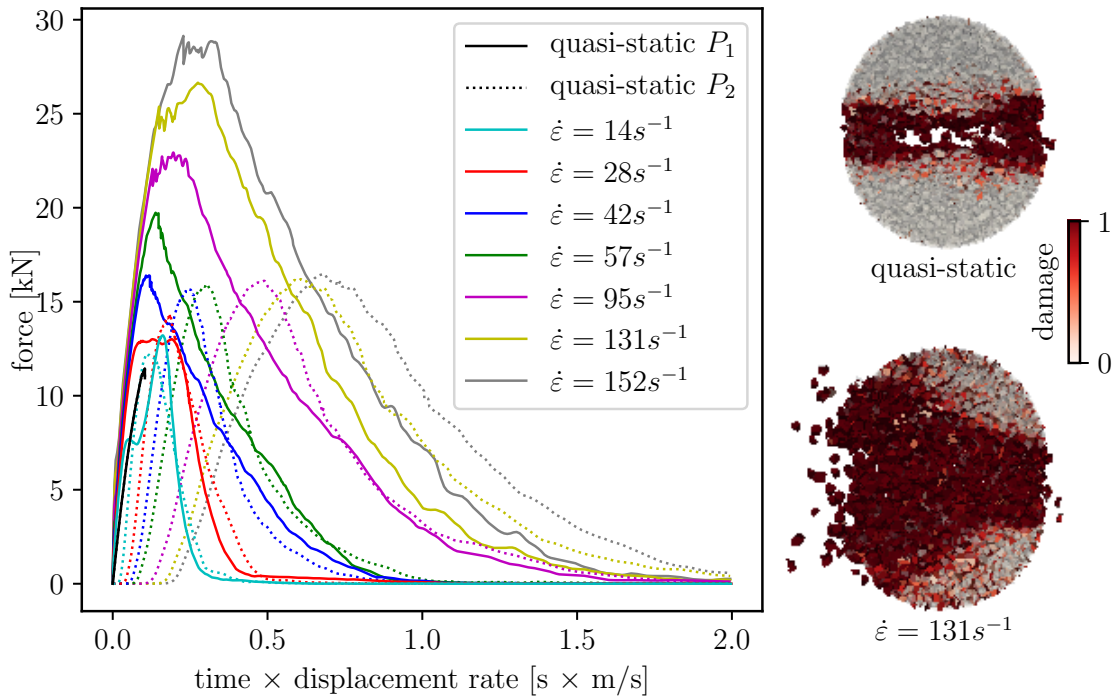


Fig. 9.14: Left: force vs. displacement curve for thin mortar specimens, right: damaged volume obtained by simulation (with magnified displacements).

The dynamical simulations were performed under wide range of displacement rates in correspondence to the experimental test. On the graph in the left part of Fig. 9.14, load-displacement curves are plotted for various strain rates. Significant delay in transmitted force can be observed as well as different increase of impact force P_1 and transmitted force P_2 . The greater increase in the first one is mainly caused by inertia.

Right part of Fig. 9.14 shows crack patterns for quasi-static and fast loading rate. In these pictures, displacements are $10\times$ magnified. Particle facets are colored according to the value of damage D . The model predicts splitting the specimen into two parts with relatively localized crack path for quasi-static loading, whereas in case of fast rate, the damage spreads into a wider zone. This corresponds to the experimental data by Jin et al. (2017)

Fig. 9.15 displays relation between the strain rate and the material dynamic tensile strength according to Eq. 9.2 obtained by the discrete particle model and experimentally by Jin et al. (2017). Value of DIF is calculated by dividing the dynamic and static strength. DIFs were obtained for both materials and both thicknesses. Even though the same trends of DIF are obtained by the model, experimental data provides greater DIFs in all cases. The rate independent version of the model was used for these simulations. It appears that for high loading rates, the material behavior

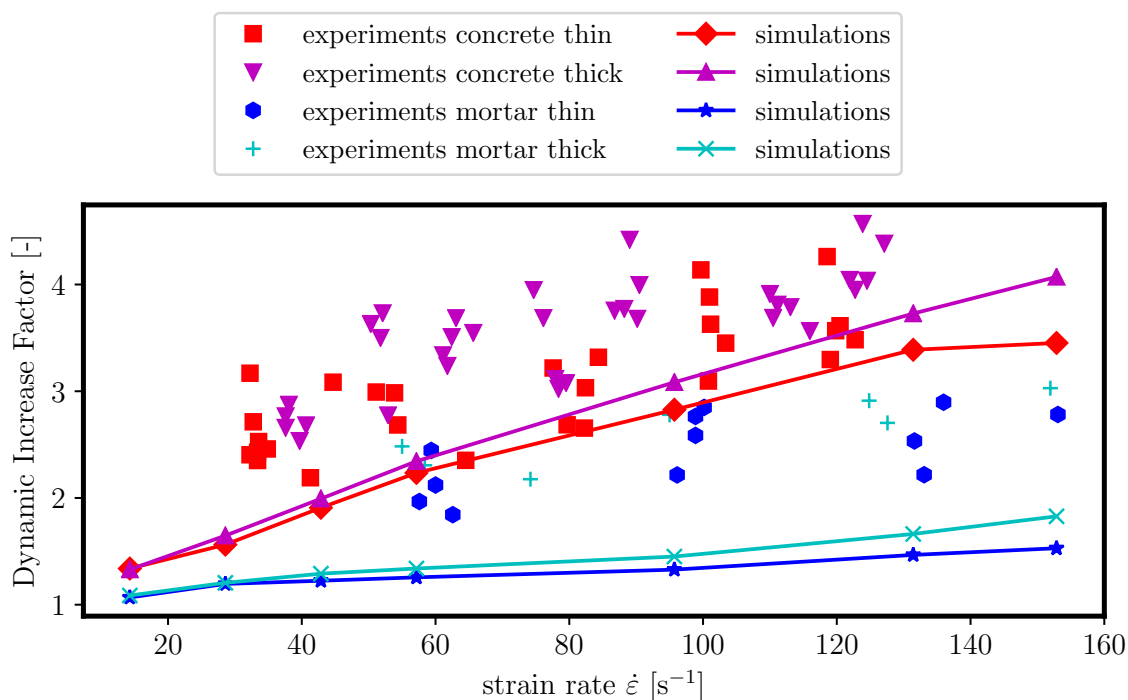


Fig. 9.15: Dynamic increase factor of material tensile strength obtained by the model compared with experimental measurements (Jin et al., 2017).

under the model resolution needs to be captured by rate dependent constitutive law.

9.5 Spalling test

Another simulated test also uses Hopkinson pressure bar setup. It is used for estimation of dynamical tensile strength induced by spalling. Test series reported by Erzar and Forquin (2011, 2010) was selected because of direct measurements of the rear face velocity, which is important for estimation of dynamic tensile strength. It was a large series of specimens tested using not only Hopkinson bar setup, but also tensile test performed in conventional apparatus to determine material properties under lower and quasi-static strain-rates.

The test setup consists of long metal (usually steel or aluminum alloy) bar and relatively short concrete cylinder at its end. Metal bar is loaded by impact of a projectile or by an explosive and the pressure wave propagates along the bar until it reaches its end. At the contact between metal and concrete, some part of pressure wave is reflected backwards to the metal bar as a tensile wave and the rest of it is transmitted into the concrete specimen, where it further propagates as a pressure wave. When it reaches the rear face of concrete cylinder, it is reflected as a tensile wave and, after reaching the material tensile strength, the specimen breaks.

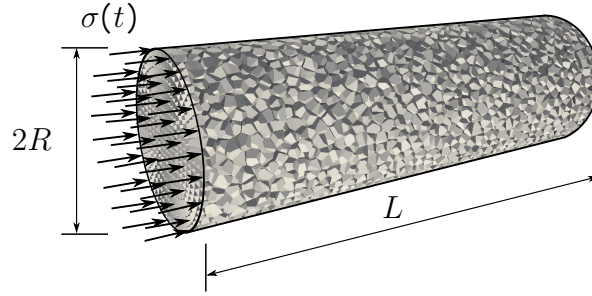


Fig. 9.16: Visualization of model geometry used in numerical simulation of spalling test – concrete cylinder discretized into particles loaded by a stress wave.

To determine the dynamic tensile strength from results of SHPB test, theory derived for 1D longitudinal wave propagation according to (Novikov et al., 1966) is usually applied. Erzar and Forquin (2010) use the following relation

$$f_{t,\text{dyn}} = \frac{1}{2} \rho c \Delta V_{\text{pb}} \quad (9.3)$$

where ΔV_{pb} is pullback velocity, which is a difference between the maximum and *residual* velocity of the rear face of the specimen, c is a wave speed, which can be for elastic materials analytically calculated

$$c = \sqrt{\frac{E(1-\nu)}{\rho(1+\nu)(1-2\nu)}} \quad (9.4)$$

Here E , ν and ρ are macroscopic elastic modulus, Poisson's ratio and density respectively. Empirical determination of residual velocity is proposed in Sec. 9.5.2.

Initially, the whole steel bar with the concrete specimen were simulated. Steel bar was represented by elastic finite elements and concrete by the discrete particles. Initial velocity was applied at the beginning of the steel bar corresponding to velocity of a projectile used for loading. However, this approach turned out to be too computationally demanding. Therefore, loading was applied by a stress wave applied at front face of the specimen as shown in Fig. 9.16.

Prior to the actual comparison of model results with the experimental data, several studies were conducted to understand the wave propagation and to correctly interpret the model results.

9.5.1 Wave propagation along elastic material

At first, propagation of a stress wave along elastic cylindrical bar was investigated, similarly to study done by Hwang et al. (2016). Stress wave was prescribed

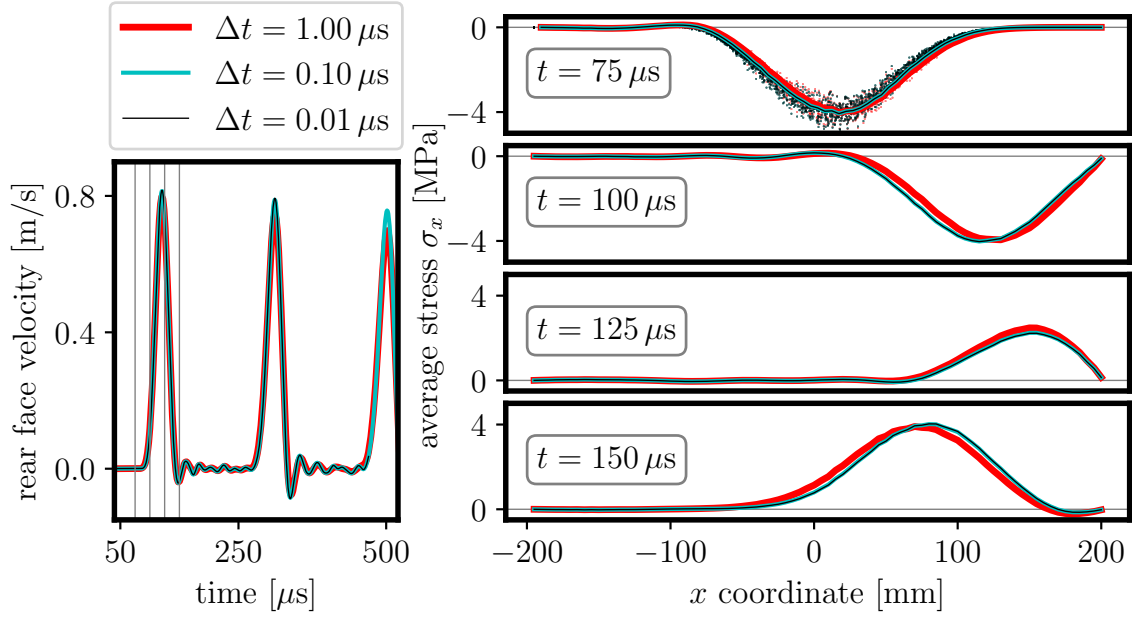


Fig. 9.17: Results for different time step length Δt , left: rear face velocity evolution in time, right: stress profile along the elastic bar in particular times.

according to one period of following cosine function

$$\sigma(t) = \begin{cases} \frac{1}{2} \left[\sigma_{\max} - \sigma_{\max} \cos\left(\frac{2\pi t}{t_P}\right) \right] & \text{for } t \leq t_P \\ 0 & \text{for } t > t_P \end{cases} \quad (9.5)$$

where σ_{\max} is the peak stress applied and t_P is the period of the stress wave. Chosen parameters are: length $L = 400$ mm and radius $R = 22.5$ mm, the maximum stress $\sigma_{\max} = 4$ MPa and the period of imposed stress wave $t_P = 50$ μ s. The material parameters are following: $E_0 = 70$ GPa, $\alpha = 0.237$, $\rho = 2340$ kg/m³ and $l_{\min} = 5$ mm.

In Fig.9.17, results of elastic simulations are plotted. The graph on the left shows evolution of the rear face velocity in time and the graphs in the right part show the stress profile along the bar in four different times during the simulation. The vertical lines in the left graph mark times when stress profiles are plotted.

Thanks to the heterogeneous inner material structure represented by the model, the stress profile is not smooth. This can be observed in the upper right graph in Fig.9.17 where nodal stress σ_x of each particle is represented by a small dot. In the lower graphs, only the average stress in longitudinal bar direction is plotted. Averaging is performed in slices of width 5 mm, corresponding to parameter l_{\min} dictating the particle size.

The color then refers to different time step length Δt used in the transient Newmark's solution. Even though the step length does not influence the stability

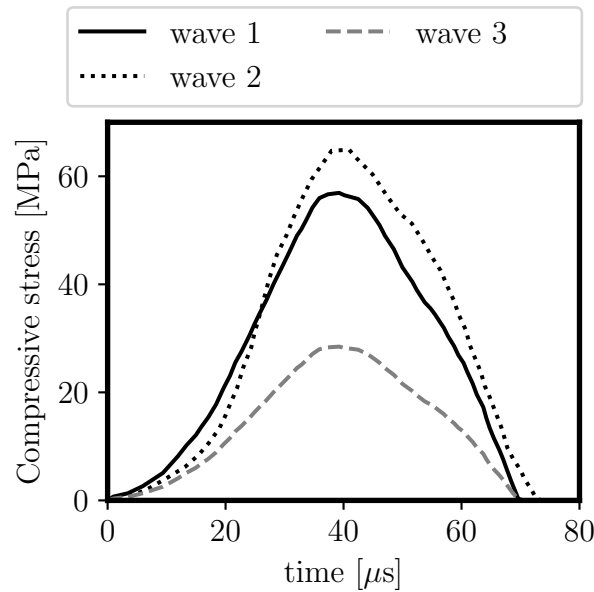


Fig. 9.18: Two stress waves reported by Erzar and Forquin (2011), wave 3 with half intensity of wave 1 is introduced for study of model behavior.

of the solution, it influences its accuracy, as can be observed from slightly different results for various step length. The wave tends to be faster when longer time-step is used. Also numerical damping has greater effect for longer Δt . Difference between solution with $\Delta t = 10^{-7}$ and $\Delta t = 10^{-8}$ is minimal, therefore time step chosen for further calculations is $\Delta t = 10^{-7}$ s.

Since the calculation of wave speed according to Eq. (9.4) takes into account macro-scopic properties that are known only approximately from the Eq. (3.8), the wave speed is calculated from the elastic model response. This actual wave speed obtained from the results of this test is $c_{act} \approx 4200\text{m/s}$.

9.5.2 Study of fracturing behavior

Prior to the comparison of the model with the experimental data, model behavior for this test setup was investigated also in nonlinear regime. Compressive stress wave imposed on the front face of the specimen is this time piecewise-linear function according to experimental data (Erzar and Forquin, 2011). The compressive wave has so high amplitude that tensile damage occurs in transverse direction. Such crushing cannot be seen in homogeneous models since it is a direct consequence of heterogeneity. This damage causes energy dissipation leading to reduction of wave intensity and also changes material behavior. Therefore it strongly affects obtained results. In order to reduce inelastic behavior under compressive wave propagation, smaller stress intensity than the experimental one was used. It is shown in Fig. 9.18

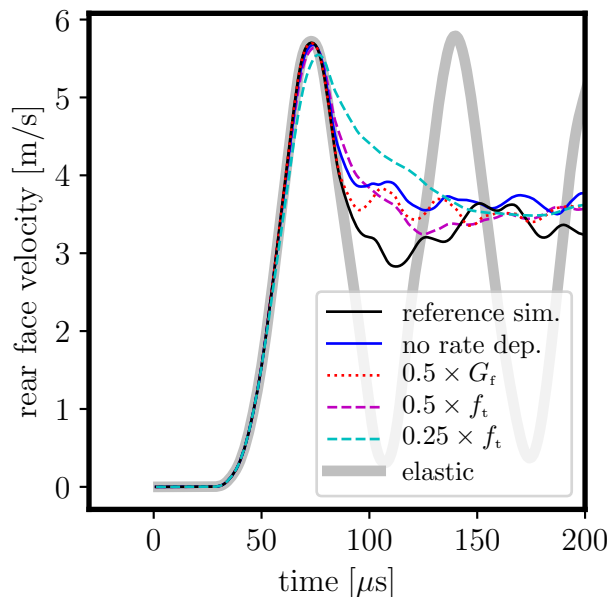


Fig. 9.19: Preliminary study on various material model settings.

as wave 3. Note that even for this reduced pressure wave, the strain-rate reaches value 20/s. Simulated specimen has length $L = 140$ mm and radius $R = 22.5$ mm. Elastic material parameters and density for this preliminary study are same as in Sec. 9.5.1, parameters governing nonlinear part of constitutive law are $f_t = 8$ MPa and $G_f = 36.5$ J/m². Parameters of rate dependency of are chosen according to recommendations in (Cusatis, 2011) $c_0 = 10^{-5}$ s⁻¹ and $c_1 = 5 \cdot 10^{-2}$.

The rear face velocity in time is plotted in Fig. 9.19 for 6 different material models. At first, elastic response was calculated. Then, the inelastic reference simulation was computed with material parameters mentioned above. Finally, four more material models were considered with (i) fracture energy decreased to one half, (ii) tensile strength decreased to one half and (iii) one quarter and (iv) eliminated strain rate dependency. For simulation with the lowest tensile strength, significant amount of damage occurs during propagation of pressure wave which leads to deviation of response from the elastic one already before peak velocity is reached.

The dynamic tensile strength is estimated using Eq. (9.3). Looking at the rear face velocity evolution, it is often unclear what value should be taken as pull-back velocity ΔV_{pb} .

For this purpose, response using three different material models was chosen for detailed comparison: The reference calculation and simulations using $0.5 G_f$ and $0.25 f_t$. These are shown in detail in Fig. 9.19. In the middle graph, derivative of velocity in time is plotted. The value of residual velocity v_r is here chosen as (i) the next local extreme after the peak velocity, $dv/dt = 0$ or (ii) the next inflex point after the peak, $d^2v/dt^2 = 0$. Time of occurrence of these events is highlighted in the

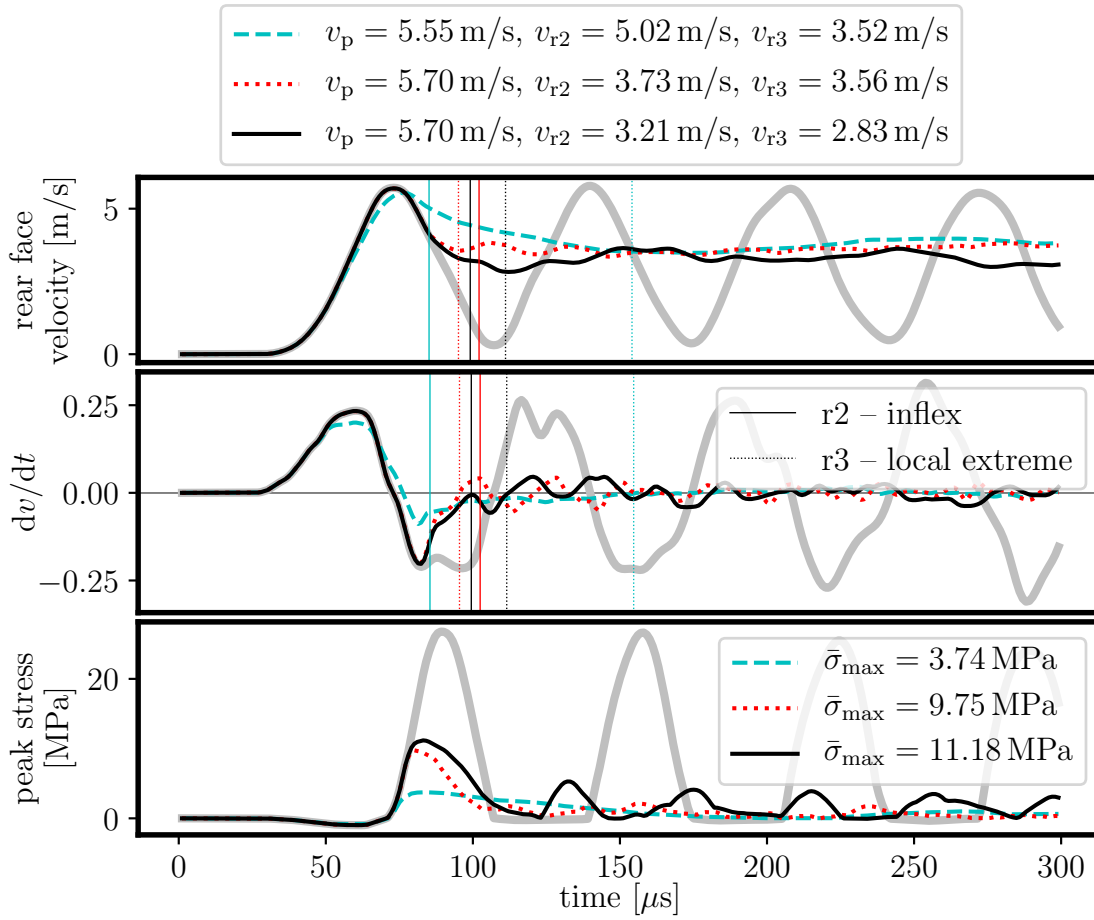


Fig. 9.20: Two different ways to estimate the residual velocity to calculate the pull-back velocity ΔV_{pb} .

calculation	v_p [m/s]	$v_{r2,3}$ [m/s]	Δ_{pb} [m/s]	$f_{t,dyn}$ [MPa]	$\bar{\sigma}_{max}$ [MPa]
0.25 f_t	5.55	5.02	0.53	2.58	3.74
		3.52	2.03	9.88	
0.5 G_f	5.70	3.73	1.97	9.50	9.75
		3.56	2.14	10.42	
reference	5.70	3.21	2.49	12.12	11.18
		2.86	2.84	13.82	

Tab. 9.3: Different $f_{t,dyn}$ according to different points considered for values of residual velocity v_r .

graphs as straight line of color corresponding to color of the response curve. Dotted lines are used for local extreme and solid lines for inflex points of the velocity in time. The bottom graph in Fig.9.19 shows evolution of the maximum tensile stress in longitudinal direction occurring in the model. In all three graphs, elastic response is plotted for comparison as thick grey curve. Values of dynamic tensile strength

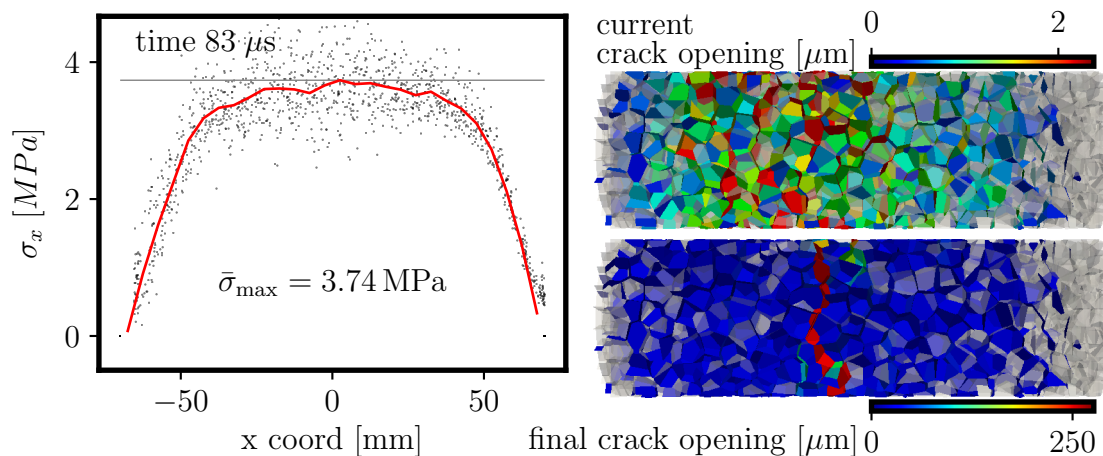


Fig. 9.21: Stress profile along the specimen and crack pattern in time of maximum tensile σ_x for simulation with $0.25 \times f_t$.

according to Eq. (9.3) are calculated in Tab. 9.3 for two mentioned values of v_r . In the table, maximum longitudinal stress $\bar{\sigma}_{\max}$ obtained by the numerical model is stated for comparison. The stress profiles of these three models responses are shown in Figs. 9.21-9.23 together with the crack pattern at the time of reaching the maximum tensile stress and at the end of the calculation. Average stress is represented by a red curve and stress in every node of meso-scale structure is represented by a small dot in stress profile.

At first, let us focus on the response of the model with $0.25 f_t$. This response deviates from the elastic even before the peak velocity, which is caused by the large damage during pressure wave propagation, see the crack in the right part of Fig. 9.21. A lot of contacts are damaged already at the time of the peak stress. The stress profile is shown in the same figure, value of the peak stress $\bar{\sigma}_{\max} = 3.74$ MPa. Calculation of the dynamic strength $f_{t,\text{dyn}}$ considering the local minimum gives exaggerated value. On the other hand, the value obtained with consideration of the inflex point is a bit lower than the model prediction, however it is much closer than the other one. The response of the material is highly influenced by the transverse damage due to huge compressive loading (relative to the material strength). This corresponds with the recommendation reported by Forquin et al. (2013) which states that one should avoid pressures larger than 30% of compressive strength for this spalling test.

Now compare the other two responses, the one with reference material model and the one using reduced fracture energy $0.5 G_f$. Even though the elastic limit is the same for both calculations, the resulting dynamic strength is different. The dynamic strength predicted by the numerical model is therefore dependent on both tensile strength and fracture energy. Also for these responses, the value of dynamic

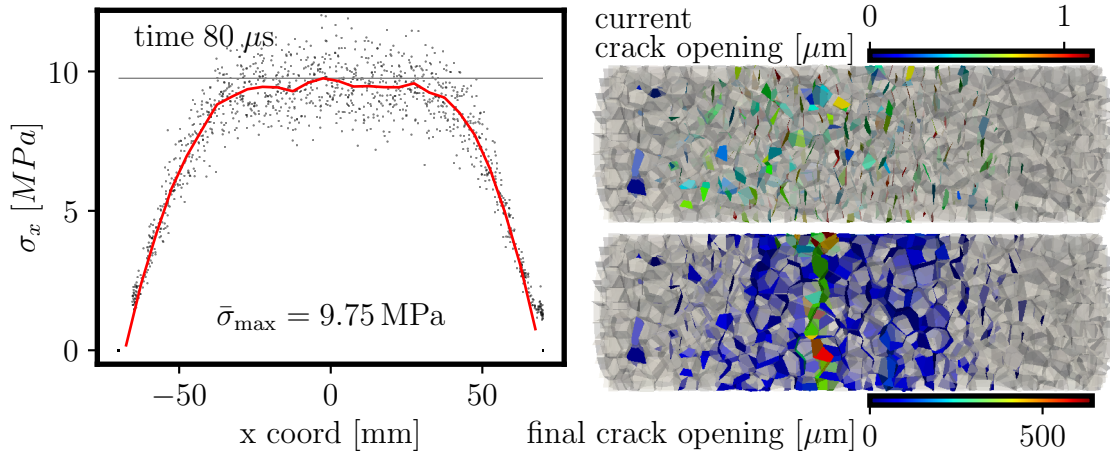


Fig. 9.22: Stress profile along the specimen and crack pattern in time of maximum tensile σ_x for simulation with $0.5 \times G_f$.

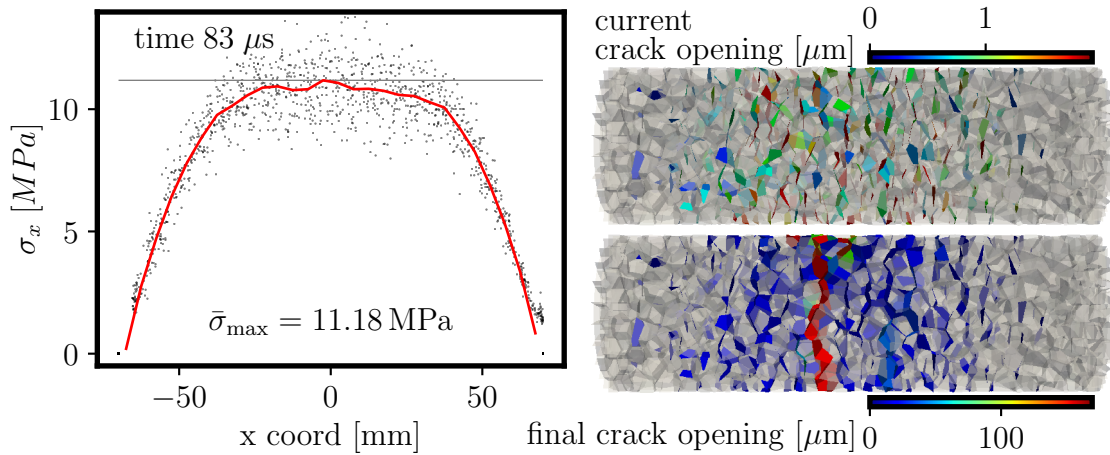


Fig. 9.23: Stress profile along the specimen and crack pattern in time of maximum tensile σ_x for reference simulation.

tensile strength calculated using the velocity at the inflex point is closer to the value of maximum stress $\bar{\sigma}_{\max}$ extracted from the meso-scale analysis.

9.5.3 Comparison to experimental data

Two tests were selected for comparison with results of the developed numerical model. These two tests differ only in stress waves transmitted from aluminum alloy bar of length 1.2 m. Both of the waves were measured by Erzar and Forquin (2011), they are plotted in Fig. 9.18 as waves 1 and 2. The maximum strain-rate calculated from the stress waves is 41/s and 94/s for wave 1 and 2, respectively.

Concrete specimens had length $L = 140$ mm and radius $R = 22.5$ mm, which are the same dimensions as in the previous section. Specimens were made of satu-

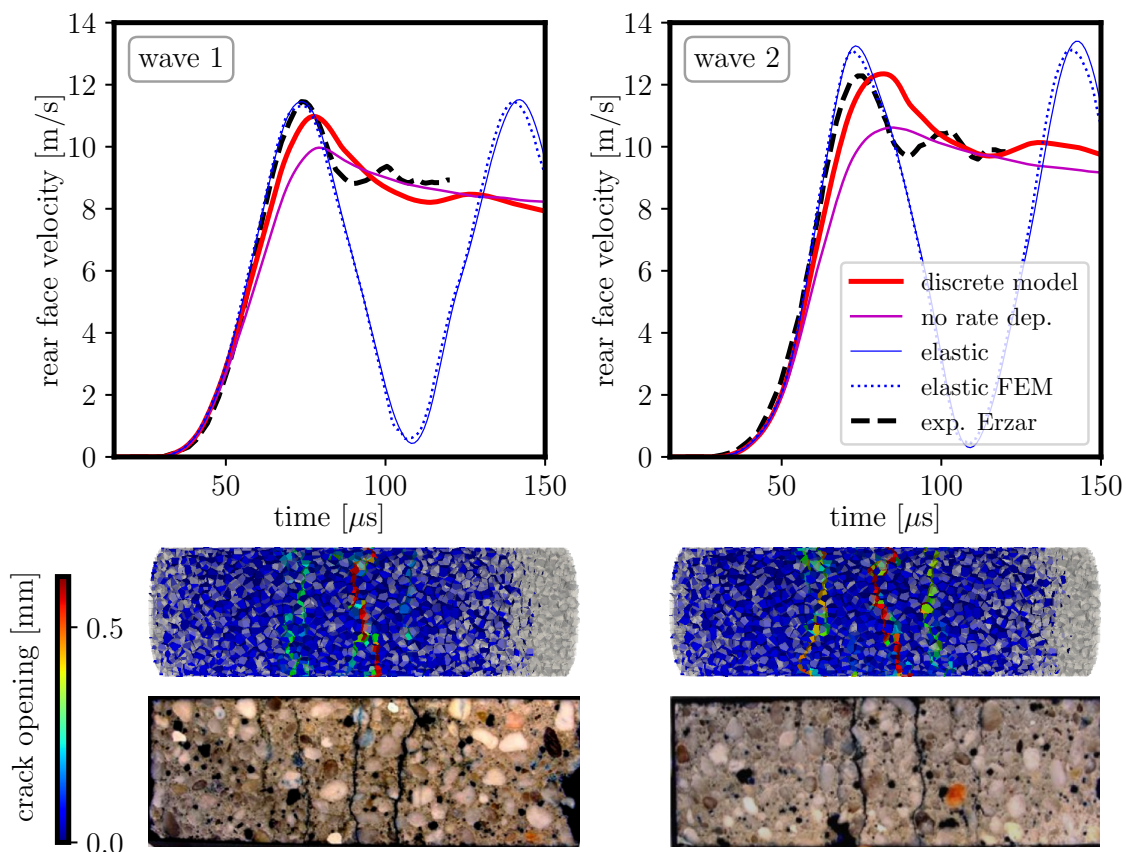


Fig. 9.24: Results of numerical simulations compared to the experimental data by Erzar and Forquin (2011).

rated (wet) concrete with the following macroscopic parameters: elastic modulus $E = 42$ GPa, Poisson's ratio $\nu = 0.2$, density $\rho = 2380$ kg/m³ and tensile strength $f_t = 3.7$ MPa.

The material parameters for the meso-scale model are following: elastic modulus $E_0 = 77$ GPa, parameter $\alpha = 0.1667$, density $\rho = 2380$ kg/m³, tensile strength $f_t = 3.7$ MPa and fracture energy $G_f = 36.5$ J/m². Parameters of rate dependency are $c_0 = 10^{-5}$ s⁻¹ and $c_1 = 10^{-1}$. Since the relation between macro and mesoscopic elastic properties – Eq. (3.8) – is only approximate, the actual mesoscale elastic modulus was identified from the wave speed and the maximum velocity of the rear face using *wave 1*. The resulting value $E_0 = 77$ GPa is slightly higher than 70 GPa which would be value obtained by Eq. (3.8). This is in agreement (Eliáš, 2017), because Eq. (3.8) underestimates E_0 for positive Poisson's ratios. For verification, results of elastic FEM simulation with the macroscopic elastic modulus and Poisson's ratio is performed. The difference between continuous and discrete elastic simulation is negligible for both waves (Fig. 9.24) and the difference is attributed to different solution methods. The continuous model used explicit time integration, while the

discrete model integrated in implicit scheme which suffers from numerical damping. The fracture energy G_f was chosen to obtain post peak evolution of the rear face velocity comparable to experimental data for the first loading case – wave 1. The second rate dependency parameter c_1 is increased for the same reason.

The model response for both loading cases along with experimental data (Erzar and Forquin, 2011) is shown in Fig. 9.24. It can be observed that the experimental peak velocity for wave 1 corresponds to the elastic response of the model. However, looking at the response for wave 2, the model elastic response of the same material is above the experimental peak velocity. It could possibly be explained by inelastic effects occurring in experiments during the pressure wave propagation, which did not occur under lower pressure of wave 1.

The responses of nonlinear model deviate from elastic response prior to reaching peak velocity in both cases, again due to inelastic effects during compression phase. These effects are magnified when rate dependency is neglected. The descending part of the simulated pullback velocity line is not as steep as reported in experiments. There are multiple macrocracks created in the model, shown in the bottom part of Fig. 9.24, which corresponds to the experimental evidence (Erzar and Forquin, 2011).

9.6 Conclusions about the dynamic model

Application of the discrete meso-scale model showed the model ability to imitate the dynamic concrete behavior. The model is, up to some point, able to reproduce both major attributes of the rate dependent concrete behavior, increase in loading forces and changes in the crack pattern. Initially, these were attributed to the heterogeneous material structure and its direct representation in the meso-scale model should have ensured capturing all the rate-dependency. This idea turned out to be too ambitious and rate-dependency of the constitutive law needed to be incorporated to enable more appropriate representation of material behavior, especially for high strain-rates.

The direct application of the displacement under higher strain rates resulted in crushing of the material close to the loading point. This occurred even though the displacement was applied via rigid plate and not in a single point. Various remedies were tried to fix this behavior, e.g. gradual increase in displacement rate instead of loading under full velocity from the beginning. These helped to prevent crushing, however, the increase in loading forces was lost due to reduced inertia effect.

The developed model was used to determine the macro-scopic homogeneous model characteristics in (Le et al., 2018). Dependency of the process zone size

and other characteristics on the strain rate and specimen size was investigated on a small specimens representing ceramics at fine resolution, using the presented model (Figs. 9.25 and 9.26). The specimens were loaded in tension, random field was considered.

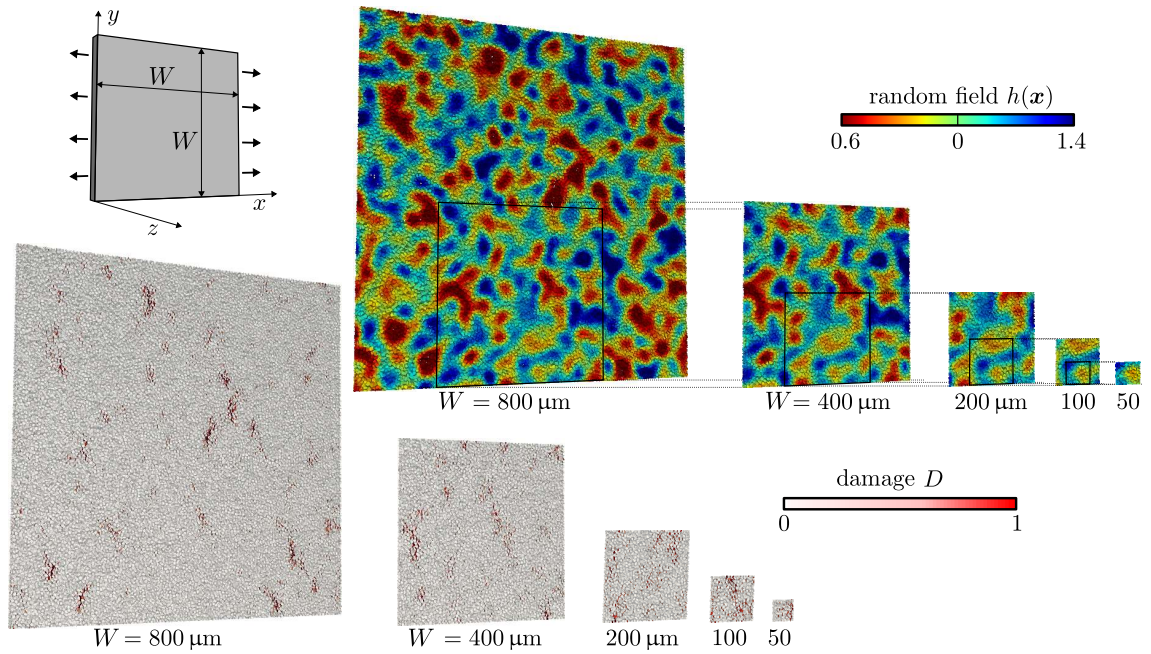


Fig. 9.25: Different fraction of damaged volume relative to different specimen size.

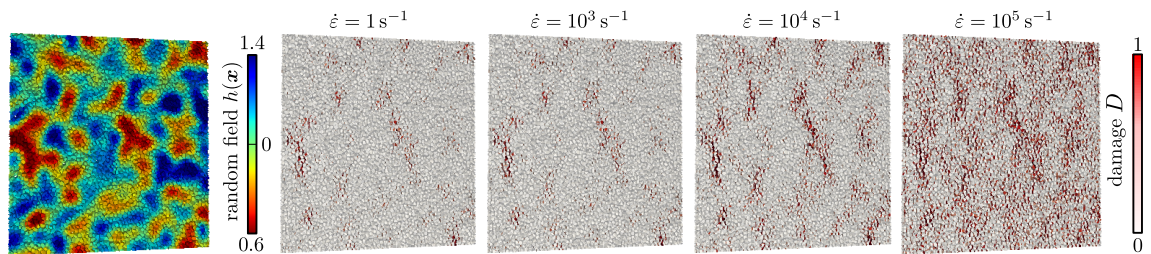


Fig. 9.26: Different amount of damaged volume for different strain rate for specimen of width = $400 \mu\text{m}$.

10 CLOSING REMARKS

The presented thesis is focused on the numerical analysis of concrete fracture using discrete meso-scale model. In the first part, the existing meso-scale model for static analysis is presented. The material representation and constitutive relations are described. Two following parts are devoted to two modifications of the computational model implemented by the author.

Part II presents incorporation of a short fiber reinforcement into the numerical model. Direct representation of fibers by additional elements was rejected in favour of indirect approach, taking into account frictional forces due to fiber resistance against pullout. The later was chosen to prevent the increase the number of degrees of freedom.

Concrete reinforced with tiny poly-vinyl-alcohol fibers is studied. At first, examples showing the model behavior on a single contact of two particles connected with one and multiple fibers are presented. The fiber constitutive law adopted from literature (Schauffert and Cusatis, 2012) has two main parts representing process of fiber debonding and pullout, respectively. The model behavior is then investigated on simulations of uni-axial tensile test of a prismatic beam made of fiber reinforced concrete. This study shows interaction between material parameters related to fibers and those related to the concrete matrix. If concrete is too strong, no strain-hardening behavior is predicted by the numerical model. This unfortunately cannot be confirmed by an experimental evidence, because the data on both plain and PVA-fiber reinforced concrete from one batch are missing.

Numerical simulations of experiments by Li et al. (2001) shows an ability of this model modification to predict complex behavior of the fiber reinforced composite, including strain-hardening and multiple cracking. However, fiber material parameters reported in the mentioned article and those used for fiber representation in computational model to obtain comparable response differ considerably.

Part III is devoted to extension of the discrete meso-scale model by an the implicit dynamic solver. An ability of the model to represent strain-rate dependent material behavior is investigated.

Initially, the constitutive law is considered strain-rate independent. The intention is to account for the rate dependent behavior by the direct representation of material inner structure. It appeared that processes at even lower scale influence the material response as well, especially for higher loading rates. Since these processes are under resolution of the model, they has to be incorporated into the constitutive law phenomenologically. The rate dependency of the constitutive law is adopted from Cusatis (2011).

Dynamic numerical model is initially used to simulate tests under relatively slow

loading rates, up to 4.3 m/s (Ožbolt et al., 2015, 2013). Numerical simulations of these experiments predict similar trends – increase of loading forces as well as the crack inclination for higher loading rates. It shows that the loading forces in dynamic regime are mostly influenced by the inertia. On the other hand, the model weakness is a local crushing in the area of applied load that occurred even though the loading was applied via rigid plate and with smooth increase of displacement rate.

Dynamic behavior under strain-rates higher than 10 s^{-1} is studied on Hopkinson bar setup. The experimental data on Brazilian splitting tests (Jin et al., 2017) and spalling experiments (Erzar and Forquin, 2010) are chosen for comparison. The large effect of inelastic material behavior during pressure wave propagation is described. It is shown that the estimation of the dynamical tensile strength can be highly influenced by the transverse tensile damage caused by the pressure wave. In case of spalling tests, the dynamical strength is estimated from the evolution of velocity at the rear face of the spalling specimen. It is discussed what value should be used as this residual pullback velocity. The most convenient seems to be the velocity at the first kink, the first local minimum might provide exaggerated dynamic strength, especially for the cases when the material is damaged already during pressure wave propagation. To avoid damaging the specimen by pressure wave, Forquin et al. (2013) recommend to use pressures lower than 30% of compressive strength in the dynamic spalling tests.

10.1 Future work

The discrete meso-scale model appears to be capable of representing the complex behavior of heterogeneous cement-based composite. This representation is, however, limited.

The limits of the current model configuration reveal the space for the future modifications. For example the transition from tensile into compressive loading that happens during reflection of the wave at the domain boundary, results into the loading unloading cycle. The constitutive law governed by the damage variable lacks representation of irreversible strain, model gives zero strain when fully unloaded. So the next step is modification of the constitutive law for more realistic representation of loading-unloading cycles.

Opportunity also lies in the application of the model to other materials or structures at different scales. For example, low-scale representation of masonry structures is a challenging task that the author considers to investigate further.

BIBLIOGRAPHY

- CEB-FIP MODEL CODE*, chapter 2. Material Properties, pages 33–81. 1990. doi:10.1680/ceb-fipmc1990.35430.0002.
- C. Adendorff, W. Boshoff, and G. van Zijl. Characterisation of crack distribution of strain-hardening cement composites (shcc) under imposed strain. *Advances in Cement-Based Materials*, pages 215–221, 2009. doi:10.1201/b10162-32.
- P.-C. Aïtcin. 4 - supplementary cementitious materials and blended cements. In P.-C. Aïtcin and R. J. Flatt, editors, *Science and Technology of Concrete Admixtures*, pages 53 – 73. Woodhead Publishing, 2016. ISBN 978-0-08-100693-1. doi:https://doi.org/10.1016/B978-0-08-100693-1.00004-7.
- C. B. Barber, D. P. Dobkin, D. P. Dobkin, and H. Huhdanpaa. The quickhull algorithm for convex hulls. *ACM Transactions on Mathematical Software (TOMS)*, 22(4):469–483, 1996.
- K.-J. Bathe. *Finite element procedures*. Prentice Hall, Englewood Cliffs, N.J., 1996. ISBN 01-330-1458-4.
- K.-J. Bathe and G. Noh. Insight into an implicit time integration scheme for structural dynamics. 98-99:1–6, 2012. ISSN 00457949. doi:10.1016/j.compstruc.2012.01.009.
- Z. P. Bažant and S.-D. Pang. Activation energy based extreme value statistics and size effect in brittle and quasibrittle fracture. *J Mech Phys Solids*, 55(1):91–131, 2007. ISSN 0022-5096. doi:http://dx.doi.org/10.1016/j.jmps.2006.05.007.
- Z. Bažant and B. Oh. Crack band theory for fracture of concrete. *Matériaux et Constructions*, 16(3):155–177, 1983. ISSN 0025-5432. doi:10.1007/BF02486267.
- Z. P. Bažant and F. Lin. Nonlocal smeared cracking model for concrete fracture. *Journal of Structural Engineering*, 114(11):2493–2510, 1988. ISSN 0733-9445. doi:10.1061/(ASCE)0733-9445(1988)114:11(2493).
- T. Belytschko and R. Gracie. On xfem applications to dislocations and interfaces. *International Journal of Plasticity*, vol. 23(10-11):1721–1738, 2007. ISSN 07496419. doi:10.1016/j.ijplas.2007.03.003.
- A. Bentur and S. Mindess. *Fibre reinforced cementitious composites*. New York, 2nd ed edition, 2007. ISBN 978-0-415-25048-1.

- M. Bignozzi and F. Sandrolini. Tyre rubber waste recycling in self-compacting concrete. *Cement and Concrete Research*, 36(4):735 – 739, 2006. ISSN 0008-8846. doi:<https://doi.org/10.1016/j.cemconres.2005.12.011>.
- J. E. Bolander, S. Choi, and S. R. Duddukuri. Fracture of fiber-reinforced cement composites. *International Journal of Fracture*, 154(1-2):73–86, 2008. ISSN 0376-9429. doi:10.1007/s10704-008-9269-4.
- A. Brara and J. Klepaczko. Experimental characterization of concrete in dynamic tension. *Mechanics of Materials*, 38(3):253 – 267, 2006a. ISSN 0167-6636. doi:10.1016/j.mechmat.2005.06.004.
- A. Brara and J. Klepaczko. Experimental characterization of concrete in dynamic tension. *Mechanics of Materials*, 38(3):253–267, 2006b. ISSN 01676636. doi:10.1016/j.mechmat.2005.06.004.
- R. Brepta, L. Půst, and F. Turek. *Mechanické kmitání*. Sobotáles, Praha, vyd. 1. edition, 1994. ISBN 80-901-6848-5.
- G. Cusatis. Strain-rate effects on concrete behavior. *International Journal of Impact Engineering*, 38(4):162–170, 2011. doi:10.1016/j.ijimpeng.2010.10.030.
- G. Cusatis and L. Cedolin. Two-scale study of concrete fracturing behavior. *Engineering Fracture Mechanics*, 74(1-2):3–17, 2007. doi:10.1016/j.engfracmech.2006.01.021.
- G. Cusatis, Z. P. Bažant, and L. Cedolin. Confinement-shear lattice model for concrete damage in tension and compression. *Journal of Engineering Mechanics*, vol. 129(12):1439–1448, 2003. ISSN 0733-9399. doi:10.1061/(ASCE)0733-9399(2003)129:12(1439).
- G. Cusatis, R. Rezakhani, M. Alnagar, X. Zhou, and D. Pelessone. Multiscale computational models for the simulation of concrete materials and structures. In *EURO-C 2014 Conference*, pages 23–38, 2014.
- J. Eibl and B. Schmidt-Hurtienne. Strain-rate-sensitive constitutive law for concrete. *Journal of Engineering Mechanics*, vol. 125(12):1411–1420, 1999. ISSN 0733-9399. doi:10.1061/(ASCE)0733-9399(1999)125:12(1411).
- J. Eliáš. Boundary layer effect on behavior of discrete models. *Materials*, 10(2):157, 2017. ISSN 1996-1944. doi:10.3390/ma10020157.

- J. Eliáš, M. Vořechovský, J. Skoček, and Z. P. Bažant. Stochastic discrete meso-scale simulations of concrete fracture. *Engineering Fracture Mechanics*, 135:1–16, 2015. ISSN 00137944. doi:10.1016/j.engfracmech.2015.01.004.
- B. Erzar and P. Forquin. An experimental method to determine the tensile strength of concrete at high rates of strain. *Experimental Mechanics*, 50(7):941–955, 2010. ISSN 0014-4851. doi:10.1007/s11340-009-9284-z. URL <http://link.springer.com/10.1007/s11340-009-9284-z>.
- B. Erzar and P. Forquin. Experiments and mesoscopic modelling of dynamic testing of concrete. *Mechanics of Materials*, 43(9):505–527, 2011. ISSN 01676636. doi:10.1016/j.mechmat.2011.05.002.
- A. P. Fantilli, H. Mihashi, and P. Vallini. Multiple cracking and strain hardening in fiber-reinforced concrete under uniaxial tension. *Cement and Concrete Research*, 39(12):1217–1229, 2009. ISSN 00088846. doi:10.1016/j.cemconres.2009.08.020.
- P. Forquin, W. Riedel, and J. Weerheijm. Chapter 6 - dynamic test devices for analyzing the tensile properties of concrete. In J. Weerheijm, editor, *Understanding the Tensile Properties of Concrete*, Woodhead Publishing Series in Civil and Structural Engineering, pages 137 – 181. Woodhead Publishing, 2013. ISBN 978-0-85709-045-4. doi:<https://doi.org/10.1533/9780857097538.2.137>.
- A. C. Fowler and B. Scheu. A theoretical explanation of grain size distributions in explosive rock fragmentation. *Proceedings of the Royal Society A: Mathematical, Physical and Engineering Science*, vol. 472(issue 2190):20150843–, 2016. ISSN 1364-5021. doi:10.1098/rspa.2015.0843.
- J. K. Gran, L. Seaman, and Y. M. Gupta. Application of a new technique to study the dynamic tensile failure of concrete. *Le Journal de Physique Colloques*, 46(C5): C5-617–C5-622, 1985. ISSN 0449-1947. doi:10.1051/jphyscol:1985579.
- P. Grassl, D. Grégoire, L. R. Solano, and G. Pijaudier-Cabot. Meso-scale modelling of the size effect on the fracture process zone of concrete. *International Journal of Solids and Structures*, vol. 49(13):1818–1827, 2012. ISSN 00207683. doi:10.1016/j.ijsolstr.2012.03.023. URL <http://linkinghub.elsevier.com/retrieve/pii/S0020768312001175>.
- Y. K. Hwang, J. E. Bolander, and Y. M. Lim. Simulation of concrete tensile failure under high loading rates using three-dimensional irregular lattice models. *Mechanics of Materials*, 101:136–146, 2016. ISSN 0167-6636. doi:10.1016/j.mechmat.2016.08.002.

- C. Jin, N. Buratti, M. Stacchini, M. Savoia, and G. Cusatis. Lattice discrete particle modeling of fiber reinforced concrete. *European Journal of Mechanics - A/Solids*, 57:85–107, 2016. ISSN 09977538. doi:10.1016/j.euromechsol.2015.12.002.
- X. Jin, C. Hou, X. Fan, C. Lu, H. Yang, X. Shu, and Z. Wang. Quasi-static and dynamic experimental studies on the tensile strength and failure pattern of concrete and mortar discs. *Scientific Reports*, 7(1), 2017. ISSN 2045-2322. doi:10.1038/s41598-017-15700-2.
- M. Jirásek. Nonlocal models for damage and fracture: comparison of approaches. *Solid Structures*, 35:4133–4145, 1998.
- M. Jirásek and Z. P. Bažant. Particle model for quasibrittle fracture and application to sea ice. *J. Eng. Mech.*, 121(9):1016–1025, 1995. doi:10.1061/(asce)0733-9399(1995)121:9(1016).
- J. Kang, K. Kim, Y. M. Lim, and J. E. Bolander. Modeling of fiber-reinforced cement composites: Discrete representation of fiber pullout. *International Journal of Solids and Structures*, 51(10):1970 – 1979, 2014. ISSN 0020-7683. doi:10.1016/j.ijsolstr.2014.02.006.
- T. Kawai. New discrete models and their application to seismic response analysis of structures. *Nuclear Engineering and Design*, 48(1):207 – 229, 1978. ISSN 0029-5493. doi:https://doi.org/10.1016/0029-5493(78)90217-0. Special Issue Structural Mechanics in Reactor Technology - Smirt-4.
- J.-L. Le and J. Eliáš. A probabilistic crack band model for quasibrittle fracture. *Journal of Applied Mechanics - ASME*, 83(5):051005–7, 2016. ISSN 0021-8936. doi:10.1115/1.4032692.
- J.-L. Le, J. Eliáš, A. Gorgogianni, J. Vievering, and J. Květoň. Rate-dependent scaling of dynamic tensile strength of quasibrittle structures. *Journal of Applied Mechanics*, 85(2), 2018. ISSN 0021-8936. doi:10.1115/1.4038496.
- J. Leppänen. Concrete subjected to projectile and fragment impacts. *International Journal of Impact Engineering*, vol. 32(11):1828–1841, 2006. ISSN 0734743x. doi:10.1016/j.ijimpeng.2005.06.005.
- C. Li and A. Der Kiureghian. Optimal discretization of random fields. *Journal of Engineering Mechanics - ASCE*, 119(6):1136–1154, 1993. ISSN 0733-9399. doi:http://dx.doi.org/10.1061/(ASCE)0733-9399(1993)119:6(1136).

- V. C. Li and S. Wang. Microstructure variability and macroscopic composite properties of high performance fiber reinforced cementitious composites. *Probabilistic Engineering Mechanics*, 21(3):201 – 206, 2006. ISSN 0266-8920. doi:<https://doi.org/10.1016/j.probengmech.2005.10.008>. Probability and Materials: from Nano- to Macro-Scale.
- V. C. Li, S. Wang, C. Wu, et al. Tensile strain-hardening behavior of polyvinyl alcohol engineered cementitious composite (pva-ecc). *ACI Materials Journal-American Concrete Institute*, 98(6):483–492, 2001.
- V. C. Li, C. Wu, S. Wang, A. Ogawa, and T. Saito. Interface tailoring for strain-hardening polyvinyl alcohol-engineered cementitious composite (pva-ecc). *Materials Journal*, 99(5):463–472, 2002.
- L. J. Malvar and J. E. Crawford. Dynamic increase factors for concrete. Technical report, Naval Facilities Engineering Service Center Port hueneme CA, 1998.
- F. Mellinger and D. Birkimer. Measurements of stress and strain on cylindrical test specimens of rock and concrete under impact loading. Technical report, Ohio River Div Labs Cincinnati, 1966.
- D. C. Montgomery. *Design and analysis of experiments*. John wiley & sons, 2017.
- A. E. Naaman, G. G. Namur, J. M. Alwan, and H. S. Najm. Fiber pullout and bond slip. i: Analytical study. *Journal of Structural Engineering*, 117(9):2769–2790, 1991. doi:10.1061/(ASCE)0733-9445(1991)117:9(2769).
- N. Newmark. *A method of computation for structural dynamics*. University of Illinois, Urbana, 1959.
- S. Novikov, I. Divnov, and A. Ivanov. Investigation of the fracture of steel, aluminum and copper during explosive loading. *Fiz Metallov Metalloved*, 21(4):608–615, 1966.
- J. Oliver. Modeling strong discontinuities in solid mechanics via strain softening constitutive equations. part 1: Fundamentals. part 2: Numerical simulations. *International Journal for Numerical Methods in Engineering*, vol. 39:3575–3623, 1996.
- J. Ožbolt, J. Bošnjak, and E. Sola. Dynamic fracture of concrete compact tension specimen. *International Journal of Solids and Structures*, vol. 50(25-26):4270–4278, 2013. ISSN 00207683. doi:10.1016/j.ijsolstr.2013.08.030.

- J. Ožbolt, N. Bede, A. Sharma, and U. Mayer. Dynamic fracture of concrete l-specimen. *Engineering Fracture Mechanics*, vol. 148:27–41, 2015. ISSN 00137944. doi:10.1016/j.engfracmech.2015.09.002.
- J. Ožbolt, A. Sharma, and N. Bede. Dynamic fracture of L and CT concrete specimens. *Proceedings of the 9th International Conference on Fracture Mechanics of Concrete and Concrete Structures*, 2016. doi:10.21012/FC9.098.
- C. Redon, V. C. Li, C. Wu, H. Hoshiro, T. Saito, and A. Ogawa. Measuring and modifying interface properties of pva fibers in ecc matrix. *Journal of Materials in Civil Engineering*, 13(6):399–406, 2001. ISSN 0899-1561. doi:10.1061/(ASCE)0899-1561(2001)13:6(399).
- E. A. Schauffert and G. Cusatis. Lattice discrete particle model for fiber-reinforced concrete. i. *Journal of Engineering Mechanics*, 138(7):826–833, 2012. ISSN 0733-9399. doi:10.1061/(ASCE)EM.1943-7889.0000387.
- C. Scheffler, S. Zhandarov, W. Jenschke, and E. Mäder. Poly (vinyl alcohol) fiber reinforced concrete: investigation of strain rate dependent interphase behavior with single fiber pullout test under quasi-static and high rate loading. *Journal of Adhesion Science and Technology*, 27(4):385–402, 2013.
- H. Schuler and H. Hansson. Fracture behavior of high performance concrete (hpc) investigated with a hopkinson-bar. <http://dx.doi.org/10.1051/jp4:2006134175>, 134, 08 2006. doi:10.1051/jp4:2006134175.
- S. Shah and A. Carpinteri. *Fracture Mechanics Test Methods For Concrete*, volume 5. CRC Press, 1991.
- F. Tonon. Explicit exact formulas for the 3-D tetrahedron inertia tensor in terms of its vertex coordinates. *Journal of Mathematics and Statistics*, 1(1):8–11, 2005. ISSN 15493644. doi:10.3844/jmssp.2005.8.11.
- J. G. M. van Mier. *Concrete fracture*. CRC Press, Boca Raton, FL, 2013.
- M. Vořechovský. Simulation of simply cross correlated random fields by series expansion methods. *Structural Safety*, 30(4):337–363, 2008. ISSN 01674730. doi:10.1016/j.strusafe.2007.05.002.
- J. Weerheijm and J. V. Doormaal. Tensile failure of concrete at high loading rates: New test data on strength and fracture energy from instrumented spalling tests. *International Journal of Impact Engineering*, 34(3):609 – 626, 2007. ISSN 0734-743X. doi:https://doi.org/10.1016/j.ijimpeng.2006.01.005.

- E. Worrell, L. Price, N. Martin, C. Hendriks, and L. O. Meida. Carbon dioxide emissions from the global cement industry. *Annual Review of Energy and the Environment*, 26(1):303–329, 2001. doi:10.1146/annurev.energy.26.1.303.
- H. Wu, Q. Zhang, F. Huang, and Q. Jin. Experimental and numerical investigation on the dynamic tensile strength of concrete. *International Journal of Impact Engineering*, 32(1):605 – 617, 2005. ISSN 0734-743X. doi:10.1016/j.ijimpeng.2005.05.008. Fifth International Symposium on Impact Engineering.
- D. Yan and G. Lin. Dynamic properties of concrete in direct tension. *Cement and Concrete Research*, 36(7):1371 – 1378, 2006. ISSN 0008-8846. doi:10.1016/j.cemconres.2006.03.003.
- E.-H. Yang, S. Wang, Y. Yang, and V. C. Li. Fiber-bridging constitutive law of engineered cementitious composites. *Journal of Advanced Concrete Technology*, 6(1):181–193, 2008a. ISSN 1346-8014. doi:10.3151/jact.6.181.
- E.-H. Yang, S. Wang, Y. Yang, and V. C. Li. Fiber-bridging constitutive law of engineered cementitious composites. *Journal of advanced concrete technology*, 6(1):181–193, 2008b.
- J. Zhou, S. Qian, M. G. S. Beltran, G. Ye, K. van Breugel, and V. C. Li. Development of engineered cementitious composites with limestone powder and blast furnace slag. *Materials and Structures*, 43(6):803–814, 2010. ISSN 1359-5997. doi:10.1617/s11527-009-9549-0.

Josef Květoň

January 5, 1989

kveton.j@fce.vutbr.cz • +420 541147131

Institute of Structural Mechanics • Faculty of Civil Engineering • Brno University of Technology

Veveří 331/95 • 602 00 Brno • Czech Republic

Current position

Brno University of Technology, Faculty of Civil Engineering

BRNO, CZECH REPUBLIC

Doctoral Student

Feb '15 – present

Discrete approach in damage mechanics

Teaching experience: *Fundamentals of Structural Mechanics, Structural Analysis II, (Czech)*

Education

Brno University of Technology, Faculty of Civil Engineering

BRNO, CZECH REPUBLIC

Master degree in Civil Engineering

2013 – 2015

Thesis "Simulation of Concrete Fracture Using Nonlocal Model"

Brno University of Technology, Faculty of Civil Engineering

BRNO, CZECH REPUBLIC

Bachelor degree in Civil Engineering

2009 – 2013

Thesis "Comparison of Localization Limiters for Strain - Softening"

International Activities

Delft University of Technology, Faculty of Civil Engineering and Geosciences

DELFT, NETHERLANDS

Erasmus+ Internship

Jan – July 2018

Simulations of Fiber Reinforced Composites

Courses attended

Gopas

BRNO, CZECH REPUBLIC

Object oriented programming in C++

Oct '16

International Center for Mechanical Sciences

UDINE, ITALY

Modeling, Simulation and Characterization of Multi-Scale Heterogeneous Materials

Sept '15

BOKU University

VIENNA, AUSTRIA

Multi-Scale and Multi-Phase Modeling of Aging Concrete Structures

June 15

BOKU University

VIENNA, AUSTRIA

Advanced Topics in Engineering Mechanics

June 15

Czech Technical University, Faculty of Civil Engineering

PRAGUE, CZECH REPUBLIC

Modeling of Localized Inelastic Deformation

Sept '14

Participation in research projects

GA19-12197S

2019 – present

Coupled discrete meso-scale model for mechanics and transport phenomena in concrete

GA19-06684J

2019 – present

Fatigue of structural concrete driven by cumulative measure of shear strain

FAST-J-18-5412

2018

Short fiber reinforcement in discrete meso-scale model

Principal investigator

FAST-J-17-4583

2017

Strain-rate effect in concrete fracture

Principal investigator

GJ15-19865Y

2016–2017

Discrete fracture models: adaptive remeshing, energy release rate, and stress along boundaries

Specialization, research interests: Computational Mechanics, Nonlinear Material Modeling, Fracture Mechanics, Localization Limiters, Discrete Models, Strain-rate Effect, Fiber Reinforcement

Computer skills: Structural design software Ansys/Scia/Rfem/Atena, CAD software, Office packages, \LaTeX , Programming languages Python/C++.

Languages: Czech (*native*), English (*upper intermediate*), German (*intermediate*).

Interests: Scouting, Futsal, Trekking, Mountain Climbing, Skiing, Cycling, Motorbikes, Archery

List of Publications

- KVĚTOŇ, J., ELIÁŠ, J. Influence of inertia and material properties on discrete simulation of dynamic fracture of concrete. *Procedia Structural Integrity*, 13:1367 – 1372, 2018a. ISSN 2452-3216. doi: <https://doi.org/10.1016/j.prostr.2018.12.286>. ECF22 - Loading and Environmental effects on Structural Integrity.
- LE, J.-L., ELIÁŠ, J., GORGOGIANNI, A., VIEVERING, J., KVĚTOŇ, J. Rate-dependent scaling of dynamic tensile strength of quasibrittle structures. *Journal of Applied Mechanics, Transactions ASME*, 85(2), 2018b. doi: 10.1115/1.4038496.
- KVĚTOŇ, J., ELIÁŠ, J. Simulations of dynamic concrete fracture with brazilian splitting test. In *Proceedings of the International Conference on Computational Methods*, 13, pages 1367 – 1372. Scien Tech Publisher, 2018c.
- KVĚTOŇ, J., ELIÁŠ, J. Simulations of concrete fracture at various strain rates: Parametric study. In *COMP-DYN 2017 - Proceedings of the 6th International Conference on Computational Methods in Structural Dynamics and Earthquake Engineering*, 2, pages 4847–4856, 2017d. doi: 10.7712/120117.5766.17557.
- KVĚTOŇ, J., ELIÁŠ, J. Discrete modeling of strain rate effect in concrete fracture. *Key Engineering Materials*, 754 KEM:345–348, 2017e. doi: 10.4028/www.scientific.net/KEM.754.345.
- KVĚTOŇ, J., ELIÁŠ, J. Vliv rychlosti zatěžování na porušení betonu: Numerická studie využívající diskrétní model. In *Sborník doktorandské konference k 95. výročí klokkerova ústavu*, 2016f. ISBN 978-80-248-3917-2.
- KVĚTOŇ, J., ELIÁŠ, J. Study of the nonlocal model parameters dependency. In *Proceedings of 18th International Conference of PhD students Juniorstav*, 2016g. ISBN 978-80-214-5311-1.
- KVĚTOŇ, J., ELIÁŠ, J. Identification of material parameters for nonlocal model of concrete fracture. In *Proceedings of the Fifteenth International Conference on Civil, Structural and Environmental Engineering Computing*. Civil-Comp Press, 2015h. doi: 10.4203/ccp.108.24.
- KVĚTOŇ, J., ELIÁŠ, J. Simulation of fracture experiments on concrete using nonlocal damage model. In *Proceedings of 13th International Conference Modeling in Mechanics*, 2015i. ISBN 978-80-248-3756-7.
- KVĚTOŇ, J., ELIÁŠ, J. Performance comparison of localization limiters. In *Proceedings of 20th International Conference Engineering Mechanics*, 2014j. ISBN 978-80-214-4871-1.